

PREPARATION OF MULTIFUNCTIONAL MATERIALS FOR  
PHOTOCATALYTIC APPLICATIONS

A THESIS SUBMITTED TO  
THE GRADUATE SCHOOL OF NATURAL AND APPLIED SCIENCES  
OF  
MIDDLE EAST TECHNICAL UNIVERSITY

BY

CEREN UZUN

IN PARTIAL FULFILLMENT OF THE REQUIREMENTS  
FOR  
THE DEGREE OF DOCTOR OF PHILOSOPHY  
IN  
CHEMISTRY

JUNE 2019



Approval of the thesis:

**PREPARATION OF MULTIFUNCTIONAL MATERIALS FOR  
PHOTOCATALYTIC APPLICATIONS**

submitted by **CEREN UZUN** in partial fulfillment of the requirements for the degree of **Doctor of Philosophy in Chemistry Department, Middle East Technical University** by,

Prof. Dr. Halil Kalıpçılar  
Dean, Graduate School of **Natural and Applied Sciences**

\_\_\_\_\_

Prof. Dr. Cihangir Tanyeli  
Head of Department, **Chemistry**

\_\_\_\_\_

Prof. Dr. Mürvet Volkan  
Supervisor, **Chemistry, METU**

\_\_\_\_\_

Assoc. Prof. Dr. Murat Kaya  
Co-Supervisor, **Chem. Eng. & Appl. Chemistry, Atılım Uni.**

\_\_\_\_\_

**Examining Committee Members:**

Prof. Dr. Ceyhan Kayran  
Chemistry, METU

\_\_\_\_\_

Prof. Dr. Mürvet Volkan  
Chemistry, METU

\_\_\_\_\_

Prof. Dr. Atilla Cihaner  
Chem. Eng. & Appl. Chemistry, Atılım Uni.

\_\_\_\_\_

Assoc. Prof. Dr. Y. Eren Kalay  
Metallurgical and Materials Eng., METU

\_\_\_\_\_

Assoc. Prof. Dr. Seha Tirkeş  
Chem. Eng. & Appl. Chemistry, Atılım Uni.

\_\_\_\_\_

Date: 27.06.2019

**I hereby declare that all information in this document has been obtained and presented in accordance with academic rules and ethical conduct. I also declare that, as required by these rules and conduct, I have fully cited and referenced all material and results that are not original to this work.**

Name, Surname: Ceren Uzun

Signature:

## ABSTRACT

### PREPARATION OF MULTIFUNCTIONAL MATERIALS FOR PHOTOCATALYTIC APPLICATIONS

Uzun, Ceren  
Doctor of Philosophy, Chemistry  
Supervisor: Prof. Dr. Mürvet Volkan  
Co-Supervisor: Assoc. Prof. Dr. Murat Kaya

June 2019, 144 pages

Due to the increasingly polluted environment and the limited energy reserves, the development of high efficient renewable technologies, green energy sources and eco-friendly methods for environmental remediation and energy production is highly important. Hydrogen (H<sub>2</sub>), as a clean and carbonless energy source, is of great potential in solving the environmental pollution and energy shortage. Turkey is a country that clued-in textile production. But the widespread discharge of wastewaters from the textile industries, which contain large amounts of dyes, has become a great concern to the environment and ecosystem due to their non-biodegradability, toxicity, and potential carcinogenicity. Therefore, finding effective treatment methods and extending the treatment units which use them is necessary. The need to meet stringent international regulations and standards for wastewater discharge has motivated the development of efficient, non-toxic and low-cost photocatalytic materials for the photodegradation of organic pollutants in wastewater.

Besides mild operating conditions photocatalytic process can be powered by sunlight which significantly reducing the energy required and therefore the operating costs. Thus, semiconductor photocatalyst has attracted widespread attention in the scientific

community due to its potential application in environmental remediation and hydrogen production. Owing to the strong oxidizing property, nontoxicity, and long-term photostability, nanostructured titanium dioxide (nano-TiO<sub>2</sub>) has many advantages when compared with other photocatalysts. However, there are still some shortcomings, such as the lack of a visible light response, a low quantum yield, and lower photocatalytic activity. To overcome these problems, studies have been focused on some strategies, including noble metal deposition, doping of metal or nonmetal ions, blending with another metal oxide, surface photosensitizing with dye, and compositing with a polymer. In particular, doping of metal and organic/inorganic composite materials, where the organic major component is based on polymers, are fast-growing areas of research.

Catalyst recovery and reuse are the two most important features for many catalytic processes. Most heterogeneous systems require a filtration or centrifugation step to recover the catalyst. However, magnetically supported catalysts can be recovered with an external magnet due to the paramagnetic character of the support thus remarkable catalyst recovery can be provided without the need for a filtration step and the catalysts can be subsequently reused in another cycle.

In this study, multifunctional organic-inorganic composite materials were prepared to provide environmental remediation with the removal of organic dyes found in wastewater from industry and produce H<sub>2</sub> from the water-ethanol mixture with photocatalytic process under ultraviolet and visible light respectively. For this purpose, novel, magnetically recyclable, poly (3, 4-ethylene dioxothiophene)(PEDOT) and noble metal nanoparticles modified TiO<sub>2</sub> nanoparticles based (CoFe<sub>2</sub>O<sub>4</sub>-PEDOT-TiO<sub>2</sub>/M, (M=Ag, Au, AgAu)) composite materials with high photocatalytic activity and well-separation property were produced. The enhanced photocatalytic properties of the composites driven by the

synergetic effects of TiO<sub>2</sub> nanoparticles with noble metal nanoparticles, and PEDOT were investigated. Besides, their separation from the liquid phase and reuse process were provided with the addition of magnetic silica coated cobalt ferrite (CoFe<sub>2</sub>O<sub>4</sub>@SiO<sub>2</sub>, MNP) nanoparticles into the composite structure.

The composition, morphology, and optical properties of the prepared composites were investigated with TEM, FE-SEM, ICP-OES, BET, particle size distribution (Zeta sizer), vibrating sample magnetometer (VSM) and UV-Vis measurements. The comparative photocatalytic activity of the prepared catalysts was investigated by using methylene blue (MB), a typical pollutant in the textile industry which has the relatively high toxicity and complex structures make them difficult to be treated by physical and biological methods, under UV and Visible light.

**Keywords:** Organic-inorganic Composites, Semiconductor Photocatalysts, Magnetic Separation, Hydrogen Production, Environmental Remediation

## ÖZ

### FOTOKATALİTİK UYGULAMALAR İÇİN ÇOK FONKSİYONLU MALZEMELERİN HAZIRLANMASI

Uzun, Ceren  
Doktora, Kimya  
Tez Danışmanı: Prof. Dr. Mürvet Volkan  
Ortak Tez Danışmanı: Doç. Dr. Murat Kaya

Haziran 2019, 144 sayfa

Gittikçe kirlenen çevre ve enerji rezervlerinin sınırlı olması nedeniyle, çevre ıslahı ve enerji üretimi için yüksek verimli yenilenebilir teknolojilerin, yeşil enerji kaynaklarının ve çevre dostu yöntemlerin geliştirilmesi önem kazanmaktadır. Örneğin karbon içermeyen, temiz enerji kaynağı olarak hidrojen (H<sub>2</sub>), çevre kirliliği ve enerji sorununun çözümünde büyük bir potansiyele sahiptir. Türkiye tekstil üretiminde söz sahibi bir ülkedir. Ancak tekstil endüstrilerinden çok miktarda boya içeren yaygın atıksu tahliyesi, biyobozunur olmamaları, zehirli olmaları ve potansiyel karsinojenisite sebebiyle çevre ve ekosistem için büyük bir endişe kaynağı haline gelmiştir. Bu nedenle etkili arıtma yöntemlerinin bulunması ve bu yöntemleri kullanan tesislerin yaygınlaştırılması gerekmektedir. Atık suyun tahliyesi ile ilgili katı uluslararası yönetmelik ve standartlar, güneş enerjisi kullanarak ışıl bozunma yöntemi ile atık sulardaki organik atıkların parçalanması için etkin, zehirli olmayan, düşük maliyetli etkin fotokatalitik malzemelerin geliştirilmesini öne çıkarmıştır.

Fotokatalitik arıtma kolay çalışma koşullarının yanı sıra, güneş ışığı ile çalıştığı için harcanan enerji ve buna bağlı olarak işletme masrafları da önemli ölçüde azalmaktadır. Buradan hareketle yarı iletken fotokatalizörler çevre ıslahı ve hidrojen gazı



üretimindeki olası uygulamaları sebebiyle bilim insanlarının yoğun olarak ilgisini çekmektedir. Nano yapıdaki titanyum dioksit (nano-TiO<sub>2</sub>), diğer fotokatalizörlerle kıyaslandığında, kolay oksitlenmesi, zehirli olmaması ve uzun süreli fotokararlılık göstermesi gibi pekçok avantaja sahiptir. Ancak, titanyum dioksitin de düşük kuantum verimi ve fotokatalitik etkinlik, görünür bölgedeki ışıkla etkileşememesi gibi sorunları vardır. Bu sorunların üstesinden gelebilmek için çalışmalar titanyum dioksitin, üzerine soy metal biriktirilmesi (deposition); metal ya da ametal iyon ile katkılanması, başka bir metal oksit ile harmanlanması, boya ile yüzeyinin ışığa duyarlı hale getirmesi ve polimer ile birleştirilmesi gibi bazı stratejiler üzerine odaklanmıştır. Özellikle metal katkı ve polimer bazlı organik-inorganik titanyum dioksit kompozit malzemeler, hızlı büyüyen araştırma alanlarıdır.

Üzerinde önemle durulan bir diğer konu da katalizörün geri kazanılması ve yeniden kullanılabilmesidir. Pek çok heterojen sistem katalizörün geri kazanımı için bir süzme ya da santrifüj basamağını gerektirir. Ancak manyetik olarak desteklenmiş katalizörler, desteğin manyetik karakterine bağlı olarak harici bir mıknatıs yardımı ile geri kazanılabilir. Böylece bahsedilen ayırma adımlarına ihtiyaç duyulmadan dikkate değer bir katalizör geri kazanımı sağlanır ve katalizör sonradan başka bir döngüde tekrar kullanılabilir.

Bu çalışmada, ultraviyole (UV) ve görünür bölge (Vis) ışık kaynağı kullanarak fotokatalitik bozunma yolu ile, atık sularda bulunan organik boyaların giderimi ile çevre ıslahı sağlamak ve hidrojen gazı (H<sub>2</sub>) üretmek için çok işlevli organik-inorganik kompozit fotokatalizörlerin geliştirilmesi planlanmıştır. Bu amaçla, yüksek fotokatalitik aktiviteye sahip, yeni, manyetik olarak geri kazanılabilir, poli(3,4-etilendioksitiyofen) (PEDOT) ve soy metal (Ag, Au) nanoparçacıklarla katkılanmış titanyum bazlı (TiO<sub>2</sub>) kompozit malzemeler (CoFe<sub>2</sub>O<sub>4</sub>@SiO<sub>2</sub>-PEDOT-TiO<sub>2</sub>/M, (M=Ag, Au, AgAu,)) üretilmiştir. Kompozit malzemelerin fotokatalitik özelliklerinin, TiO<sub>2</sub> nanopartikülleri, soy metal nanoparçacıkları ve PEDOT yüklemesi ile birlikteli olarak etkileşiminin katalitik aktiviteye etkisi incelenmiştir. Bunun yanında manyetik

silika kaplı kobalt ferrit ( $\text{CoFe}_2\text{O}_4@\text{SiO}_2$ , MNP) nanoparçacıkların kompozit yapıya eklenmesiyle, sıvı fazdan ayrılması ve yeniden kullanılması işleminin harici bir miknatis kullanılarak yapılabilmesi sağlanmıştır.

Hazırlanan kompozitlerin kompozisyonu, yapısı, biçimbilgisi ve optik özellikleri TEM, FE-SEM, ICP-OES, BET, parçacık boyutu dağılımı (Zeta sizer), titreşen örnek magnetometresi (VSM) ve UV-Vis kullanılarak incelenmiştir. Hazırlanan katalizörlerin karşılaştırmalı fotokatalitik etkinliği, farklı ışık kaynakları (UV,Vis,) altında araştırılmıştır. Üretilen katalizörlerin fotokatalitik olarak organik boya parçalamadaki etkinliğini tespit etmek için, tekstil endüstrisinde yüksek zehirliliğe ve fiziksel ve biyolojik yöntemlerle işleme sokulmasına engel karmaşık yapılara sahip olan metilen mavisi (MB) kullanılmıştır.

Anahtar Kelimeler: Organik-inorganik Kompozitler, Yarı-iletken Fotokatalizörler, Manyetik Ayırma, Hidrojen Üretimi, Çevre Islahı

To My Family

## ACKNOWLEDGEMENTS

Foremost, I would like to express my sincere gratitude to my advisor Prof. Dr. Mürvet Volkan for her continuous support, her patience, encouragement, motivation and advices throughout my time as her student.

I also wish to express my deepful thanks to Assoc. Prof. Dr. Murat Kaya for encouraging my research and for allowing me to enhance myself as a research scientist. His advices and valuable suggestions helped me on both research studies as well as on my career.

I would like to thank my thesis monitoring committee members, Prof. Dr. Ceyhan Kayran, Assoc. Prof. Dr. Y. Eren Kalay for their priceless suggestions, advices, useful discussions and comments.

Thanks also extended to Prof. Dr. Atilla Cihaner, Assoc. Prof. Dr. Seha Tirkeş and Dr. Salih Ertan for their valuable suggestions and endless help throughout my experimental studies in ATOMSEL.

I would like to express my gratefulness to Assoc. Prof. Dr. Erk İnger for his patience, support and trust in every situation.

Endless thanks to my family, Bergüzar Uzun, Feridun Uzun and Şebnem Uzun for their love, trust and patience. Their support is the most profitable experience of my life.

This work was supported by Scientific and Technological Research Council of Turkey (TUBITAK) (Project No: 115Z550).

The last but not least, I would like to express my thanks to my lovely friends, Eda aęlı, İzay Reyhanoęlu, Simge Örsçelik, Hande Işın, Nursevinç Karakuş, Asena Şanlı, Güray Hatipoęlu and my previous research assistant Dr. Tuęba Nur Alp for their endless support, encouragement and patience.

## TABLE OF CONTENTS

ABSTRACT .....	v
ÖZ.....	viii
ACKNOWLEDGEMENTS.....	xii
TABLE OF CONTENTS .....	xiv
LIST OF TABLES.....	xviii
LIST OF FIGURES .....	xix
LIST OF ABBREVIATIONS.....	xxiv
CHAPTERS	
1. INTRODUCTION.....	1
1.1. Energy .....	2
1.1.1. Hydrogen Energy .....	4
1.2. Environmental Remediation .....	7
1.3. Advanced Oxidation Processes (AOPs).....	9
1.4. Semiconductors for Photocatalysis .....	16
1.4.1. TiO <sub>2</sub> as a Photocatalyst .....	19
1.5. Doping of Semiconductors.....	24
1.5.1. Nobel Metal Doping .....	24
1.5.1.1. Silver Nanoparticles Doped TiO <sub>2</sub> .....	28
1.5.1.2. Gold Nanoparticles Doped TiO <sub>2</sub> .....	30
1.5.1.3. Bimetallic Nanoparticles Doping .....	32
1.5.2. Conducting Polymers .....	34
1.5.2.1. PEDOT .....	36

1.6. Magnetic Separation.....	38
1.7. Scope of the Thesis.....	41
2. EXPERIMENTAL.....	43
2.1. Chemicals and Reagents.....	43
2.1.1. Preparation of Cobalt Ferrite and Silica Coating on Cobalt Ferrite Magnetic Nanoparticles .....	43
2.1.2. Preparation of Conducting Poly (3,4-ethylenedioxythiophene) (PEDOT), Magnetically Recyclable MNP-PEDOT and MNP-PEDOT-TiO <sub>2</sub> .....	43
2.1.3. Addition of Metal Nanoparticles onto the Surface of Materials.....	44
2.2. Instrumentation.....	44
2.2.1. Field Emission Scanning Electron Microscope (FE-SEM) .....	44
2.2.2. Transmission Electron Microscopy (TEM) .....	44
2.2.3. Energy Dispersive X-ray Spectrometer (EDX) .....	45
2.2.4. Vibrating Sample Magnetometer (VSM) .....	45
2.2.5. Inductively Coupled Plasma Optical Emission Spectrometer (ICP-OES).....	45
2.2.6. Atlas Solar Simulator.....	45
2.2.7. Surface Area Analysis by using Brunauer–Emmett–Teller (BET) .....	46
2.2.8. Gas Chromatography (GC) Measurements.....	46
2.2.9. UV-Vis Spectrophotometer .....	46
2.3. Preparation of Cobalt Ferrite (CoFe <sub>2</sub> O <sub>4</sub> ) Magnetic Nanoparticles with Surface Modification .....	46
2.3.1. Preparation of Cobalt Ferrite (CoFe <sub>2</sub> O <sub>4</sub> ) Magnetic Nanoparticles .....	46
2.3.2. Silica Coating onto Cobalt Ferrite Magnetic Nanoparticles .....	47
2.4. Preparation of PEDOT, Magnetically Recyclable MNP-PEDOT and MNP-PEDOT-TiO <sub>2</sub> .....	48

2.4.1. Preparation of Conducting Polymer, PEDOT .....	48
2.4.2. Preparation of Magnetically Recyclable, MNP-PEDOT Composite Material .....	50
2.4.3. Preparation of Magnetically Recyclable, MNP-PEDOT-TiO <sub>2</sub> Composite Material .....	51
2.5. Addition of Noble Metal Nanoparticles onto the Surface of Composite Materials.....	52
2.6. Degradation of Methylene Blue Under Light Source .....	53
2.7. Hydrogen Generation Experiments Under UV Light Irradiation .....	55
3. RESULTS AND DISCUSSION .....	57
3.1. Preparation and Characterization of Composite Materials .....	58
3.1.1. Preparation and Characterization of Silica-Coated Magnetic Nanoparticles .....	58
3.1.2. Preparation and Characterization of PEDOT Polymer and MNP-PEDOT Composite Material .....	62
3.1.3. Preparation and Characterization of MNP-PEDOT-TiO <sub>2</sub> Composite Material .....	66
3.1.4. Characterization of Silver and Gold Nanoparticle Added TiO <sub>2</sub> Nanoparticles.....	70
3.1.5. Characterizations of Silver-Gold Bimetallic Nanoparticle Added TiO <sub>2</sub> Nanoparticles.....	73
3.1.6. Characterizations of Silver Nanoparticle Added MNP-PEDOT-TiO <sub>2</sub> Composite Material .....	75
3.1.7. Characterizations of Gold Added MNP-PEDOT-TiO <sub>2</sub> Composite Material .....	77



3.1.8. Characterizations of Silver-Gold Bimetallic Nanoparticle Added MNP-PEDOT-TiO <sub>2</sub> Composite Material.....	79
3.2. Photocatalytic Activity Results of Prepared Composite Materials .....	80
3.2.1. Adsorption Profiles of the Prepared Nanostructures .....	80
3.2.2. Photocatalytic Activity of the Prepared Structures Under UV Light Illumination.....	84
3.2.3. Photocatalytic Activity of the Prepared Structures Under Solar Light Illumination.....	94
3.2.4. Reuse Studies.....	103
3.3. Measurements of the Degradation Products of Methylene Blue by Using LC-MS .....	106
3.4. Photocatalytic Hydrogen Production Studies .....	110
4. CONCLUSION.....	125
REFERENCES.....	127
CURRICULUM VITAE .....	143

## LIST OF TABLES

### TABLES

Table 3.1. Percent adsorption values of TiO <sub>2</sub> nanoparticle under dark condition for different durations.....	82
Table 3.2. Percent adsorption values of MNP-PEDOT-TiO <sub>2</sub> composite material under dark condition for different durations.....	83
Table 3.3. Percent dye degradation efficiency of TiO <sub>2</sub> nanoparticles under UV light for different durations. ....	85
Table 3.4. Calculated percent dye degradation results of all catalysts prepared in this study under UV light for different durations. ....	86
Table 3.5. The comparison of the initial rates of the MNP-PEDOT-TiO <sub>2</sub> with TiO <sub>2</sub> , PEDOT and MNP-PEDOT catalyst.....	90
Table 3.6. The comparison of the percent degradation of MB under UV light by using 2 mg TiO <sub>2</sub> nanoparticles and MNP-PEDOT-TiO <sub>2</sub> which contains 2 mg TiO <sub>2</sub> nanoparticles. ....	91
Table 3.7. Calculated percent dye degradation results of all catalysts prepared in this study from UV-Vis spectra obtained under solar light for different durations.....	95
Table 3.8. The comparison of the results with literature .....	102
Table 3.9. Comparison of the hydrogen amounts obtained by using photocatalyst produced during the study. ....	122

## LIST OF FIGURES

### FIGURES

Figure 1.1. Schematic diagram of the mechanism of photocatalyst [58].....	17
Figure 1.2. Schematic illustration of charge separation mechanism under UV light irradiation [85]. .....	25
Figure 1.3. Schottky barrier between a metal and a semiconductor. $E_g$ is the band gap of semiconductor and $\Phi_B$ is the height of Schottky barrier [86].....	26
Figure 1.4. Schematic illustration of (a) surface plasmon resonance (b) charge separation mechanism under visible light irradiation [85].....	27
Figure 1.5. Schematic illustration of bimetallic nanoparticles [108].....	32
Figure 1.6. Chemical structures of some conducting polymers (CPs).....	35
Figure 2.1. Illustration for the preparation of magnetic nanoparticles.....	47
Figure 2.2. Illustration for the preparation of silica-coated magnetic nanoparticles. ....	48
Figure 2.3. Schematic representation of chemical polymerization of EDOT by using $FeCl_3$ initiator.....	49
Figure 2.4. Illustration for the preparation of PEDOT polymer. ....	50
Figure 2.5. Illustration for the preparation of MNP-PEDOT composite material. ....	51
Figure 2.6. Illustration for the preparation of MNP-PEDOT- $TiO_2$ composite material. ....	52
Figure 2.7. Illustration for the loading procedure of Ag and Au ions onto the surface and chemical reduction of the ions via $NaBH_4$ .....	53
Figure 2.8. Photocatalytic reactor and UV system that were utilized throughout the photocatalytic efficiency tests. ....	54
Figure 2.9. Atlas solar simulator system that was utilized throughout the photocatalytic efficiency tests. ....	55

Figure 2.10. (a) System that was used to generate hydrogen gas from the ethanol-water mixture under UV light (b) Tedlar bag for collecting a gas sample for GC analyses. .... 56

Figure 3.1. SEM image of  $\text{CoFe}_2\text{O}_4$  magnetic nanoparticles. .... 58

Figure 3.2. EDX pattern of  $\text{CoFe}_2\text{O}_4$  magnetic nanoparticles. .... 59

Figure 3.3. TEM image of  $\text{CoFe}_2\text{O}_4@SiO_2$  core-shell magnetic nanoparticles. .... 60

Figure 3.4. EDX pattern of  $\text{CoFe}_2\text{O}_4@SiO_2$  core-shell magnetic nanoparticles. .... 60

Figure 3.5. Magnetization vs. magnetic field for  $\text{CoFe}_2\text{O}_4@SiO_2$  core-shell magnetic nanoparticles. .... 61

Figure 3.6. SEM image of PEDOT..... 63

Figure 3.7. SEM image of MNP-PEDOT..... 64

Figure 3.8. Comparison of SEM images of PEDOT polymer and MNP-PEDOT. .... 65

Figure 3.9. TEM image of  $TiO_2$  nanoparticles. .... 66

Figure 3.10. TEM image of MNP-PEDOT-  $TiO_2$ . .... 67

Figure 3.11. EDX pattern of MNP-PEDOT- $TiO_2$ . .... 68

Figure 3.12. Magnetization vs. magnetic field for MNP-PEDOT- $TiO_2$ ..... 69

Figure 3.13. Magnetic behavior of MNP-PEDOT- $TiO_2$  composite material under externally applied magnetic field (1.6 T). .... 70

Figure 3.14. TEM image of Ag added  $TiO_2$  nanoparticles..... 71

Figure 3.15. EDX Analysis of Ag added  $TiO_2$ . .... 71

Figure 3.16. TEM image of Au added  $TiO_2$  nanoparticles..... 72

Figure 3.17. EDX pattern of Au added  $TiO_2$  nanoparticles..... 73

Figure 3.18. TEM image of AgAu NPs added  $TiO_2$  nanoparticles. .... 74

Figure 3.19. EDX pattern of AgAu bimetallic nanoparticles added  $TiO_2$  nanoparticles. .... 75

Figure 3.20. TEM image of MNP-PEDOT- $TiO_2$ -AgNPs composite material..... 76

Figure 3.21. EDX pattern of Ag nanoparticle added MNP-PEDOT- $TiO_2$  composite material. .... 77

Figure 3.22. TEM image of MNP-PEDOT- $TiO_2$ -AuNPs composite material..... 78

Figure 3.23. EDX pattern of Au nanoparticle added MNP-PEDOT-TiO <sub>2</sub> composite material.....	78
Figure 3.24. TEM image of MNP-PEDOT-TiO <sub>2</sub> -AgAuNPs. ....	79
Figure 3.25. EDX pattern of AgAu nanoparticle added MNP-PEDOT-TiO <sub>2</sub> composite material.....	80
Figure 3.26. UV-Vis spectra of the MB solution taken initially and after mixed with 10 mg of TiO <sub>2</sub> nanoparticles under dark environment for different durations. ....	81
Figure 3.27. UV-Vis spectra of the MB solution taken initially and after mixed with 10 mg of MNP-PEDOT-TiO <sub>2</sub> composite material under dark environment for different durations. ....	83
Figure 3.28. UV-Vis spectra of the MB solution shows the photocatalytic degradation of MB under UV light in the presence of 10 mg TiO <sub>2</sub> nanoparticles (Degussa P25) for different durations. ....	85
Figure 3.29. Comparison of the percent degradation of MB under UV light by using a) TiO <sub>2</sub> , b) TiO <sub>2</sub> -AgNPs, c) TiO <sub>2</sub> -AuNPs and d) TiO <sub>2</sub> -AgAuNPs catalysts.....	87
Figure 3.30. Comparison of the percent degradation of MB under UV light by using a) TiO <sub>2</sub> , b) PEDOT, c) MNP-PEDOT and d) MNP-PEDOT-TiO <sub>2</sub> .....	89
Figure 3.31. Comparison of the percent degradation of MB under UV light by using a) MNP-PEDOT-TiO <sub>2</sub> , b) MNP-PEDOT-TiO <sub>2</sub> -AgNPs, c) MNP-PEDOT-TiO <sub>2</sub> -AuNPs and d) MNP-PEDOT-TiO <sub>2</sub> /AgAuNPs.....	93
Figure 3.32. UV-Vis spectra of the MB solution shows the photocatalytic degradation of MB under solar light illumination in the presence of 10 mg TiO <sub>2</sub> nanoparticles (Degussa P25) for different durations. ....	94
Figure 3.33. Comparison of the percent degradation of MB under solar light by using a) TiO <sub>2</sub> , b) TiO <sub>2</sub> -AgNPs, c) TiO <sub>2</sub> -AuNPs and d) TiO <sub>2</sub> AgAuNPs.....	96
Figure 3.34. Comparison of the percent degradation of MB under solar light by using a) TiO <sub>2</sub> , b) PEDOT, c) MNP-PEDOT and d) MNP-PEDOT-TiO <sub>2</sub> catalyst.....	97
Figure 3.35. Comparison of the percent degradation of MB under solar light by using a) MNP-PEDOT-TiO <sub>2</sub> , b) MNP-PEDOT-TiO <sub>2</sub> -Ag, c) MNP-PEDOT-TiO <sub>2</sub> -Au and d) MNP-PEDOT-TiO <sub>2</sub> -AgAu catalyst. ....	99

Figure 3.36. Proposed mechanism of photodegradation of MB dye by the prepared photocatalysts under light irradiation..	100
Figure 3.37. Reuse performance of MNP-PEDOT-TiO <sub>2</sub> -AgNPs composite material.	104
Figure 3.38. Reuse performance of MNP-PEDOT-TiO <sub>2</sub> -AuNPs composite material.	104
Figure 3.39. Reuse performance of MNP-PEDOT-TiO <sub>2</sub> -AgAuNPs composite material.	105
Figure 3.40. LC-MS spectrum of MB before the photocatalytic reaction under solar light.	107
Figure 3.41. LC-MS spectrum of the photocatalytic degradation products of methylene blue by using TiO <sub>2</sub> nanoparticles as catalyst under solar light.	108
Figure 3.42. Comparison of the LC-MS data of the MB solution treated with TiO <sub>2</sub> nanoparticles and MNP-PEDOT-TiO <sub>2</sub> -AgAuNPs under solar light.	109
Figure 3.43. Control experiment for photocatalytic hydrogen evolution, a time-dependent variation of the volume of the gas mixture obtained from 50 mL water-ethanol mixture under 150 W UV light exposure in the absence of a catalyst.	111
Figure 3.44. GC chromatogram which shows the composition of gas obtained from 50 mL water-ethanol mixture under 150 W UV light exposure at the end of the control experiment.	112
Figure 3.45. Time-dependent variation of the volume of the gas mixture obtained from photocatalytic hydrogen evolution from 50 mL water-ethanol mixture under 150 W UV light exposure by using 20 mg TiO <sub>2</sub> nanoparticles as a catalyst.	113
Figure 3.46. Time-dependent variation of the volume of the gas mixture obtained from photocatalytic hydrogen evolution from 50 mL water-ethanol mixture under 150 W UV light exposure by using 20 mg MNP-PEDOT as a catalyst.	114
Figure 3.47. Time-dependent variation of the volume of the gas mixture obtained from photocatalytic hydrogen evolution from 50 mL water-ethanol mixture under 150 W UV light exposure by using 20 mg MNP-PEDOT-TiO <sub>2</sub> as a catalyst.	115

Figure 3.48. Time-dependent variation of the volume of the gas mixture obtained from photocatalytic hydrogen evolution from 50 mL water-ethanol mixture under 150 W UV light exposure by using 20 mg MNP-PEDOT-TiO <sub>2</sub> -AgNPs as a catalyst which contains 0.86 % (w/w), Ag.....	117
Figure 3.49. Time-dependent variation of the volume of the gas mixture obtained from photocatalytic hydrogen evolution from 50 mL water-ethanol mixture under 150 W UV light exposure by using 20 mg MNP-PEDOT-TiO <sub>2</sub> -AuNPs as a catalyst which contains 0.32 % (w/w), Au.....	118
Figure 3.50. Time-dependent variation of the volume of the gas mixture obtained from photocatalytic hydrogen evolution from 50 mL water-ethanol mixture under 150 W UV light exposure by using 20 mg MNP-PEDOT-TiO <sub>2</sub> -AgAuNPs as a catalyst which contains 0.79 % (w/w) Ag and 0.28 % (w/w) Au. ....	119
Figure 3.51. Comparison of the gas formation capability of catalysts prepared during this study. ....	120
Figure 3.52. GC chromatogram showing the composition of gas obtained from 50 mL water-ethanol mixture by using MNP-PEDOT-TiO <sub>2</sub> composite material as photocatalyst under 150 W UV light exposure. ....	121

## LIST OF ABBREVIATIONS

AA	Ascorbic acid
AOPs	Advanced oxidation processes
APTMS	(3-aminopropyl) trimethoxysilane
BET	Brunauer-Emmett-Teller
CB	Conduction band
CPs	Conducting polymers
EDOT	3,4-ethylenedioxythiophene
EDX	Energy dispersive X-ray spectrometer
GC	Gas chromatography
ICP-OES	Inductively coupled plasma optical emission spectrometry
LC-MS	Liquid chromatography - mass spectrometry
MB	Methylene blue
MNPs	Magnetic nanoparticles
NPs	Nanoparticles
PEDOT	Poly (3,4-ethylenedioxythiophene)
PPMS	Physical properties measurement system
SEM	Scanning electron microscopy
TEM	Transmission electron microscopy
TEOS	Tetraethyl orthosilicate
UV-Vis	Ultraviolet-visible



VB	Valence band
VSM	Vibrating sample magnetometer



## **CHAPTER 1**

### **INTRODUCTION**

Energy production and environmental troubles are of great concerns that society faces recently. Due to an exponential increase in human population and developments in the economy, the demand for energy sources and environmental issues increase extremely with a large scale. For thousands of years, the ecosystem that humankind is living stored a large amount of carbon dioxide (CO<sub>2</sub>) and different harmful chemicals in the water of underground and oceans.

Especially, mining activities, vehicle emissions, and disposal of toxic industrial effluents are responsible for the major pollution problems in the world. On the other hand, if the rate of fossil fuel consumption and environmental pollution increases more, the amount of greenhouse gases, heavy metals, phenol, ammonia, and sulfur-containing compounds in the atmosphere and water sources increases. Such effluents and chemicals are responsible for several chronic diseases and unhealthy for endocrine systems in human.

In fact, all the living beings in the world are under direct risk. It is crucial to develop renewable energy sources and technologies for environmental troubles to solve problems related to both energy demand and environmental remediation. Otherwise, as time progresses, the environment and mankind will be damaged adversely.

Recently, sunlight assisted photochemical reactions that use the mechanisms of advanced oxidation processes (AOPs) are preferred because such processes are totally environmentally-friendly that they are capable of degrading several types of toxic contaminants into nontoxic products. AOPs include the photocatalytic process in

which reactions are taking place by semiconductor under exposure of light. Therefore, such photocatalytic processes can be used effectively to solve the problems related to energy crises and elimination of environmental pollutants under a range of the solar spectrum. However, several photocatalysts mainly absorb ultraviolet light, so that they exhibit low activity in utilizing solar light. Therefore, several methods have been investigated to enhance visible light absorption of semiconductor photocatalysts that include doping of metal and nonmetal species, dye sensitization and surface modification.

### **1.1. Energy**

Energy is an important part of society and it is required to enhance social and economic living standards in society. Since the beginning of mankind, several types of resources from wood to nuclear energy are utilized to generate energy. Reliable energy supply is important for heating, lighting, transport and industrial processes.

Energy resources can be classified as non-renewable and renewable. Nowadays, non-renewable energy sources such as coal, petroleum, and natural gas are utilized dominantly [1, 2]. Of these sources, coal has a lower cost and it provides a high amount of energy considering its weight compared to other forms of energy. However, it is one of the dirtiest forms of fossil fuels and its burning releases high amount of greenhouse gases into the atmosphere. On the other hand, coal mining is extremely dangerous and has adverse effects on the environment such as increased erosion, the release of hydrogen sulfide and explosive natural gases such as methane and especially collapsing of mine stopes [3].

Petroleum is the other widely utilized energy source in the world for fuel. It has a high energy density, easy extraction, and easy transport because of being in a liquid form by pipes or vehicles. It can be used in several industries as power plants to supply high demands for energy and transportation including cars, planes, etc. However, similar to the other forms of fossil fuel, petroleum is a limited source, it causes environmental pollution,

it produces high amount of greenhouse gases such as carbon dioxide, nitrous oxide and methane [4].

Finally, like another form of fossil fuels, natural gas is environmentally friendly compared to other nonrenewable energy sources, easier to transport, cheaper compared to other fossil fuel energy sources. On the other hand, it is extremely combustible, so that the event of leak can cause explosions [5,6].

Utilization of nonrenewable sources is considered as the principal reason for climate change. The increase in carbon concentration causes a large amount of greenhouse gas emissions that result in climate change and acid rains. On the other hand, the formation of toxic materials by these sources results in several illnesses causing the death of millions of people in the world [7]. Due to depletion and environmental concerns, renewable energy sources such as solar, wind, geothermal, biomass, hydropower and hydrogen energies are considered as an alternative for sustainable development in the future [8]. Especially, after the Kyoto protocol, unlimited, recycled and clean sources have been become at the center of concentration [9].

Of these sources, especially solar energy is environmentally friendly compared to other renewable options, sustainable, and abundant supply. However, its cost for initial setup is high, it is not constant supply which means that its efficiency is affected by environmental factors and finally storage and backup problems are faced. As a clean source, wind energy is simple and powerful, but it is noisy, besides it has high investment cost, access problems to remote places, and adverse effects on the ecosystem. As a renewable source, geothermal energy is abundant and clean, but it has a high cost because of heating and cooling systems, hydrogen sulfide emissions can be formed and geothermal power plants are vulnerable in certain areas. As an abundant source with a wide variety of feedstocks, biomass energy releases greenhouse gases, it requires a high amount of fertilizer and water, and it has limitation in supplying resource. And finally, as a clean source, hydropower is abundant and safe. It is cheaper than other traditional power plants, it is easily stored in reservoirs,

but, it can cause flooding of surrounding landscapes and it interrupts the ecology of the area [10,11].

### **1.1.1. Hydrogen Energy**

Although renewable sources are considered as alternative energy sources to fossil fuels, discontinuity and fluctuating nature of such sources require improving effective energy storage mediums. The storage of renewable energy can be provided in the form of electricity and chemical energy as for hydrogen energy case. For years, electricity is widely utilized as an energy storage medium and it is essential for our daily lives. On the other hand, as an energy source, hydrogen is considered as a promising clean energy source due to its superior features. As a chemical fuel, hydrogen can solve several problems related to global energy and environmental pollution. Firstly, it has higher energy conversion values compared to gasoline and natural gas. Secondly, the combustion process of hydrogen does not produce any greenhouse gases, so that it is extremely clean and sustainable energy of the future. Thirdly, as it is the most abundant element in the world, it can be produced from a wide range of hydrogen-containing materials. Moreover, the storage of hydrogen can be provided in different forms such as gas, liquid, chemical as metal hydrides and physical storage as a metal-organic framework so that transportation over a long distance is one of the important advantages of hydrogen.

Furthermore, it can be converted to several energy forms, and most importantly, the production, storage, and transportation of hydrogen do not have any adverse effect on the environment. Finally, hydrogen is not only important for energy production but also an essential chemical substance for chemical industry [12, 13].

Development of effective and low-cost materials for production of H<sub>2</sub> is main concerning for sustainable hydrogen economy. Currently, in the industry, the present hydrogen production is based on reformation (steam reforming) and gasification processes that utilize fossil fuels such as natural gas, oil, and coal. These processes can take advantages

of large scale production of hydrogen and low cost but result in the formation of carbon dioxide emissions.

The more promising other efforts for hydrogen production without carbon dioxide release can be mentioned as biomass by using microorganisms and fermentation [14, 15] and splitting by water [16]. Especially, biomass is an attractive route to produce a large amount of hydrogen in volumes. Other advantages of biomass technique are the formation of lower CO<sub>2</sub> emissions, an increase in the agricultural output due to residues conversion, lower cost due to a decrease in solid wastes [17]. On the other hand, hydrogen production by water splitting includes several processes such as electrolysis, photoelectrolysis, biophotolysis and thermally decomposition. Of these techniques, especially electrolysis is a commercial method with the efficiency of nearly 75 %. Although it is clean and water is abundant, the cost of hydrogen by water splitting is several times higher than fossil fuel based techniques [18].

After the discovery of hydrogen production by photoelectrochemical water splitting technique on n-type TiO<sub>2</sub> electrodes that were utilized as photoanode and Pt as a cathode, the technology for production of hydrogen with semiconductors by utilizing solar energy has gained great importance to solve energy problems in the world [19, 20]. In the study, while the light is irradiated with higher energy than that of the bandgap of TiO<sub>2</sub>, e-h pairs are formed in the conduction band (CB) and valence band (VB) of semiconducting material. The formed electrons migrate towards Pt cathode to produce H<sub>2</sub>, whereas holes produce O<sub>2</sub> [19]. Several photoelectrochemical cells have been designed after the mentioned publication. However, highly stable photoelectrodes with proper band gap energy are a big dilemma for hydrogen generation via photoelectrochemical methods. Previously, another solar hydrogen generation technique is recommended for hydrogen production such as photocatalytic or photochemical water splitting.

The main idea related to these techniques is to generate hydrogen via sunlight which is a powerful and continuous source of energy. On the other hand, during these methods, no

undesirable by-products are formed, which makes these techniques completely environmentally safe [21].

Recently, the efforts related to a combination of heterogeneous catalysis and solar energy have been made. In photocatalytic reactions, the catalysts utilized are semiconducting materials. As semiconductor-based photocatalytic techniques meet the demand related to the energy crisis and environmental problems, the development of novel semiconductor photocatalyst with high photocatalytic activity for hydrogen production has undergone considerable research. Until now, depending on the electronic configuration, several UV active semiconducting photocatalysts have been prepared and fundamentally classified into four groups: (1)  $d^0$  metal (such as  $Ti^{4+}$ ,  $Ta^{5+}$ ,  $W^{6+}$ ) oxide photocatalysts, (2)  $d^{10}$  metal ( $In^{3+}$ ,  $Ge^{4+}$ , and  $Sb^{5+}$ ) oxide photocatalysts, (3)  $f^0$  metal ( $Ce^{4+}$ ) oxide photocatalysts, and (4) non-oxide photocatalysts [22].

Among the photocatalytic systems, especially n-type semi-conductor metal sulfides (CdS) and oxides (such as  $TiO_2$ , ZnO,  $WO_3$ ) containing ones have gained great importance for hydrogen generation in terms of efficiency. According to the aforementioned photocatalytic systems reported in the literature, because of the large bandgap of semiconducting materials, the activity of photocatalyst was only achieved under UV light exposure. The other disadvantages of such catalysts are that lower stability in aqueous medium resulting in the aggregation and therefore decrease in reaction sites, and fast recombination rates of e-h pairs [22, 23].

Hydrogen generation by using photocatalytic process involves mainly three steps. Firstly, absorption of light irradiation resulting in the formation of  $e^-/h^+$  pairs. Secondly, the migration of charge carriers in semiconductor, and finally surface chemical reactions are taking place among these carriers and several compounds such as  $H_2O$  [22]. Several modifications are done to decrease the band gap of such photocatalysts and therefore, to increase photocatalytic activity with enhanced stability.



## **1.2. Environmental Remediation**

Elimination of harmful and toxic chemicals from the air, soil and water, treatment of contaminated sites to change the harmful chemicals to less harmful ones, embedding of polluting materials in the ground while preventing them from permeating into the soil, water and air is stated as 'remediation'. Recently, several remedial techniques have been investigated to overcome the problems related to environmental pollution and therefore, to meet the site remediation goals. As various remediation technologies are available today, selecting the most suitable technique has become crucial to achieve successful cleaning up of contaminated sites [24]. One of the major and crucial problems of the modern world is environmental pollution. Industries are the greatest source of pollution, especially the textile industry produces a large amount of liquid effluents as pollutants during fabric processing [24].

Industrially, ten thousands of various synthetic dyes and pigments are utilized, and hundreds of thousands of tons of dyestuffs are produced worldwide. Up-to-date technology, dyes can be utilized in several fields such as in the textile industry, leather tanning, paper production, medicine, cosmetics, agricultural, etc. [24]. Especially, the textile industry consumes a high amount of water during manufacturing processes utilized in dyeing and other operations of production. Unfortunately, most of these dyes escape and therefore, dye-containing wastewater from textile plants is considering the most polluting source for environmental pollution in all other industrial sectors.

Synthetic dyes are one of the most important contaminants in wastewater, because a tiny amount of dyes (less than 1 ppm) in water are extremely visible, and they reflect the sunlight while preventing penetration of sunlight into water. This affects aquatic species growth adversely and prevents photosynthesis. Moreover, depending on the amount of dye and exposure time, living organisms in water can negatively be affected in terms of acute and chronic inflammation [24]. The first and fundamental concern is to the removal of the

dye from wastewater, but the point of degradation dye is not only to remove color, but also to eliminate and decrease the toxicity of such pollutants.

Due to the increased demand for textile products, nowadays, removal of harmful substances, especially mutagenic, carcinogenic and allergenic textile chemicals, and dyes from wastewater have gained great importance. Wide range of technologies have been developed to decrease their environmental impact in different countries. Wastewater remediation is not only based in decolorization of dye but also degradation of dye molecules. In fact, decolorization occurs when the dye molecules are removed from the solution or when the bonds of chromophore are broken, but major fragments of dye still remain in the effluents [25].

The methods for dye removal can be classified as physical methods such as membrane-filtration processes (nano-filtration, reverse osmosis, electrodialysis) and sorption techniques, chemical methods such as coagulation and flocculation, conventional oxidation methods (with ozone), irradiation or electrochemical techniques, and biological methods such as aerobic and anaerobic microbial degradation and use of pure enzymes [26]. All these mentioned techniques have several advantages and disadvantages. Due to the chemical stability of synthetic dyes, traditional treatment techniques for wastewater are clearly inefficient. Furthermore, these methods do not solve the concerns related to water recycling problem.

Mainly the disadvantages of physical methods are their high cost, low efficiency, special equipment requirements, and further care for this equipment is required. For example, considering as the most effective physical technique, in membrane-based techniques, membrane fouling, membrane cleaning and corrosion of membrane with time are the drawbacks of such techniques. Color can be effectively removed via physical methods, but such methods cannot provide degradation of dye molecules so that proper disposal is required. With chemical techniques, although dye molecules are degraded, there is still a disposal problem. Furthermore, secondary pollution problem arises due to the usage of an

excessive amount of chemicals in such techniques. Finally, biological methods are known as environmentally friendly because these techniques can provide mineralization of pollutants completely with low cost. The main limitation is that some dyes are highly stable and very resistant to biodegradation due to poor adsorption onto the surface. On the other hand, biological techniques are time consuming and inconvenient, making such techniques unpractical for high sample amount [27].

The new emerging technique, called advanced oxidation processes (AOPs) can be successfully applied for the treatment of contaminated and industrial wastewater containing an excessive amount of pollutants. Such techniques are also proper for purification and disinfection of drinking water. AOPs involve the formation of highly reactive chemical oxidants such as hydroxyl radicals to increase the oxidation and degradation rate of organic pollutants from wastewater. The hydroxyl radicals are powerful, nonselective and very reactive oxidants so that they can easily react with most of the organic pollutants.

### **1.3. Advanced Oxidation Processes (AOPs)**

Advanced oxidation processes (AOPs) are environmentally friendly, promising and effective techniques for the removal of organic pollutants from waters and wastewaters. In these processes, the generation of powerful oxidizing agents such as hydroxyl radicals ( $\bullet\text{OH}$ ) is taking place with a sufficient concentration in order to efficiently decontaminate waters. Main types of AOPs can be classified as chemical, sonochemical, electrochemical and photochemical reactions.

As water treatment process, AOPs were firstly defined by Glaze et al. in 1987 [28]. The method involving the generation of hydroxyl radicals was performed at room temperature under normal pressure to decontaminate waters efficiently. After then, several numbers of research works were published related to AOPs and such techniques have gained great importance due to effective degradation and destruction

of organic pollutants in aquatic media [29]. Of the AOPs the oldest one is the Fenton method, in which iron (II) salt and  $\text{H}_2\text{O}_2$  are used as Fenton's reagent for degradation of organic pollutants [30]. However, it is necessary to enhance oxidation efficiency during treatment of environmental water sample by ultraviolet (UV) light or sunlight. Although Fenton's chemistry started with the study published at the end of the nineteenth century for the oxidation of tartaric acid by using Fenton's reagent, in recent studies, the mechanism of the Fenton process was demonstrated clearly. According to these demonstrations, the Fenton process was started with the formation of hydroxyl radical and such processes can be utilized in the degradation of several organic pollutants [31]. Experimentally, by chemical probes or spectroscopic techniques, the formation of hydroxyl radicals was supported [32].

The efficiency of Fenton's reagent directly changes with several factors such as temperature, pH, and concentrations of  $\text{H}_2\text{O}_2$  and catalyst. For wastewater treatment, the advantages of Fenton process compared to other oxidation techniques is that no energy input is required to provide activation of  $\text{H}_2\text{O}_2$ , it has short reaction times with easy-to-handle chemicals [33], nevertheless, the main disadvantages are high cost of hydrogen peroxide with its risky storage and transportation, and besides, at the end of treatment, iron salt forms Fe (III)-carboxylic acid complexes (iron sludge), therefore additional separation is required to avoid further water pollution. In order to minimize the disadvantages of Fenton processes, the concentration of  $\text{H}_2\text{O}_2$  added can be reduced and the formation of iron sludge can be prevented by catalysts such as zeolites, alumina, molecular sieves or by using ion-exchange resins, or membranes [33].

The other type of AOPs is sonochemical AOP which utilizes ultrasounds in an aqueous medium. The technique has mainly two mechanisms, named as chemical (indirect) and physical (direct) mechanisms. In the first one, water and oxygen molecules undergo homolytic cleavage with high frequency to generate  $\bullet\text{OH}$ ,  $\text{HO}_2\bullet$ , and  $\bullet\text{O}$  radicals [34]. In the direct mechanism, also called as sonication, ultrasounds

form cavitation bubbles that growing and collapsing of these bubbles result in the formation of breaking forces with high temperatures (5000 K) and pressures ( $6 \times 10^4$  kPa). In these severe conditions, due to sonolysis of water molecules, generation of reactive radicals is taking place to react with chemicals in an aqueous medium or to degrade organic compounds [35].

The important disadvantage of this water treatment technique is that by ultrasounds, sufficient number of hydroxyl radicals cannot be formed so that other oxidizing agents such as hydrogen peroxide is required and also UV irradiation should be applied at the same time. Furthermore, the method should be combined with other AOPs such as Fenton-type reactions. In sonochemical AOP treatment, several important parameters should be considered such as ultrasonic frequency, pH of the solution, amount and type of iron precursors to increase the performance of such treatments for pollutants in water. On the other hand, as well as the properties of pollutants such as nature and amount, the experimental conditions such as reactor type, size of the reactor and exposure time have an important effect on the efficiency of these methods [35].

As the third type of AOPs, electrochemical AOP provide an extremely clean and efficient way to generate hydroxyl radical to destroy a large amount of organic pollutants. It is one of the most popular electrochemical techniques for wastewater remediation. The technique involves oxidation of pollutants in an electrolytic cell. In the electrochemical process, hydroxyl radicals can be electrochemically generated directly via electron transfer to the anode or electrocatalytically by using Fenton's reagent. The efficiency of the process can be increased by combining these two electrochemical processes.

For the treatment of wastewater, high cell voltages are applied to achieve oxidation of pollutants in water directly. Anode material in these techniques is important to concern because either electrochemical conversion or combustion reaction is taking place directly depending on the anode material. Such electrochemical processes have gained

great importance in recent years because of the several advantages that these processes offer. Besides being environmentally safe, these processes can operate at ambient temperature and pressure, they don't need any chemical reagents or catalyst to generate hydroxyl radicals and do not form waste. However, a drawback of electrochemical processes is that reaction rates are typically slower than other AOPs because pollutants must diffuse to the surface of relatively high costs of electrodes in order to react [36].

The final type of AOPs is the photochemical technologies in which UV or Vis light radiations are coupled with strong oxidizing agents such as  $O_3$  and  $H_2O_2$  or a catalyst with  $Fe^{3+}$  or  $TiO_2$ . The mentioned photochemical processes can degrade pollutants by several reactions named as photodecomposition under UV light, excitation and degradation of pollutants, and oxidation via  $O_3$ ,  $H_2O_2$ , and oxidation via  $Fe^{3+}$  and  $TiO_2$ . The photochemical AOPs can be classified as  $H_2O_2$  photolysis ( $H_2O_2/UV$ ),  $O_3$  photolysis ( $O_3/UV$ ), photo-Fenton process ( $H_2O_2/Fe^{2+}/UV$ ), and heterogeneous photocatalysis ( $TiO_2/UV$ ) [37]. In the photolysis of  $H_2O_2$ , UV radiations with the wavelength of 200-300 nm range, provide photolysis of hydrogen peroxide causing the homolytic cleavage of the O-O bond and therefore leading to the generation of hydroxyl radicals. These radicals also cause the decomposition of hydrogen peroxide molecules with secondary reactions. It is important to note that the rate of generation of free radicals directly depends on the several crucial parameters such as the power of UV lamps, and physicochemical properties of solutions such as pH, temperature turbidity and so on.  $H_2O_2/UV$  AOP is generally taking place in an alkaline medium with large reaction rates.

UV radiation activates hydrogen peroxide resulting in the generation of hydroxyl radicals. However, one drawback of this AOP is that relatively high concentration of hydrogen peroxide is required to achieve efficient oxidation of pollutants due to low absorption of hydrogen peroxide in UV region, but an excessive concentration may also cause a reduction in the rate of oxidation due to scavenging effect of  $H_2O_2$  [38].

In O<sub>3</sub>/UV process, the photolysis of ozone in aqueous solution is taking place with UV irradiation between the range of 200-360 nm. As ozone absorption of UV light occurs at 254 nm, as UV source, low-pressure mercury vapor UV lamps are commonly used for this process. Since the absorption coefficient value of ozone is larger than that of hydrogen peroxide at this wavelength, this process is more effective compared to photolysis of H<sub>2</sub>O<sub>2</sub>/UV, so that, photolysis of ozone process is widely utilized for the removal of pesticides and phenols in wastewaters [39]. The photolysis of ozone in aqueous solutions causes the formation of hydrogen peroxide that initiates the decomposition of remained ozone into hydroxyl radicals. Due to being highly reactive species, ozone and hydroxyl radicals are commonly used as an oxidizer in drinking water treatment.

In the photo-Fenton (H<sub>2</sub>O<sub>2</sub>/Fe<sup>2+</sup>/UV) process, the classical Fenton reaction is assisted via UV light irradiation to achieve a catalytic reduction of Fe<sup>3+</sup> into Fe<sup>2+</sup> in hydrogen peroxide solutions to increase the number of hydroxyl radicals [40]. As the photo-generated ferrous ions enter Fenton reaction to produce extra hydroxyl radicals, the oxidation rate of photo-assisted Fenton reactions is higher than that of classical Fenton process. Furthermore, an advantage of the photo-Fenton process, total iron usage, and sludge generation are less compared to Fenton reaction [41]. However, in photo-Fenton process, the intensity and wavelength of UV light irradiation have a crucial effect on degradation of pollutants so that utilization of artificial light is an important drawback of this process in terms of cost-effectiveness.

Nowadays, solar photo-Fenton AOP is an alternative to UV assisted photo-Fenton process that has been used to destroy several organic compounds in polluted waters, to degrade the herbicides and to treat wastewater effluents [42]. The final photochemical AOP is heterogeneous photocatalysis with semiconducting material TiO<sub>2</sub> under UV light exposure. In 1972, Fujishima and Honda explained that photoexcited TiO<sub>2</sub> can be utilized to split water into hydrogen and oxygen with photo-electrochemical solar cell [43]. This work was important to lead for the development

of new advanced oxidation process. The process depends on the utilization of semiconducting material for application in environmental concerns and energy production.

In the heterogeneous photocatalytic process, a semiconducting material, generally  $\text{TiO}_2$ , is utilized due to several crucial aspects. Firstly, it is stable and inert. The production of  $\text{TiO}_2$  is easy and relatively inexpensive compared to other semiconducting materials [44]. When the absorbed photons have higher energy than the energy gap of semiconducting material, e-h pairs are generated and these pairs migrate to the surface of a semiconductor to degrade pollutants adsorbed onto the surface. Photogenerated e-h pairs are strong oxidizing and reducing agents to form hydroxyl and superoxide radicals.

During the photocatalytic process, the photogenerated holes can directly oxidize the pollutants or oxidize hydroxyl groups adsorbed onto the surface of a semiconductor to form hydroxyl radicals to degrade pollutants indirectly which is the most favorable pathway for degradation. In the heterogeneous photocatalytic process,  $\text{TiO}_2$  can be utilized as a thin film on support materials [45] or as either powder in aqueous suspension [46]. For thin films, at the end of the process, there is no need to remove the catalyst, but the layer of catalyst should be stable and active on the supporting material. Besides, the amount and type of catalyst directly depend on the source of light and the concentration of pollutant. Moreover, the pH of the reaction medium should be optimized firstly depending on the type of pollutant. On the other hand, the dispersed catalyst can be easily used, and it has a large surface area which increases the efficiency of the catalyst significantly [46].

The heterogeneous photocatalysts have been widely used for degradation of organic pollutants recently. Besides, this technology can be also efficient to destroy pathogens such as viruses, bacteria and so on in water effluents [47]. More importantly, the photocatalysts can also be modified as visible light active with several strategies such



as dopants (nonmetal or metal), dye sensitizations, and coupling with different semiconducting materials [48].

With such photocatalysts, toxic chemicals such as cyanide, nitride, and sulfite can be oxidized to nontoxic or relatively less toxic compounds such as CO<sub>2</sub>, nitrate, and sulfate [49]. Furthermore, they can also be utilized to degrade or mineralize several pollutants such as pesticides, pharmaceuticals, surfactants, sulfur-containing organic compounds, dyes and so on [50].

According to the type of materials involved, the photocatalyst can be classified as a molecular photocatalyst, semiconducting photocatalysts, quantum dots, two dimensional (2D) photocatalysts, plasmonic metal photocatalysts and traditional semiconductor-based photovoltaic assisted catalysts [51]. Each photocatalyst has different principles so that in order to describe their system, the type of photocatalyst should be considered. For example, when the molecular photocatalysts are considered the molecular orbital (HOMO-LUMO) levels of the photocatalyst with molecular orbitals of reactant molecules are necessary [52]. For semiconductors, band gap and band theory become important [53].

When the size of the photocatalyst is small as Bohr radii of excitons, which is the distance in an e-h pair, the quantum effect becomes dominant in which optical and electrical properties change with size [54]. This is the situation in which quantum dots are utilized as photocatalyst. When the size is small enough (less than 10 nm), materials that have conduction property, such as carbon dots can become semiconducting material making such materials to be used as photocatalyst.

Ultrathin films, transition metal oxides, and dichalcogenides are examples of 2D materials that can be used as another type of photocatalyst. This class of materials due to their unique structures provide intended anisotropy for charge separation to apply the material as photocatalyst [55]. On the other hand, plasmonic metal photocatalysts

are desirable due to their plasmonic effects for photocatalytic applications [56]. Finally, in the semiconductor-based photovoltaic assisted catalyst, absorption of light results in charge separation and the catalytic process is taking place on semiconductor containing photovoltaic devices. In this process, renewable electrical energy such as wind can also be replaced with photovoltaic component [57].

#### **1.4. Semiconductors for Photocatalysis**

Of the mentioned photocatalysts, recently especially semiconductor photocatalysts have gained great importance. Semiconductors can be examined as both particulate and film-like configurations. The dispersion of particulates of photocatalyst provides better photocatalytic activity while evaluating the performance of it. This simplicity makes particulate semiconductor photocatalysts most popular compared to other type of photocatalysts.

The semiconductor photocatalyst can be prepared as different morphologies such as solid spheres, hollow structure, and asymmetric morphologies. The widely used semiconductors as photocatalysts are Si, Ta<sub>3</sub>N<sub>5</sub>, TiO<sub>2</sub>, BiVO<sub>4</sub>, Fe<sub>2</sub>O<sub>3</sub>, WO<sub>3</sub>, ZnO, Cu<sub>2</sub>O, Ag<sub>3</sub>PO<sub>4</sub>, CdS, and GaAs/InGaP). Recently, researches have been focused on the facile synthetic procedure of nanoparticles such as co-precipitation, hydrothermal precipitation, ultrasonic exfoliation and ball milling [51].

A typical particulate semiconductor system contains photocatalyst and reactive medium that reduction and oxidation reactions are taking place on the surface of photocatalyst. To prevent precipitation or agglomeration of particles in the medium and to increase absorption of light, stirring or flow agitation is necessary.

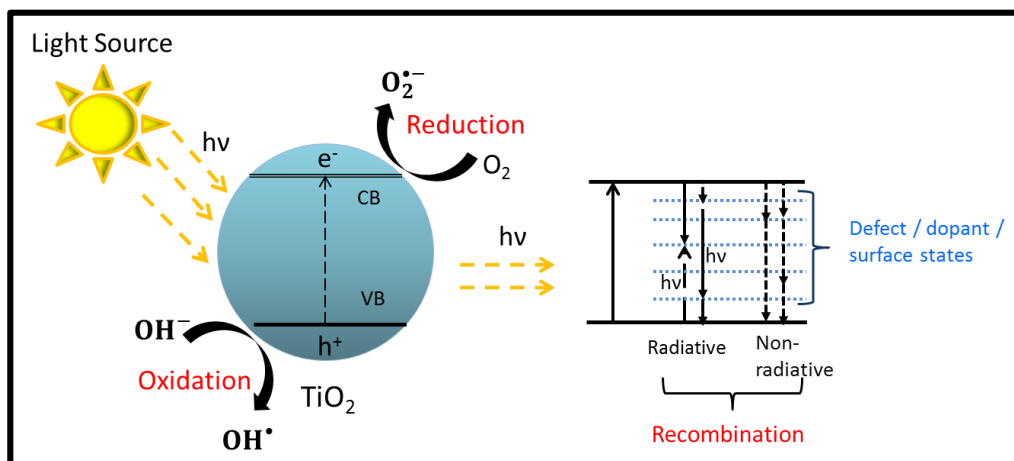
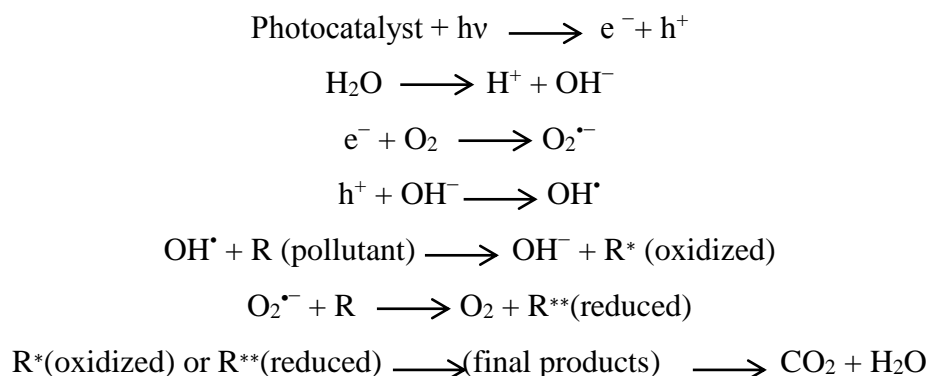


Figure 1.1. Schematic diagram of the mechanism of photocatalyst [58].

In semiconductor photocatalyst, when light has equal or greater energy than that of the band gap of the semiconductor, electron and hole pairs generate. Photogenerated electrons would be excited from the valence band to the conduction band of the semiconductor and holes would be left in the valence band. These photogenerated pairs migrate to separated sites on the surface of photocatalyst.

On the surface, redox reactions are taking place. In the process, photogenerated electrons reduce O<sub>2</sub> molecules to O<sub>2</sub><sup>•-</sup> radicals, and holes oxidize H<sub>2</sub>O to generate •OH radicals. Figure 1.1. shows the schematic diagram of the mechanism of the photocatalyst.

The reactions which are taking place are given below:



The formed radicals have long enough lifetimes to oxidize dye pollutants such as methylene blue, methyl orange, and rhodamine B. The semiconductor photocatalysts can perform catalytic activity from ultraviolet (UV) and visible spectrum of light depending on the bandgap and electronic structure of the photocatalyst.

The semiconductor photocatalysts have advantages such as low manufacturing cost, non-toxicity, having a high surface area, and high amount of active sites, having simple preparation for large scale applications, short charge diffusion distance which is important to decrease bulk charge recombination, and showing tunable properties when modified with dopants, sensitizers, etc. Besides, with photocatalytic technique, complete degradation of pollutants can be achieved so that the method does not leave a trace amount of pollutants. However, removal of catalyst from the reaction medium, serious surface charge recombination, poor chemical stability due to the large surface area can be serious problems for such systems. In order to obtain better photocatalytic activity, a semiconductor having a lower band gap energy should be chosen. Besides, the cost, easy production, stability in the reaction medium, being eco-friendly, and effectiveness are the crucial parameters that should be considered for the selection of photocatalyst [59].

### 1.4.1. TiO<sub>2</sub> as a Photocatalyst

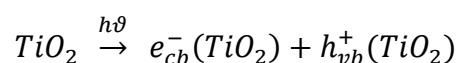
Of all the aforementioned semiconductors, titanium dioxide (TiO<sub>2</sub>) seems to be the best semiconducting material as a photocatalyst due to several desirable properties. For example, it has high ultraviolet absorption, high stability, low cost and non-toxicity making it to be utilized in several applications such as electroceramics, glass and degradation of pollutants photocatalytically in water and air [60].

The most common crystalline forms of TiO<sub>2</sub> are anatase and rutile. There is also brookite crystalline form of TiO<sub>2</sub>, but it is uncommon and unstable. Anatase form is the most stable crystalline of TiO<sub>2</sub> with a formation heat as 8-12 kJ/mol [61], and at high temperatures, nearly as 700 °C, it can be converted to rutile structure depending on the size of the crystallite and impurity. The density of rutile (4.26 g/mL) is greater than the anatase (3.9 g/mL) form. The reduced density between these two crystalline forms causes crucial differences in physical properties. Although rutile structure (E<sub>g</sub> = 3.0 eV) is expected as a better photocatalytic activity, anatase (E<sub>g</sub> = 3.2 eV) form exhibits more performance than rutile due to having an open structure compared to rutile. Besides, the anatase form has a higher density of localized states, the higher probability of hydroxyl radicals on the surface adsorbed, better chemical stability and slower recombination of charge carriers [62].

Degussa P25 is the most widely utilized and commercial TiO<sub>2</sub> that is a mixture of rutile (15 %) and anatase (85 %) phases as well as some amorphous phases of TiO<sub>2</sub> placed in the structure. It exhibits excellent photocatalytic activity which is related to the mixed phase composition and anatase crystallinity which provides a photoinduced charge separation and a large surface area (nearly 55 m<sup>2</sup>g<sup>-1</sup>) [63]. These two important factors affect photocatalytic activity because, for example, high anatase crystallinity means that there are few defects in the structure that these defects act as recombination centers for electron-hole pairs. High crystallinity increases the probability of photocatalytic reactions so that it enhances the performance of photocatalyst. On the

other hand, the large surface area of Degussa P25 is an advantage for photocatalytic reactions that are taking place on the surface. Because as the photocatalytic reactions occur when the organic pollutants adsorb onto the surface, the large surface area favors this important step with enhancing the activity of the catalyst.

The photocatalysis of TiO<sub>2</sub> is initiated by the absorption of the photons with energy equal or greater than that of the band gap of it. This results in the generation of electron-hole pairs as shown in the equation below.



After exposure of light, TiO<sub>2</sub> can act as both electron donor and acceptor for the surrounding molecules. The charges can react with either adsorbed pollutants and water molecules in the reaction medium. However, as the major component of the solution is water, reactions with water are more likely to occur compared to pollutant molecules. Oxidation of water or hydroxyl ions by holes form hydroxyl radicals that are highly powerful and non-selective oxidant. The oxidation potential of hydroxyl radical (<sup>•</sup>OH) is 2.86 V. For comparison, other materials that can be utilized for disinfection of water can be given as ozone (2.07 V), H<sub>2</sub>O<sub>2</sub> (1.78 V), chlorine (1.36 V) and ClO<sub>2</sub> (1.27 V) [64]. Hydroxyl radicals are the most significant radicals attacking contaminant molecules at the surface during the photocatalytic process of TiO<sub>2</sub>. On the other hand, the generation of superoxide radicals from oxygen molecules is the other reaction taking place at the surface. This reaction prevents recombination of electrons with hole and provides an accumulation of oxygen radicals that also attacks the pollutant molecules adsorbed [65]. Until now, the photocatalytic property of TiO<sub>2</sub> has been utilized in dye-synthesized solar cells [66], sensors [67], hydrogen generation via water splitting method [68], photocatalytic reduction of CO<sub>2</sub> [69] and for remediation of various biological species [70].

The properties and activity of TiO<sub>2</sub> depend on surface structure such as surface area, porosity, defects and experimental conditions such as the concentration of pollutants, amount of catalyst, pH, temperature, and intensity of light and irradiation time.

Surface morphology, or in detail sizes of particle and agglomerates affect photocatalytic activity in the oxidation process. Until now, several forms of TiO<sub>2</sub> have been produced with several techniques to obtain photocatalyst with proper physical properties, performance, and stability for applications. When the size of nanoparticle decreases, due to the increase in surface area, higher conversion in organic pollutants can be obtained [71].

As another condition, porosity provides considerable internal surface areas, abundant surface states for catalytic conversion of molecules. Therefore, the introduction of porous structure into photocatalyst increases active sites which are necessary for catalysis. That is, photocatalysts with porous structure may show enhanced catalytic activity [72]. As reported, bulk and surface defects on TiO<sub>2</sub> are crucial factors that affect the activity of the catalyst, as they change its optical and electrical properties. As bulk defects cause recombination of e-h pairs, migration of these charge carriers are prevented. Such defects can trap photo-generated electrons with electrostatic interaction and therefore limit the increase in activity of photocatalyst. In contrast, surface defects and oxygen vacancies behave as trapping and adsorption sites while transferring the charge to adsorbed species making charge carrier separation easily. The surface defects capture the electrons promoting the recombination of charge carriers. Therefore, surface defects may facilitate the enhancement in photocatalytic activity [73].

When photocatalytic oxidation is taking place, the concentration of organic pollutant decreases depending on the performance of photocatalyst as time passes. However, at too high pollutant concentrations, the surface of TiO<sub>2</sub> becomes saturated causing the

deactivation of photocatalyst due to less electron-hole pair generation so that photocatalytic activity diminishes [74].

According to literature, the amount of the photocatalyst is the other parameter that should be considered. In photocatalytic reactions, the rate of reaction is directly affected by the concentration of catalyst so that photocatalytic degradation increases with the amount of catalyst loading. However, for better results, the optimum catalyst dose should be determined to avoid using an excess catalyst with unfavorable light scattering and reduction in light penetration at the same time. Above the amount of optimum dose, decrease in degradation efficiency may be observed [75].

Another crucial parameter in photocatalytic reactions is the pH of the reaction medium. When the pH of the solution is lower than 6.9, the surface of TiO<sub>2</sub> is positively charged, whereas, in alkaline medium higher than 6.9, the surface is negatively charged. Protonation and deprotonation of titanium can be explained by the following reactions:



The pH of solution influences the surface charge of TiO<sub>2</sub>, therefore adsorption of pollutant molecules onto the surface changes. Besides, proper pH should be adjusted to prevent agglomeration of nanoparticles during the photocatalytic reaction. TiO<sub>2</sub> is reported to exhibit better catalytic activity at lower pH nearly at 5, but a further decrease in pH may decrease the rate of the reaction due to electrostatic repulsion between catalyst surface and pollutants [76].

During the photocatalytic processes, generation of heat by a UV lamp or an external source affects reaction pathways and reaction rate of degradation. According to



experimental studies related with a degradation rate of organic compounds by temperature is that generally increase in temperature causes recombination of charge carriers and desorption of the organic compounds adsorbed onto the surface, therefore it decreases photocatalytic activity [77].

Light intensity is the other important parameter in photocatalytic systems. Reaction rate largely depends on light absorption of catalyst. On the other hand, the reaction pathway is not influenced by the light source. That is, the mechanism of band gap sensitization does not change depending on nature or form of light. It has been shown that when light intensity is in the range of 0-20 mW/cm<sup>2</sup>, the rate of photocatalytic reaction increases linearly. On the other hand, with the exposure of intermediate light which is in the range of 20-30 mW/cm<sup>2</sup>, the rate of reaction depends on the square root of light intensity. It was also reported that higher light intensity does not have any effect on the rate. This can be explained as, at a low light intensity, the formation of electron-hole pairs is predominant and recombination is negligible.

On the other hand, at higher light intensities, there is a competition between electron-hole pair separation and recombination decreasing the effect of light intensity on the rate of reaction. The slow kinetics of degradation of dye molecules after a certain time can be explained by reaction of short-chain aliphatic with hydroxyl radicals and a short lifetime of photocatalyst due to active site deactivation by side product deposition [78]. When natural sunlight is utilized for photosensitization of TiO<sub>2</sub>, only about 5% of light irradiation of this catalyst has proper energy. Furthermore, reflection and transmission of light cause energy loss in the application of catalysts in photo processes [79]. In order to increase the absorption property of TiO<sub>2</sub>, and therefore to enhance photocatalytic activity with exposure of visible light, new strategies should be performed.

Currently, several efforts are applied to enhance the band gap of TiO<sub>2</sub> for increasing photocatalytic performance. These efforts can be classified as changing shape (nanowires, nanoparticles, etc.) [80], size [81] dopants (nitrogen, metal, and carbon) [82], and production of composites and heterostructures.

## **1.5. Doping of Semiconductors**

In order to enhance visible light absorption of semiconductor photocatalysts with improved stability, several modification techniques can be applied such as noble metal loading, ion doping, dye sensitization and addition of conjugated polymers to the structure.

### **1.5.1. Nobel Metal Doping**

Incorporation of noble metals onto the surface of semiconductors such as TiO<sub>2</sub> can extremely enhance the activity of catalyst under visible light. To design photocatalyst with high activity, understanding the enhancement mechanisms after doping noble metal nanoparticles to the surface of titania is important.

Several noble metals, including Ag, Au, Pt, Pd, and Cu on the surface of TiO<sub>2</sub> nanocomposites were reported for modification in order to enhance photocatalytic efficiency in redox processes and to extend absorption of visible light by semiconducting material [83,84].

Due to the distinct enhancement mechanisms under UV and visible light, the proposed mechanisms will be discussed separately. Under UV light irradiation, the important proposed mechanism is the charge separation mechanism, in which these energetic electrons are transferred from the conduction band of semiconductor to noble metal as shown in Figure 1.2.

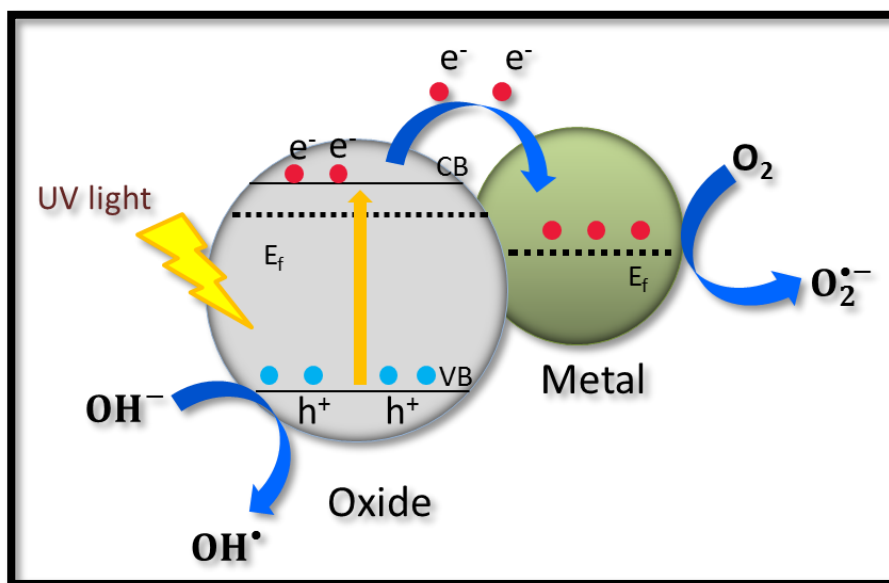


Figure 1.2. Schematic illustration of charge separation mechanism under UV light irradiation [85].

Figure 1.2 exhibits a schematic illustration of charge separation mechanism between metal and semiconductor. The metals have crucial roles on enhancing the photocatalytic activity in metal-semiconductor oxide composites. The enhancement in the photocatalytic activity of  $\text{TiO}_2$  can be explained by the decrease in the band gap or the addition of intra-band gap states by virtue of dopants. As the Fermi levels of plasmonic nanomaterials are lower than that of  $\text{TiO}_2$ , photoexcited electrons ( $e^-$ ) can be transferred to the conduction band of  $\text{TiO}_2$ . Therefore, electron-hole recombination is less likely to occur that results in effective charge separation and enhancement in photocatalytic performance [86].

The enhancement in photocatalytic activity is also attributed to Schottky junction due to contact between noble metal nanoparticles and semiconductor. Schottky barrier arises due to equilibrium in Fermi levels that results in the formation of a built-in electric field at the interface. This provides a better separation of e-h pairs that decreases recombination rate, and therefore the lifetime of e-h pairs increases as shown in Figure 1.3 [84,86].

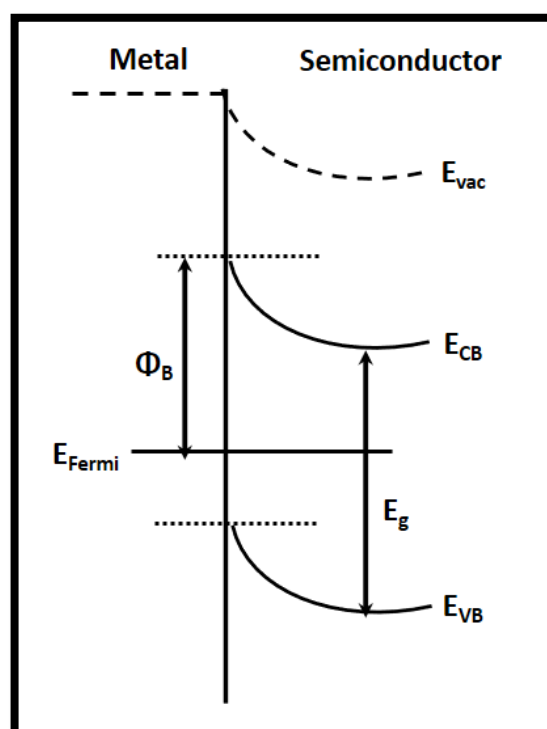


Figure 1.3. Schottky barrier between a metal and a semiconductor.  $E_g$  is the band gap of semiconductor and  $\Phi_B$  is the height of Schottky barrier [86].

Under visible light, enhancement in photocatalytic activity can be explained by charge transfer mechanism and the local electric field enhancement at the metal-semiconductor interface. In these proposed mechanisms, plasmonic nanoparticles absorb visible light strongly due to localized surface plasmon resonance (LSPR) acting as an antenna to concentrate light that facilitates the usage of such particles in photocatalytic applications [83]. This effect arises from the collective oscillations of electrons on the surface of noble metals, and these energetic electrons are transferred to the conduction band of semiconductor. At the same time, the collective oscillations of electrons in metal nanoparticles result in the enhancement of local electromagnetic fields at the interface of metal and semiconducting material as shown in Figure 1.4.

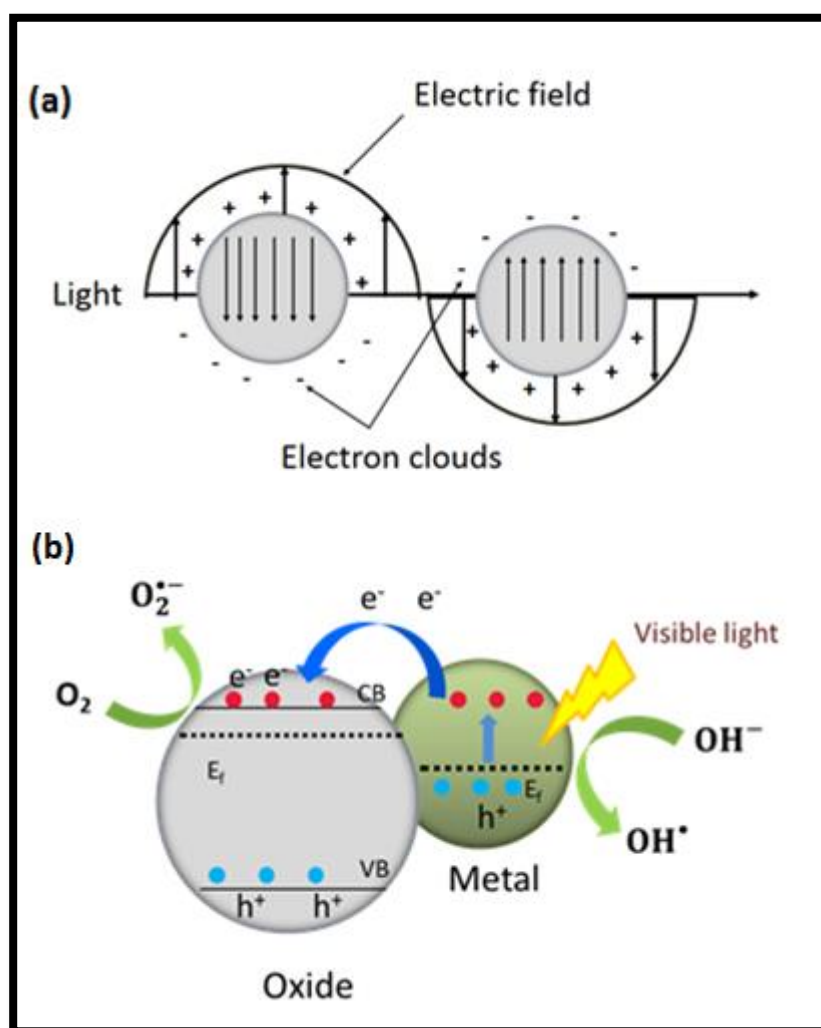


Figure 1.4. Schematic illustration of (a) surface plasmon resonance (b) charge separation mechanism under visible light irradiation [85].

Clearly, the addition of noble metal nanoparticles has several advantages such as retardation of electron-hole recombination, shifting of absorption of  $TiO_2$  from UV to visible light region, modification of surface properties of photocatalyst, increase in the number of hydroxyl radicals on the surface formed. However, the addition of the proper amount of metal is important to enhance the performance of photocatalyst, because there are also some disadvantages. For example, due to the high concentration of noble metal addition, metal clusters can be formed which cause the formation of barrier on the surface, and therefore, due to low absorption, photocatalytic activity

reduces. On the other hand, metal nanoparticles on the surface can also act as recombination centers that affects activity of catalyst. Therefore, the proper amount should be adjusted to produce noble metal decorated photocatalyst with an improved photocatalytic performance [87].

#### **1.5.1.1. Silver Nanoparticles Doped TiO<sub>2</sub>**

Ag, among the noble metals, is an excellent metal because of exhibiting intense surface plasmons at the wavelength range between 320-450 nm. This range is near the absorption band gap of TiO<sub>2</sub> which is 388 nm. The closeness of these values is important to decrease the rate of recombination. Silver addition to TiO<sub>2</sub> makes the structure proper to be utilized as photocatalyst with visible light exposure. Ag-TiO<sub>2</sub> photocatalysts are widely utilized in several applications in environmental remediation, antimicrobial activity and in oxidation reactions as catalysts, etc [88]. Deposition or doping of silver onto the surface of TiO<sub>2</sub> is necessary to produce Ag-TiO<sub>2</sub>. The deposition of silver onto the surface is generally achieved via wet impregnation technique [88]. Other techniques are hydrothermal method [89], sol-gel and modified sol-gel processes [90], microemulsion [88], photoreduction [91] and photodeposition [92]. After deposition, calcination, photo or chemical reduction is required to obtain silver nanoparticles on the surface.

In wet impregnation technique, TiO<sub>2</sub> nanoparticles are impregnated with aqueous or nonaqueous solutions of metal precursors such as nitrate, chloride, acetate and so on. The taken metal precursors as dopant are mixed with semiconductor in specific hydrophilic or hydrophobic solvent [93]. Sobana et al. examined the degradation of Direct red 23 and Direct blue 53 organic dyes via silver doped TiO<sub>2</sub> which was prepared with a wet impregnation technique. Degradation of dyes was enhanced with silver deposited TiO<sub>2</sub> because of lower electron-hole recombination provided by silver metal on the surface [94]. In literature, it was mentioned that silver nanoparticles on the surface can trap photogenerated electrons from TiO<sub>2</sub> and leave holes for

degradation. Furthermore, silver nanoparticles provide absorption in the visible region and facilitate electron excitation via local electrical field that is formed. The surface plasmons in silver have the ability to enhance this electrical field [95]. Besides, according to Chao et al., silver addition onto TiO<sub>2</sub> promotes the transformation of anatase to rutile that has higher specific surface area resulting in the enhancement in performance of photocatalyst, and also enhance electron-hole charge separation [96].

In the hydrothermal technique, titanium dioxide and metal precursors with a hydrolyzing agent are heated in an inert gas condition at high temperature. For example, Chen et al. prepared TiO<sub>2</sub> NPs decorated with Ag NPs by hydrothermal technique. Stability and dispersion of photocatalyst were achieved with polyamide network polymers. With silver addition, it was found that the mineralization rate of methyl orange was nearly 3 times higher than that of pure TiO<sub>2</sub>. The prepared photocatalyst has also photoactivity under visible light [97].

The other widely utilized techniques for metal doping are sol-gel and modified sol-gel methods to obtain nanomaterials that have better physicochemical properties with high homogeneity. In the sol-gel process, the inorganic network is added in a continuous liquid phase that is solvent. The process involves the hydrolysis and condensation of precursors which are metal alkoxides. With dilute acid or water, the precursor is hydrolyzed to form a solid called sol. In the end, calcination is taking place to obtain nanoparticles on the surface. Machado et al. reported the synthesis of silver-doped titanium dioxide via the sol-gel method by using Ti (IV) isopropoxide. The metal alkoxide was solubilized in isopropanol, and different amount of silver precursors were added to the mixture. In the end, drying and calcination processes were applied to obtain silver doped TiO<sub>2</sub> photocatalysts [98].

In the water in oil microemulsion technique, micellar aggregates consist of water droplets surrounded by the nonpolar solvent. The advantage of this technique is that particle size can be controlled via the nanodroplet size of microemulsions that are

formed. Ag/Cu-TiO<sub>2</sub> photocatalysts were prepared in water/sodium bis-(2-ethylhexyl) sulfosuccinate (AOT)/cyclohexene mixture by using microemulsion technique. The prepared particles are highly active in photocatalytic reactions under visible light during the decomposition of phenol and are highly effective in antimicrobial activities [99].

The photoreduction technique is another technique that can be utilized for the synthesis of metal-doped TiO<sub>2</sub>. Sobana et al. prepared silver-doped TiO<sub>2</sub> by photoreducing technique on the surface. For this, silver nitrate solution was added at constant pH value, and the mixture was irradiated via mercury lamps providing UV light irradiation for 3 hours to achieve a reduction of Ag<sup>+</sup> ions to Ag nanoparticles [94].

The photodeposition method involves the addition of silver nitrate solution to TiO<sub>2</sub> nanoparticle in aqueous medium and photodeposition in the photoreactor for silver nanoparticle doping on the surface [100].

#### **1.5.1.2. Gold Nanoparticles Doped TiO<sub>2</sub>**

Despite the more intense surface plasmon resonance (SPR) band of silver nanoparticles, gold (Au) nanoparticles absorb at longer wavelength region. This provides shifting of higher absorption at the visible light region. On the other hand, due to high stability, gold nanoparticles containing photocatalysts are resistant to oxidation reactions making them as promising candidates for heterogeneous catalysts [101].

Understanding the oxidation mechanism of such photocatalyst is crucial to construct novel photocatalytic materials. The photocatalytic activity can be enhanced by accumulation and discharging of electrons under UV light, and by providing electron transfer from metal nanoparticles to TiO<sub>2</sub> under visible light [102]. Several articles



demonstrate that surface plasmon of gold nanoparticles induces photocatalytic reactions under visible light [103,104]. In another study, the enhancement of photocatalytic activity with gold nanoparticles was also explained as the formation of dual Ti-Au catalytic sites at the interface of gold doped TiO<sub>2</sub>. It was demonstrated that these catalytic sites work together to activate molecular oxygen during the oxidation of carbon monoxide [105].

For Au nanoparticle loading onto the surface of TiO<sub>2</sub>, generally, the photo-deposition technique is applied. In the study, firstly, colloidal gold nanoparticles were prepared and TiO<sub>2</sub> powder was suspended into the aqueous solution of gold nanoparticles. Later on, photo-irradiation of the mixture was taking place with a light source having a higher wavelength than 300 nm by high-pressure mercury arc. Since Au nanoparticles on the surface acted as reduction centers, the effective photocatalytic performance was found for prepared catalysts. However, the disadvantage of this technique is that it is difficult to demonstrate the relation of nanoparticle size and amount of loading with the activity of photocatalysts. Besides, it is elusive to explain how TiO<sub>2</sub> types affect the performance of plasmonic photocatalysts because the activity depends on both the preparation technique and interaction between loaded nanoparticles and TiO<sub>2</sub> [106].

Prevention of agglomeration and leaching of gold nanoparticles in aqueous medium are crucial concerns to increase activity and to enhance the stability of photocatalysts during degradation of organics. Besides, if the interaction between metal nanoparticles and support is low, due to Ostwald ripening, during photocatalytic reaction larger particles can form resulting in the decrease of catalytic activity. Therefore, it is important to stabilize gold nanoparticles and to provide interaction between gold particles and support. It is clear that facile methods to prevent agglomeration and to achieve interaction of gold nanoparticles with TiO<sub>2</sub> are required to obtain highly effective Au doped TiO<sub>2</sub> photocatalysts.

### 1.5.1.3. Bimetallic Nanoparticles Doping

Further enhancement in the photocatalytic activity can be attainable with bimetallic (BM) composite nanoparticles that consist of two distinct metal elements [107]. The use of such nanostructures offers better electronic, optical and photocatalytic properties compared to their monometallic counterparts. Bimetalization not only provides the occurrence of new properties due to synergistic effect but also combines the properties of each individual metals [108].

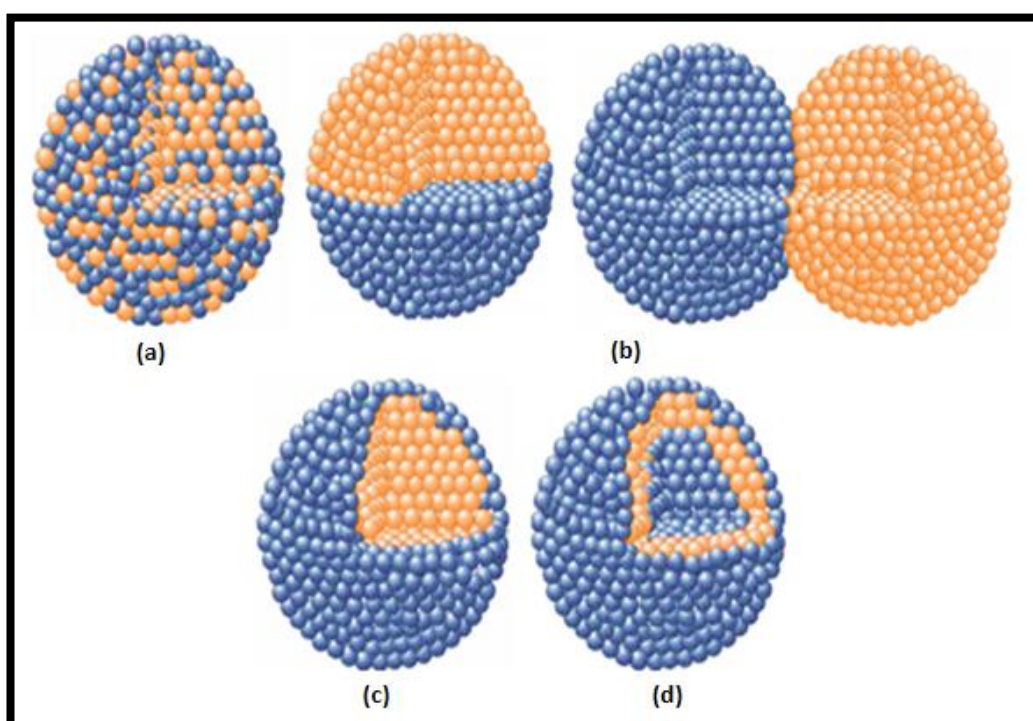


Figure 1.5. Schematic illustration of bimetallic nanoparticles [108].

Bimetallic nanoparticles with same size, shape and composition exhibit superior enhancement in the activity. Figure 1.5 exhibits a schematic illustration of bimetallic nanoparticles with different structures. The distribution mode of two elements can be oriented as (a) an alloy or an intermetallic structure, (b) a heterostructure, (c) a core-

shell, and (d) a multishell structure. The experimental parameters such as miscibility and reduction kinetics of metal ions strongly affect the structure of bimetallic nanoparticles. For example, lattice constants are reported as 0.408 and 0.409 for silver and gold, respectively. As these values are identical to each other, they are completely miscible, and therefore homogenous composition for the formation of Ag-Au bimetallic nanoparticles is considered [109].

In literature, it has been mentioned that there are mainly two factors for the higher photocatalytic performance of bimetallic nanoparticle containing photocatalyst. The electronic and geometric factors provide a better photocatalytic activity to bimetallic nanomaterials compared to monometallic counterparts [110]. The electronic effect is described as a change in the electronic structure of material when the bimetallic nanoparticle is formed. For example, when transition metals are used as bimetallic nanoparticles, the binding strength of nanoparticles to adsorbate molecules is strongly influenced by the interaction through the d-band of metal nanoparticles to adsorbates. Therefore, relative to Fermi level low lying d-band decreases the binding of bimetallic nanoparticles to adsorbates because of the occupation of antibonding states. On the other hand, the catalytic performance is also affected by the geometric effect. This effect is related to the shape of bimetallic nanoparticles that determine the arrangement of atoms on the surface of photocatalyst. Depending on the composition of nanoparticles, the binding strength between the surface of photocatalyst and adsorbate molecules can be changed with the enhanced reaction kinetics [111].

The promoting effect of bimetallic nanoparticles is strongly related to the synergy between each metal, therefore the electrical, optical and catalytic activity of photocatalyst enhance. This enhancement is due to the improved charge separation in photocatalyst that facilitates the transfer of electron-hole pairs from metal nanoparticles to conduction band of semiconducting material.

### 1.5.2. Conducting Polymers

Conducting polymers are organic molecules that have alternating double and single bonds along their backbone chain that result in conjugation system of  $\pi$  molecular orbitals due to overlap of  $p_z$  atomic orbitals. Conducting polymers behave as electron donors by transferring photogenerated electrons to the conduction band of semiconducting material [112].

Furthermore, conducting polymers has the advantage of easy processability in the solution process. Due to this advantage, after the discovery of polyacetylene in 1978, conducting polymers have gained great importance in several applications such as solar cells, transistor, electrochromic devices, supercapacitors, and light emitting diodes, etc. The photocatalysts can be prepared by doping of conducting polymers with semiconductors [113]. By this, the excellent electronic properties of semiconducting materials such as high conductivity and stability combined with the promising properties of conducting polymers such as accessibility, chemical versatility and tunable properties [114].

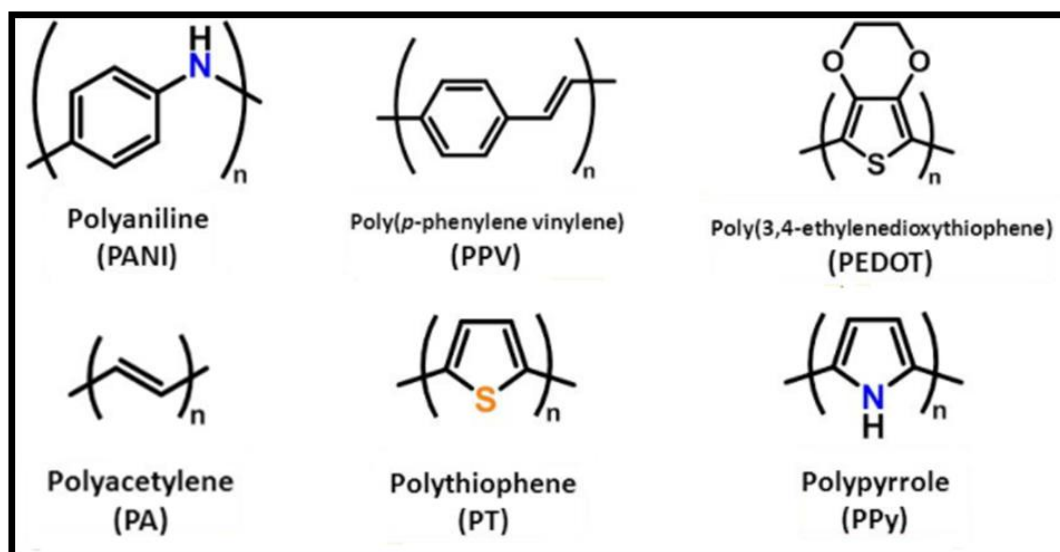


Figure 1.6. Chemical structures of some conducting polymers (CPs)

Figure 1.6 exhibits the chemical structures of conducting polymers that can be used as photocatalyst. Several conducting polymers such as polyaniline (PANI), polypyrrole (PPy), polyacetylene (PA), Poly (p-phenylene vinylene) (PPV), polythiophene (PT), poly (3,4-ethylenedioxythiophene) (PEDOT) can be utilized with semiconductors. Since band structures of conducting polymers are well-matched with the energy levels of most of the semiconducting materials, the recombination rate of charge carriers decreases with the enhancement of the photocatalytic activity of the material. Furthermore, conducting polymers can sensitize semiconductors to enhance light harvesting efficiency. These mentioned merits are important for the materials to be utilized in photocatalytic applications.

Although the semiconducting photocatalysts are generally used in the form of powder that provides high surface area in the solution of catalytic reaction, they have also several disadvantages such as having time-consuming procedures required while removing catalyst from reaction medium that results in the loss of some amount of photocatalyst, powder of photocatalysts are unhealthy to humans, and finally agglomeration of photocatalyst causes decrease in the surface area reducing

photocatalytic performance. These problems can only be solved via embedding semiconducting material into polymeric support. To select ideal polymeric support, some qualities should be considered such as the good adhesive property of polymer with catalyst, large specific area, high adsorption ability towards species in the reaction medium, high chemical, and mechanical stability. The techniques in order to immobilize semiconducting materials to the polymeric matrix can be mentioned as electrospinning, sol-gel methods, hydrothermal and solvothermal methods, chemical polymerization and impregnation. Mostly, in order to decrease the probability of damaging the polymeric matrix, these techniques should be applied at low temperatures [115].

#### **1.5.2.1. PEDOT**

Poly (3,4-ethylenedioxythiophene), usually known as PEDOT, has attracted significant interest as a conducting polymer due to its high thermal and chemical stability, robust, tunable in properties, high activity under visible light irradiation, high conductivity, high transparency, and biocompatibility. These advantages make PEDOT as the most promising conducting polymer to be utilized in several applications such as solar cells, organic light emitting diodes, biosensors and so on [116].

PEDOT is characterized by its color that changes from dark blue in a neutral state to light blue color in the oxidized state, therefore it is one of the most promising candidates for being utilized as conducting polymer, especially in electrochromic devices.

PEDOT has low electronic band gap value between the range of 1.6-1.7 eV, explained as optically induced  $\pi$ - $\pi^*$  transitions that is shown at 610 nm as wavelength value. Generally, by changing the degree of  $\pi$ -overlap along the chain of polymer with steric interactions and addition of electron donor and acceptor substituents to the structure

that affect the electronic property of  $\pi$ -system in the polymer, the band gap value of conjugated polymer can be altered. The low oxidation potential and comparatively low band gap towards other conjugated polymers provide superior electrochemical and spectroscopic properties to PEDOT that other polymers do not have [117].

Depending on counter-ion dopant and ratio of  $\text{FeCl}_3$  oxidant to monomer through the chemical polymerization reaction, which is a widely used technique for preparation, the solubility of polymer changes. For example, when the ratio of oxidant to monomer is above two, due to crosslinking, the structure becomes very rigid, therefore PEDOT becomes partially insoluble in organic solvents. When this ratio increases more, the insoluble polymer is formed [117].

As mentioned before, generally chemical polymerization technique is utilized to synthesize PEDOT polymer that includes oxidative coupling of monomers. In this technique, chemical oxidants such as ferric chloride or ammonium persulfate are the chemical oxidants that are used. The first step of the route is the oxidation of monomer with oxidants and formation of the radical cation followed by dimerization of free radicals. The reaction rate can be increased by using protic acids and Lewis acids throughout the reaction of EDOT with corresponding dimers and trimers. In chemical polymerization, oxidizing agents are necessary for the preparation of the polymer. Furthermore, the morphology of polymer can be varied by controlling the experimental parameters such as the concentration of monomer to oxidizer ratio, temperature, pH value and time [118,119].

Alternatively, electrochemical and photo-polymerization techniques are proposed for obtaining conducting polymers. In electrochemical polymerization, any oxidant is not necessary that makes this route proper for the deposition of polymer onto the substrate to make a thin film. The technique is generally carried out in water and acetonitrile solutions. Morphology, conductivity and electrical, mechanical and optical properties of polymers strongly depend on several parameters such as electrolyte, deposition time

and applied voltage. However, the disadvantages of this polymerization process are the difficulty in the electropolymerization of some monomers and the higher oxidation potential results in the oxidation of polymer excessively. In the photo-polymerization technique, monomers are polymerized by light sources such as ultraviolet (UV), visible light, and laser-generating radicals or holes. This technique is an alternative route to overcome the oxidation problems of electrochemical process. The process can be controlled via lighting on/off the source but the method needs further exploration to obtain polymers with better properties [119].

## **1.6. Magnetic Separation**

Until now, the addition of magnetic nanoparticles to distinct materials have gained great importance for such materials to be utilized in a wide range of application such as biomedicine, drug delivery, environmental remediation and photocatalytic technology [120].

Recently, researchers are interested in the novel photocatalyst preparation techniques to insert magnetic property into the structure of the catalyst. Addition of magnetic property to the material is important to provide reusability and easy separation of materials that are crucial concerns to achieve large scale utilization of these materials and to meet the future needs of semiconductor photocatalysis technology. Magnetic nanomaterials have advantages of chemical stability, low toxicity, easy synthesis procedures, and superior recycling property. Several synthetic procedures can be utilized for the synthesis of magnetic nanoparticles such as co-precipitation, microemulsion, thermally decomposition, solvothermal and hydrothermal synthesis [120]. By using these techniques, shape-controlled, stable, narrow size distributed nanoparticles with homogenous composition can be prepared.



Of these mentioned techniques, especially co-precipitation the most common and simplest method for the synthesis of magnetic nanoparticles with the addition salt precursors in alkaline solution at room temperature or elevated temperatures. The ratio of salt precursors, pH and reaction temperature are the fundamental parameters that affect the property of particles. By co-precipitation technique, a large scale of nanoparticles can be prepared, but this technique has some disadvantages such as hard control of particle size and shape and low dispersity.

Microemulsion technique is presented to prepare magnetic nanoparticles with narrow sizes. A microemulsion is a thermodynamically stable isotropic dispersion of two immiscible liquids that contain nano-domains stabilized by surfactant molecules. As the particles are synthesized within the nano-sized droplets, the particle nucleation, growth, and agglomeration are limited by the water to surfactant molar ratio [121].

Thermally decomposition technique provides monodispersed, well-shaped magnetic nanoparticles with superior magnetic properties. The technique includes firstly, decomposition of metal carbonyl precursors followed by oxidation with air or oxidant in an organic solvent at high temperatures, and secondly, decomposition of precursors with cationic metal centers. This method is mentioned as the best technique for controlling the size and morphology of prepared magnetic nanoparticles. In this method, reaction time and temperature, the amounts of organometallic compounds and surfactant and also type of solvent are important parameters that influence the properties of synthesized magnetic nanoparticles [122].

Despite the usage of a large amount of toxic and expensive chemicals in thermal decomposition technique, in solvothermal and hydrothermal processes such toxic chemicals are not required. The reaction conditions include high pressure and temperature that is carried out in reactors or autoclaves. These reactions are performed in ethanol or water solutions. Solvent temperature and time are important parameters while preparing magnetic nanoparticles through solvothermal and hydrothermal

processes. The techniques involve two routes that are hydrolysis and oxidation or neutralization of metal hydroxides. By these techniques, monodispersed, hydrophilic and single-crystalline magnetic nanoparticles can be produced [122,123].

However, the tendency of magnetic nanoparticles to agglomeration and high reactive character of these particles in harsh conditions can cause a reduction in the magnetic response of magnetic nanoparticles. To prevent this, coating of nanoparticles can be achieved via noble metal, carbon, zirconia, titanium, polymer and silica shells. Of the mentioned coatings materials, especially, silica coating has gained great attention due to the advantages it provides.

To prevent the reduction of magnetic nanoparticle core during photocatalytic reactions that result in the loss of magnetic property and to improve photocatalytic activity, introducing of silica shell seems to be crucial in order to isolate magnetic core and semiconducting material [124-126]. For silica coating, in literature, mainly four routes are proposed such as Stöber method, microemulsion, aerosol pyrolysis and methods related to silicate solution. However, the most common and widely utilized technique is Stöber method for silica coating onto magnetic nanoparticles. The Stöber method involves hydrolysis and condensation of alkoxysilanes such as tetraethylorthosilicate (TEOS) in ethanol-water solution with ammonia addition. By this technique, it is easy to control the thickness of the silica layer and to obtain uniform size with high crystallinity [127].

## 1.7. Scope of the Thesis

In this study, multifunctional composite materials as photocatalysts were produced to generate hydrogen from water-ethanol mixture and to remove organic dyes found in textile based wastewaters. For this, poly (3,4-ethylenedioxythiophene) (PEDOT) and noble metal nanoparticles (Ag, Au, AgAu NPs) modified TiO<sub>2</sub> based composite materials with magnetic property were prepared and characterized by using TEM, FE-SEM, ICP-OES, BET, particle size distribution (Zeta sizer), vibrating sample magnetometer (VSM). Then comparative photocatalytic activities and reuse capacities were investigated in the degradation of organic dye, methylene blue (MB), known as a typical pollutant in the textile industry under UV and solar radiation at room temperature. The degradation of MB was proved with UV-Vis and liquid chromatography-mass spectrometry (LC-MS) measurements. After that, hydrogen production capacities of each catalyst prepared from ethanol-water mixture were investigated under UV light. The amount of hydrogen produced at the end of photocatalytic process was measured with gas chromatography coupled with thermal conductivity detector (GC-TCD).



## CHAPTER 2

### EXPERIMENTAL

#### 2.1. Chemicals and Reagents

In this study, all the chemicals and reagents were analytical grade and utilized without further purification. In all experiments, deionized water obtained from milli-Q water purification system was used.

##### 2.1.1. Preparation of Cobalt Ferrite and Silica Coating on Cobalt Ferrite Magnetic Nanoparticles

For the preparation of cobalt ferrite magnetic nanoparticles, iron (III) chloride hexahydrate ( $\text{FeCl}_3 \cdot 6\text{H}_2\text{O}$ , Riedel-de Haën), cobalt (II) chloride hexahydrate ( $\text{CoCl}_2 \cdot 6\text{H}_2\text{O}$ , Surechem), sodium hydroxide (Sigma-Aldrich), sodium chloride ( $\text{NaCl}$ , Fisher Scientific Company) were purchased.

For silica coating on cobalt ferrite magnetic nanoparticles, tetraethyl orthosilicate (TEOS, Aldrich), (3-aminopropyl) trimethoxysilane (APTMS, Aldrich), ethanol (Merck) were purchased.

##### 2.1.2. Preparation of Conducting Poly (3,4-ethylenedioxythiophene) (PEDOT), Magnetically Recyclable MNP-PEDOT and MNP-PEDOT-TiO<sub>2</sub>

In the synthesis of conducting polymer (PEDOT), 3,4-ethylenedioxythiophene (EDOT, Sigma-Aldrich), iron (III) chloride anhydrous ( $\text{FeCl}_3$ , Sigma-Aldrich), chloroform ( $\text{CHCl}_3$ ), nitromethane ( $\text{CH}_3\text{NO}_2$ , Merck) were utilized.

For the addition of magnetic nanoparticles to PEDOT, silica coated cobalt ferrite magnetic nanoparticles ( $\text{CoFe}_2\text{O}_4@\text{SiO}_2$  MNPs) were prepared in the laboratory and used. Titanium dioxide nanopowder, P25 ( $\text{TiO}_2$ , Degussa-Evonik) was utilized.

### **2.1.3. Addition of Metal Nanoparticles onto the Surface of Materials**

For the addition of silver and gold monometallic, and silver-gold bimetallic nanoparticles onto the surface, silver nitrate ( $\text{AgNO}_3$ , Merck) and gold (III) chloride trihydrate ( $\text{HAuCl}_4$ , Sigma-Aldrich) metal salts and for chemical reduction, sodium borohydride ( $\text{NaBH}_4$ , Merck) was utilized.

## **2.2. Instrumentation**

### **2.2.1. Field Emission Scanning Electron Microscope (FE-SEM)**

Structural and morphological properties of prepared nanoparticles and photocatalysts were carried out with Quanta 400F Field Emission Scanning Electron Microscope (FE-SEM) located at Central Laboratory in METU. The photocatalysts were dropped onto the carbon tape coated copper grids and then they left for drying at room temperature overnight.

### **2.2.2. Transmission Electron Microscopy (TEM)**

Structural and morphological properties of prepared nanoparticles (monometallic and bimetallic) and photocatalysts were investigated with two different instruments, for high resolution with 2100 F, 200 kV TEM and for polymer containing materials with FEI 120 kV CTEM.

### **2.2.3. Energy Dispersive X-ray Spectrometer (EDX)**

The elemental compositions of prepared nanoparticles and photocatalysts were investigated with energy dispersive X-Ray coupled with SEM and TEM at METU Central Laboratory.

### **2.2.4. Vibrating Sample Magnetometer (VSM)**

The saturation magnetization of magnetic nanoparticles and magnetically recyclable photocatalysts were carried out with the instrument of Cryogenic Limited (United Kingdom), physical properties measurement system (PPMS) at METU Central Lab. The maximum magnetic field of VSM is 5.0 Tesla with magnet type NbTi multi-filamentary strands.

### **2.2.5. Inductively Coupled Plasma Optical Emission Spectrometer (ICP-OES)**

The amount of doped monometallic (Ag and Au) NPs and bimetallic (AgAu) NPs that were attached onto the surface of photocatalysts were determined by Perkin Elmer Optima 4300DV ICP-OES containing Echelle polychromator and S-CCD detector at METU Central Laboratory.

### **2.2.6. Atlas Solar Simulator**

To evaluate photocatalytic activities of prepared photocatalysts, atlas solar simulator equipped with xenon arc lamp with 150 W power was utilized.

### **2.2.7. Surface Area Analysis by using Brunauer–Emmett–Teller (BET)**

Surface area of prepared photocatalysts were investigated with BET method by the instrument of Quantachrome Corporation, Autosorb-6 that has the ability to measure the minimum surface area as  $0.05 \text{ m}^2/\text{g}$  and pore diameter between the range of 5-500 Angstrom.

### **2.2.8. Gas Chromatography (GC) Measurements**

Hydrogen recovery experiments were done by using GC Agilent 7890B coupled with FID and TCD detector in Atilim University.

### **2.2.9. UV-Vis Spectrophotometer**

Absorbance values of methylene blue dye solution were measured via UV-Vis spectrophotometer SPECORD S 600 in quartz cuvettes.

## **2.3. Preparation of Cobalt Ferrite ( $\text{CoFe}_2\text{O}_4$ ) Magnetic Nanoparticles with Surface Modification**

### **2.3.1. Preparation of Cobalt Ferrite ( $\text{CoFe}_2\text{O}_4$ ) Magnetic Nanoparticles**

$\text{CoFe}_2\text{O}_4$  magnetic nanoparticles were prepared via co-precipitation method. For the preparation of magnetic nanoparticles, 1.08 g of  $\text{FeCl}_3 \cdot 6\text{H}_2\text{O}$  and 0.476 g of  $\text{CoCl}_2 \cdot 6\text{H}_2\text{O}$  precursor salts were dissolved in 20 mL deionized water. During continuous mixing on a magnetic stirrer, 2.40 g of sodium hydroxide (in 20 mL water) and 0.88 g of sodium chloride (in 20 mL water) was mixed dropwise with precursor salts containing solution and stirring was continued for half an hour.



Later on, the container was taken and put into the ultrasonic bath and mixing was continued for 1 hour at 80 °C. At this temperature, the orange color of the solution turned to dark brown-black color showing the formation of magnetic nanoparticles. When the mixture cooled to room temperature, precipitates were isolated with a magnet, and after removal of the supernatant, prepared nanoparticles were washed with deionized water (Figure 2.1)

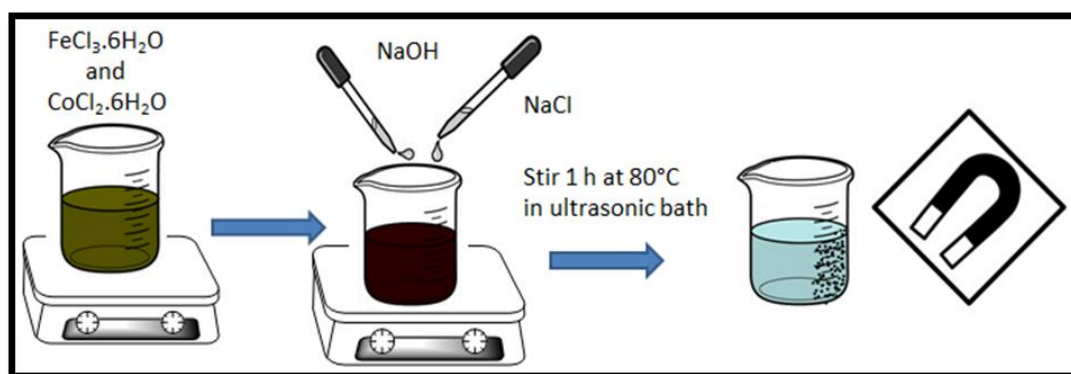


Figure 2.1. Illustration for the preparation of magnetic nanoparticles.

### 2.3.2. Silica Coating onto Cobalt Ferrite Magnetic Nanoparticles

Magnetic nanoparticles prepared by the co-precipitation method were coated with silica by applying Stöber method. For this, 338  $\mu\text{L}$  TEOS and 28.8  $\mu\text{L}$  APTMS were mixed in 160 mL ethanol with vigorous stirring. Later on, previously prepared magnetic nanoparticles dispersed in 40 mL deionized water were suspended into this solution and left for stirring for 3 hours at room temperature. Finally, prepared silica coated magnetic nanoparticles were rinsed several times with deionized water, isolated by the magnet and dried for further studies. Illustration for the preparation of silica coated cobalt ferrite magnetic nanoparticles was shown in Figure 2.2.

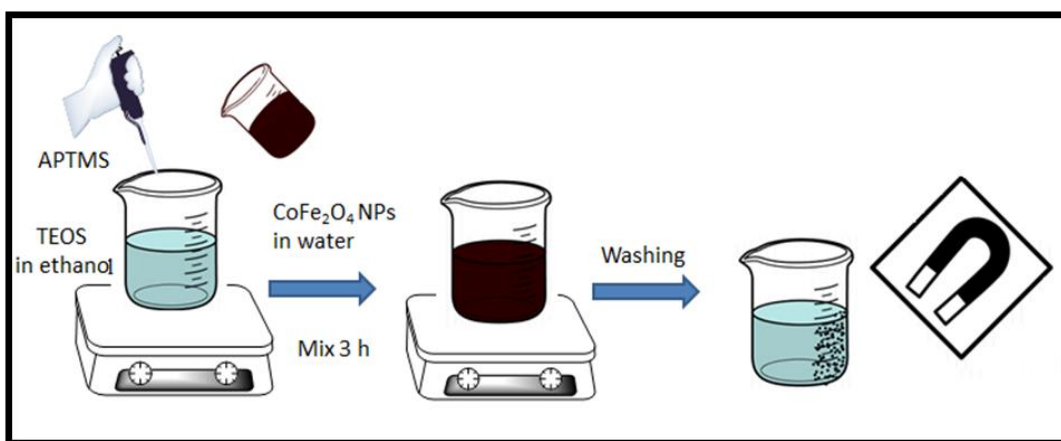


Figure 2.2. Illustration for the preparation of silica-coated magnetic nanoparticles.

## 2.4. Preparation of PEDOT, Magnetically Recyclable MNP-PEDOT and MNP-PEDOT-TiO<sub>2</sub>

### 2.4.1. Preparation of Conducting Polymer, PEDOT

Polymerization of monomer, EDOT, was carried out by using chemical polymerization technique by direct oxidation of monomer with anhydrous FeCl<sub>3</sub>. Schematic representation of the chemical polymerization of EDOT can be seen in Figure 2.3 with the structures of monomer and polymer.

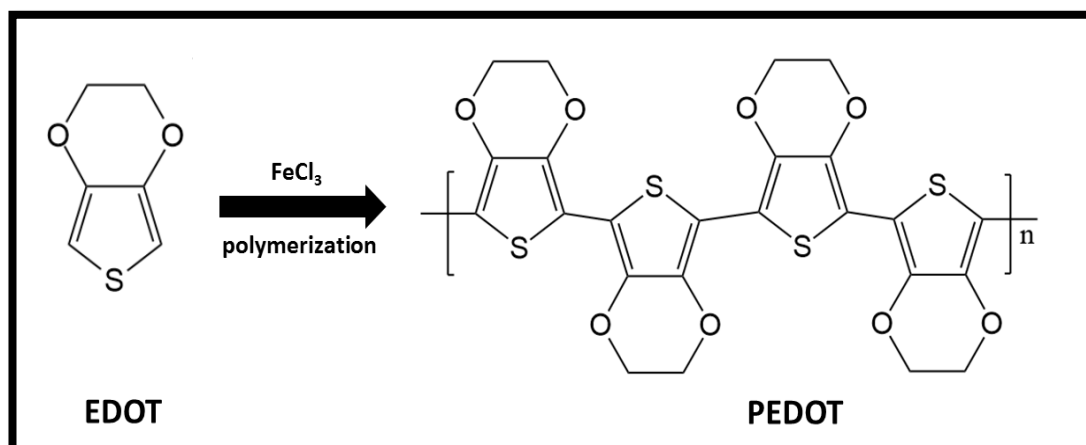


Figure 2.3. Schematic representation of chemical polymerization of EDOT by using  $\text{FeCl}_3$  initiator.

For polymerization, 107  $\mu\text{L}$  EDOT monomer was dissolved in 5 mL chloroform at  $0^\circ\text{C}$  in round bottom flask. In another flask, 0.65 g of  $\text{FeCl}_3$  and a small portion of nitromethane were dissolved in  $\text{CHCl}_3$  and then this mixture was added to the monomer-containing solution dropwise. The reaction mixture was left for stirring for 1 day. After then, 15 mL methanol was added to the mixture in order to obtain precipitates and the solution was refrigerated. After then, the polymer was filtered and washed by Soxhlet apparatus with the circulation of methanol for 2 days to remove impurities. Illustration for preparation of PEDOT was shown in Figure 2.4.

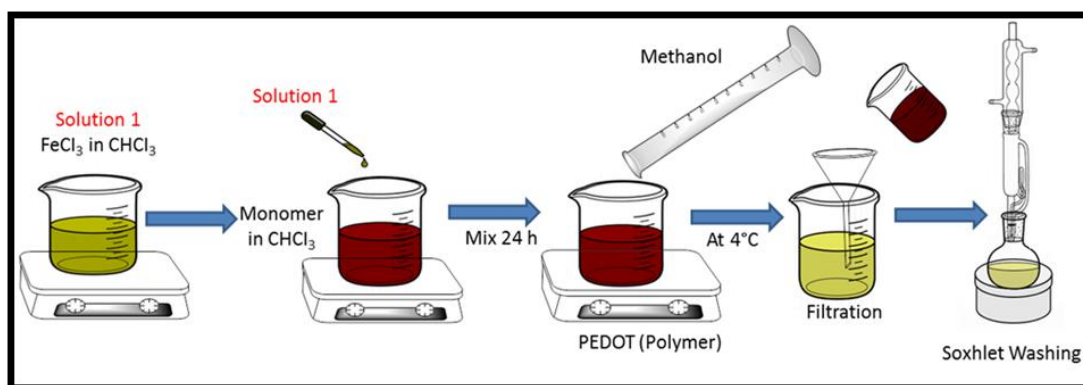


Figure 2.4. Illustration for the preparation of PEDOT polymer.

### 2.4.2. Preparation of Magnetically Recyclable, MNP-PEDOT Composite Material

107  $\mu\text{L}$  EDOT monomer was dissolved in chloroform at  $0^\circ\text{C}$  and to this monomer-containing solution, 0.1 g of magnetic nanoparticles were added. Later on, in another container, 0.65 g of  $\text{FeCl}_3$  and a small portion of nitromethane were dissolved in  $\text{CHCl}_3$  and then this mixture was added to the monomer and magnetic nanoparticle containing solution dropwise. The reaction mixture was left for stirring for 1 day. After then, 15 mL methanol was added to the mixture and the solution was refrigerated in order to provide precipitation of photocatalysts. After then, MNP-PEDOT photocatalysts were filtered and washed by Soxhlet apparatus with the circulation of methanol for 2 days. Preparation procedure was shown in Figure 2.5.

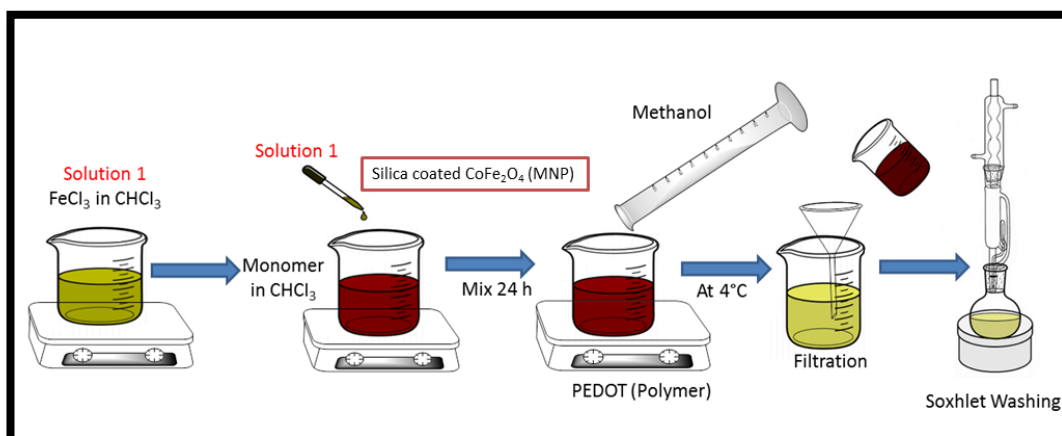


Figure 2.5. Illustration for the preparation of MNP-PEDOT composite material.

### 2.4.3. Preparation of Magnetically Recyclable, MNP-PEDOT-TiO<sub>2</sub> Composite Material

0.65 g of FeCl<sub>3</sub> and a small portion of nitromethane were dissolved in CHCl<sub>3</sub> and to this initiator-containing solution 0.040 g of TiO<sub>2</sub> nanoparticles were added (Mixture 1). Into another container, 107 μL EDOT monomer was dissolved in 5 mL chloroform at 0°C and to this monomer containing solution 0.1 g of magnetic nanoparticles were added (Mixture 2). Later on, Mixture 1 was added to Mixture 2 dropwise. The reaction mixture was left for stirring for 1 day. After then, 15 mL methanol was added to the mixture and the solution was refrigerated for precipitation of photocatalysts. After then, MNP-PEDOT-TiO<sub>2</sub> photocatalysts were filtered and washed by Soxhlet apparatus with the circulation of methanol for 2 days. Illustration for the synthetic procedure for MNP-PEDOT- TiO<sub>2</sub> can be seen in Figure 2.6.

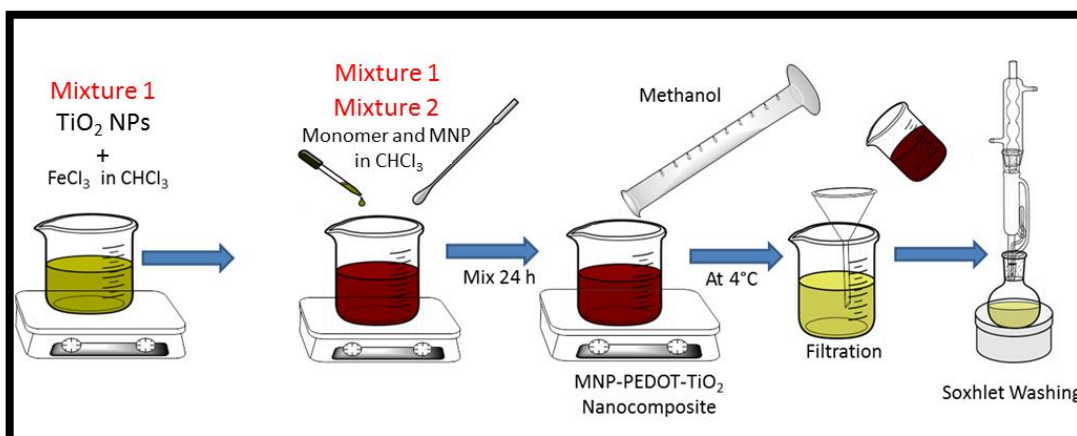


Figure 2.6. Illustration for the preparation of MNP-PEDOT-TiO<sub>2</sub> composite material.

## 2.5. Addition of Noble Metal Nanoparticles onto the Surface of Composite Materials

Silver and gold (monometallic) nanoparticles and AgAu (bimetallic) nanoparticles were attached to supports of TiO<sub>2</sub> and MNP-PEDOT-TiO<sub>2</sub> by liquid impregnation technique. For this, Ag<sup>+</sup> and Au<sup>3+</sup> ions were immobilized onto the supports by using AgNO<sub>3</sub> and HAuCl<sub>4</sub> metal salts, respectively. Depending on obtaining monometallic or bimetallic nanoparticles on the surface of substrates, metal salts were added either alone or together. Initially, 100 mg supports have taken and dispersed in 10 mL deionized water via magnetic stirrer. After then, 2% (w/w) AgNO<sub>3</sub> and 2% (w/w) HAuCl<sub>4</sub> were mixed with these dispersions and mixtures were left for vigorous stirring continuously for 5 hours.

Metal ions attached supports (TiO<sub>2</sub> and MNP-PEDOT-TiO<sub>2</sub>) were isolated from the medium by using a magnet to continue for the washing step. Unbound ions and impurities were eliminated via one time washing with deionized water. During washing steps, supernatants and washing water used for rinsing particles were collected to investigate the loading amount of ions onto the surface with ICP-OES instrument.

The loading step was followed by the reduction of ions by using  $\text{NaBH}_4$  as a reducing agent. For this, previously prepared ion loaded composite materials were dispersed in 10 mL of deionized water and 40 mg reducing agent was added to the mixture to reduce ions to nanoparticles. After mixing for 1 hour, the prepared particles were isolated and rinsed two times with deionized water. Later on, the particles were dried and they were utilized for further experiments. Illustration for the loading procedure of  $\text{Ag}^+$  and  $\text{Au}^{3+}$  ions onto the surface and chemical reduction of the ions via  $\text{NaBH}_4$  can be seen in Figure 2.7.

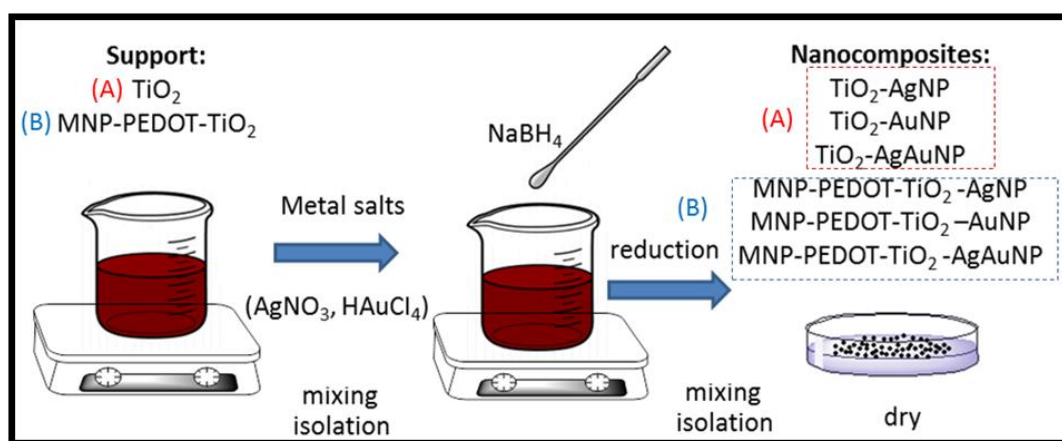


Figure 2.7. Illustration for the loading procedure of Ag and Au ions onto the surface and chemical reduction of the ions via  $\text{NaBH}_4$

## 2.6. Degradation of Methylene Blue Under Light Source

Before starting with photocatalytic studies, firstly adsorption-desorption equilibrium was investigated. Under dark, 10 mg of photocatalysts were added to 10 mL methylene blue (MB) solutions (nearly 8 mg/L), and the mixture was left in the dark for continuous stirring. Stirring was continued until the absorbance measurements become constant. After then, the degradation of MB solution with photocatalysts was started in a UV reactor (Figure 2.8).

After starting UV exposure, the decolorization of MB solution was followed in each 10 min intervals. The decrease in absorbance values was measured via UV-Vis spectrophotometer, by taking 2 mL sample from the reactor via syringe and clear MB solution was separated from the sample by centrifugation and external magnet. As specific absorbance maxima for MB was measured at 665 nm, this peak was checked in each time intervals. The percent degradation of MB dye solution was calculated by the equation given below (Eq. 1)

$$D = \left( \frac{A_0 - A_t}{A_0} \right) \times 100 \quad \text{Eq. 1.}$$

( $A_0$  = initial absorbance value of dye,  $t$  = reaction time,  $A_t$  = absorbance at time  $t$ )

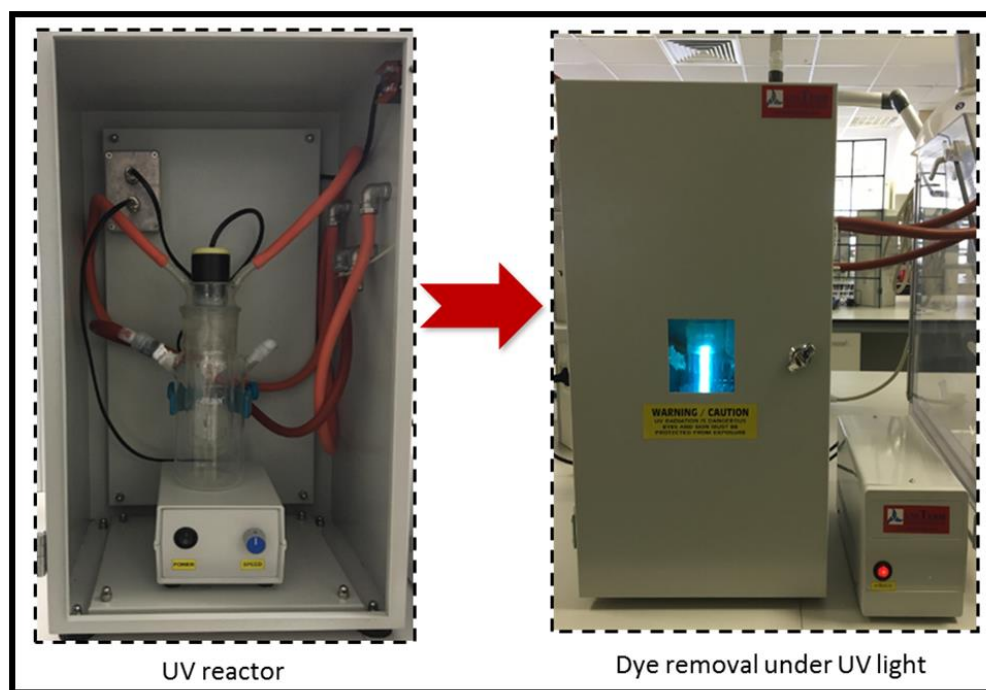


Figure 2.8. Photocatalytic reactor and UV system that were utilized throughout the photocatalytic efficiency tests.



The same photocatalysts were also used to determine photocatalytic performances via Atlas solar simulator by calculating with  $E_q$ . 1 in the same way (Figure 2.9).



*Figure 2.9.* Atlas solar simulator system that was utilized throughout the photocatalytic efficiency tests.

LC-MS system was used to determine the degradation products of MB at the end of the photocatalytic reactions.

## **2.7. Hydrogen Generation Experiments Under UV Light Irradiation**

Photocatalytic hydrogen generation tests of catalysts were carried out in the same reactor attached to a glass column containing deionized water with an average thickness of 2 cm as shown in Figure 2.10. For this, 20 mg photocatalysts were placed into the reactor and 50 mL of ethanol-water solution were added and resulting dispersion mixed continuously for few minutes before UV light exposure. Later on,

the reactor was exposed to light irradiation and the change in water level in the column was measured and recorded.

The amount of hydrogen in the gas mixture was investigated by taking a gas sample by Tedlar sample bag and injected into a GC instrument. As carrier gas during the measurements, N<sub>2</sub> gas was utilized, and the quantity of H<sub>2</sub> was examined against the peak area of the signal, which directly depends on the mole of gas evolved. Figure 2.10 exhibits the system utilized for photocatalytic hydrogen production and Tedlar bag used for the collection of gas sample for GC measurements.



Figure 2.10. (a) System that was used to generate hydrogen gas from the ethanol-water mixture under UV light (b) Tedlar bag for collecting a gas sample for GC analyses.

## CHAPTER 3

### RESULTS AND DISCUSSION

In this study, polymer and noble metal nanoparticles doped TiO<sub>2</sub> containing multifunctional photocatalysts were prepared to provide environmental remediation by the degradation of dye solutions finding in wastewaters. The prepared photocatalysts were also proper candidates for hydrogen generation from volatile organic compounds.

For this purpose, PEDOT, magnetically recyclable MNP-PEDOT, magnetically recyclable MNP-PEDOT-TiO<sub>2</sub>, MNP-PEDOT-TiO<sub>2</sub>-AgNP, MNP-PEDOT-TiO<sub>2</sub>AuNPs, MNP-PEDOT-TiO<sub>2</sub>-AgAuNPs composite materials with high photocatalytic activity and well-separation property were produced. The comparative photocatalytic activity of the prepared composites was investigated in the degradation of organic dye, methylene blue (MB), known as a typical pollutant in the textile industry under UV radiation at room temperature. Furthermore, the comparative photocatalytic activity of the prepared composites was investigated under solar radiation. Besides the results of photocatalytic reactions, the morphological and magnetic property of prepared photocatalysts were investigated. In the end, the degradation of MB dye was proven by LC-MS by examining degradation products after photocatalytic reactions and photo-stability of magnetic nanoparticle containing photocatalysts were investigated via recycling tests. In the last part of the study, the prepared catalysts were also utilized for H<sub>2</sub> generation from the ethanol-water mixture under UV light and the quantity of hydrogen evolved at the end of the reactions was determined by GC-TCD.

### 3.1. Preparation and Characterization of Composite Materials

#### 3.1.1. Preparation and Characterization of Silica-Coated Magnetic Nanoparticles

In order to provide magnetic separation, silica coated cobalt ferrite ( $\text{CoFe}_2\text{O}_4@\text{SiO}_2$ ) nanoparticles were added to the composite material. In the preparation of  $\text{CoFe}_2\text{O}_4@\text{SiO}_2$ , initially  $\text{CoFe}_2\text{O}_4$  nanoparticles were synthesized via co-precipitation technique. This technique provides small magnetic nanoparticles together with well-dispersed agglomerates. SEM image of magnetic nanoparticles can be seen in Figure 3.1.

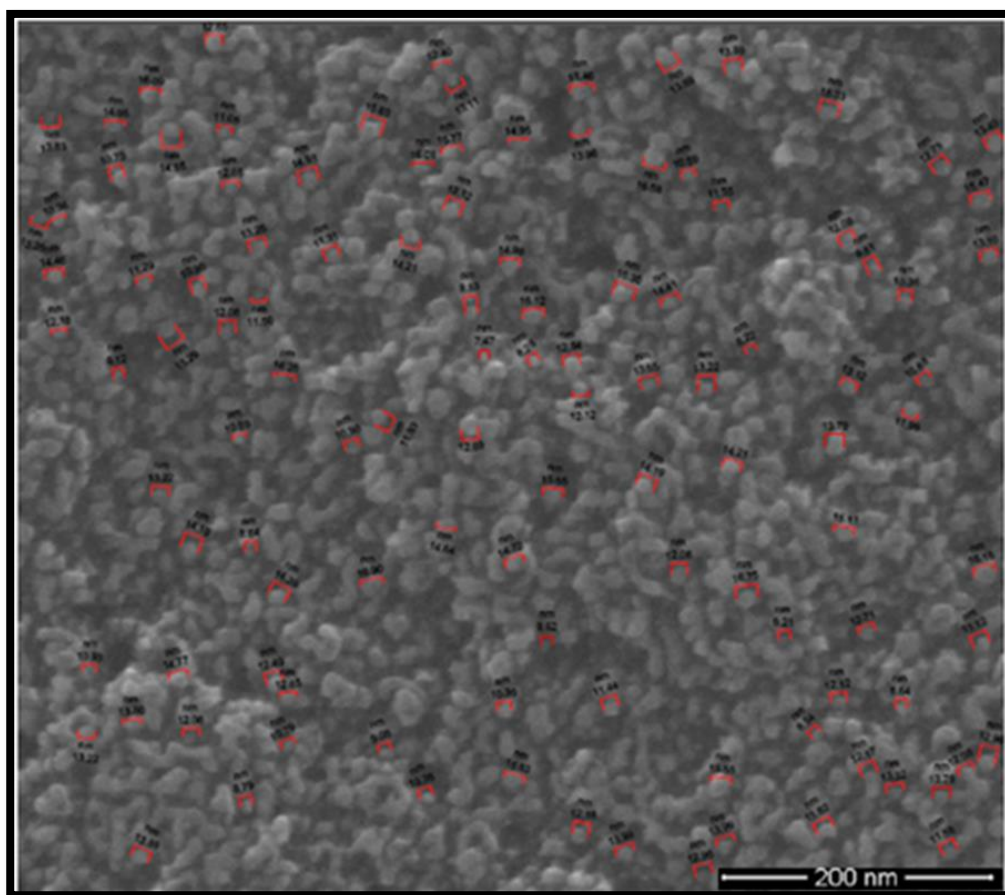


Figure 3.1. SEM image of  $\text{CoFe}_2\text{O}_4$  magnetic nanoparticles.

100 nanoparticles were selected from the Figure 3.1 and size of nanoparticles was determined as approximately  $13 \pm 2$  nm.

Elemental composition of prepared magnetic nanoparticles was investigated by EDX pattern shown in Figure 3.2.

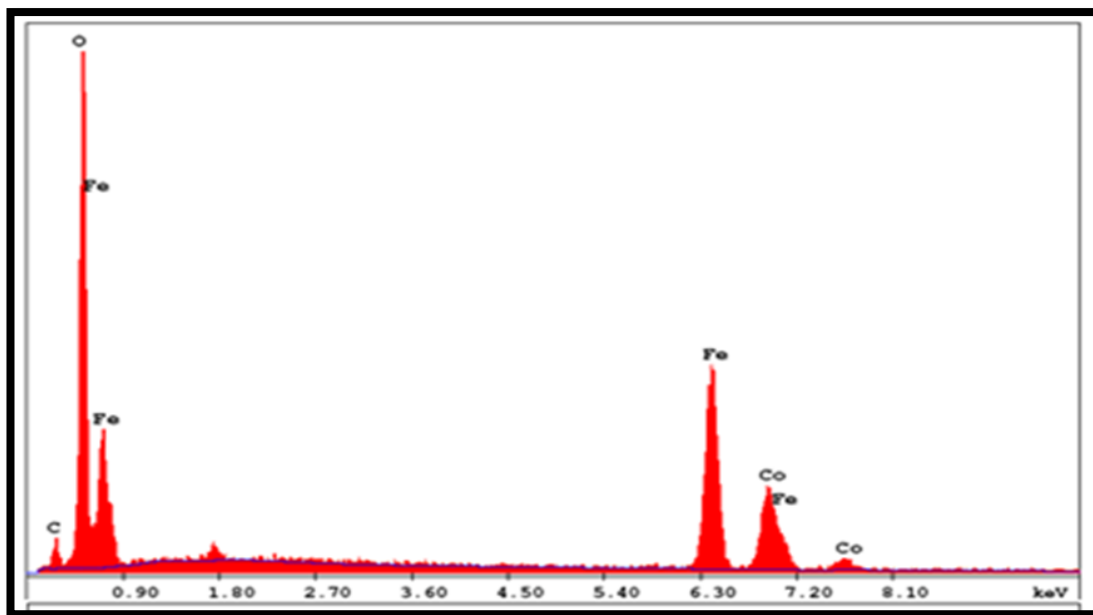


Figure 3.2. EDX pattern of  $\text{CoFe}_2\text{O}_4$  magnetic nanoparticles.

According to EDX results, the ratio of peaks is in good agreement with expected elemental composition of  $\text{CoFe}_2\text{O}_4$ .

After obtaining  $\text{CoFe}_2\text{O}_4$ , silica coating was utilized with Stöber method that involves hydrolysis and condensation of TEOS in ethanol-water sol. Then, the morphology and chemical composition of silica-coated magnetic nanoparticles were investigated by TEM and energy dispersive X-ray (EDX) analysis. Results are shown in Figure 3.3 and in Figure 3.4, respectively.

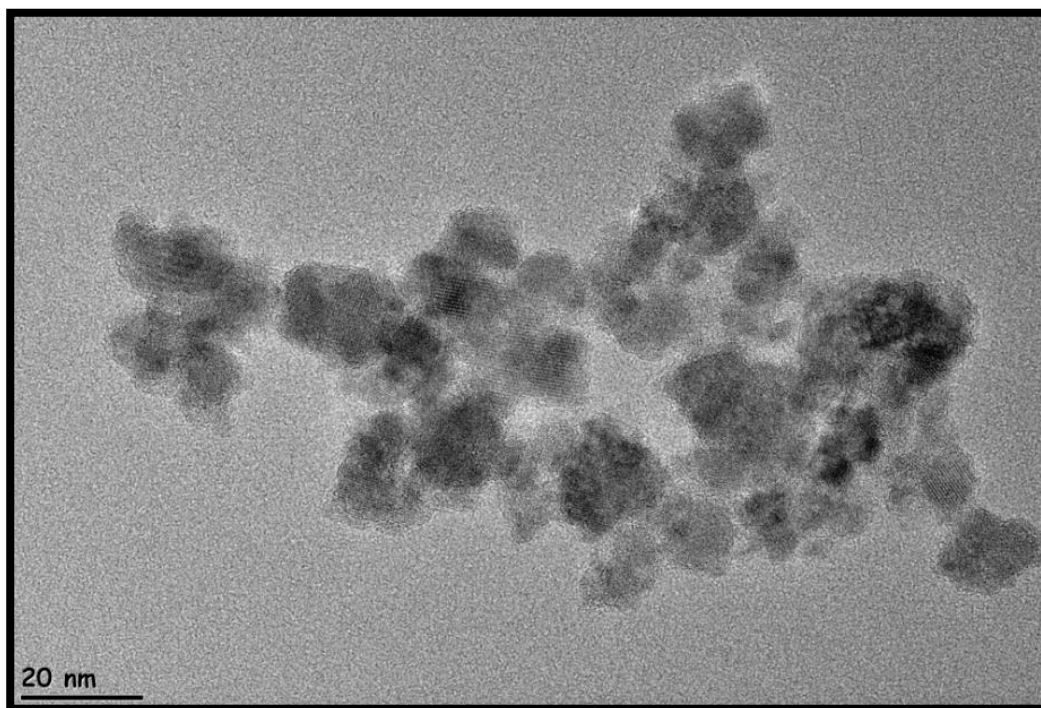


Figure 3.3. TEM image of  $\text{CoFe}_2\text{O}_4@\text{SiO}_2$  core-shell magnetic nanoparticles.

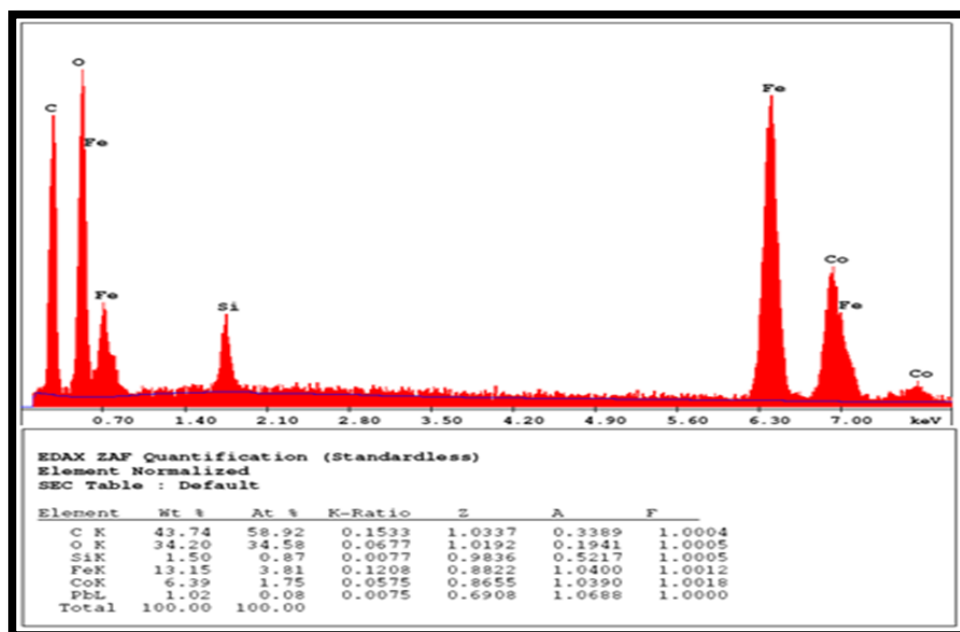


Figure 3.4. EDX pattern of  $\text{CoFe}_2\text{O}_4@\text{SiO}_2$  core-shell magnetic nanoparticles.



Accordingly, the particle size of silica coated  $\text{CoFe}_2\text{O}_4$  nanoparticles was calculated as  $18 \pm 3$  nm. When the initial size of  $\text{CoFe}_2\text{O}_4$  nanoparticles was taken as 13 nm on average, the thickness of the silica coating was calculated as  $5 \pm 3$  nm. EDX pattern in Figure 3.4 exhibits the formation of silica shell on the surface of magnetic nanoparticles.

The magnetic property of prepared silica-coated magnetic nanoparticles was investigated by vibrating sample magnetometer (VSM).

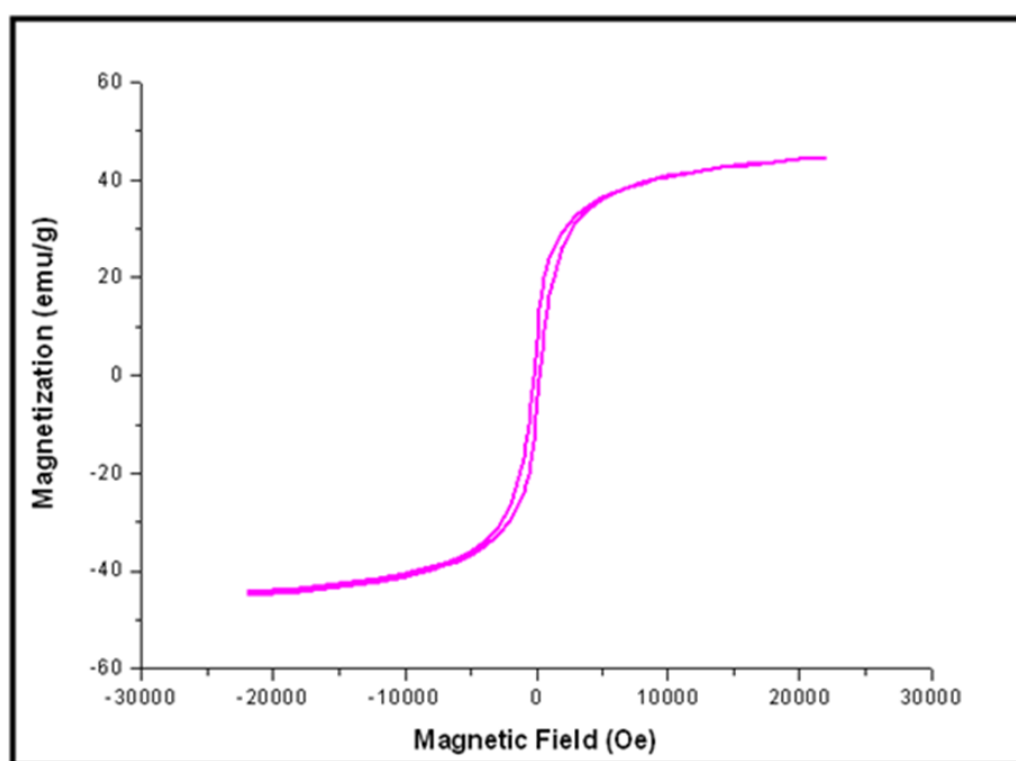


Figure 3.5. Magnetization vs. magnetic field for  $\text{CoFe}_2\text{O}_4@SiO_2$  core-shell magnetic nanoparticles.

Figure 3.5 exhibits a hysteresis loop of magnetic nanoparticles obtained at 300 K and with 2.2 Tesla magnetic fields. The saturation magnetization was obtained as 48.7 emu/g.

### **3.1.2. Preparation and Characterization of PEDOT Polymer and MNP-PEDOT Composite Material**

For the synthesis of PEDOT and magnetic nanoparticles containing PEDOT (MNP-PEDOT), the chemical oxidation polymerization technique was utilized as mentioned in the experimental part. The synthesis by chemical polymerization provides high PEDOT yield compared to other polymerization techniques such as electrochemical polymerization and vapor phase polymerization for large-scale applications.

The surface morphology of PEDOT polymer and MNP-PEDOT are shown in Figure 3.6 and Figure 3.7, respectively.



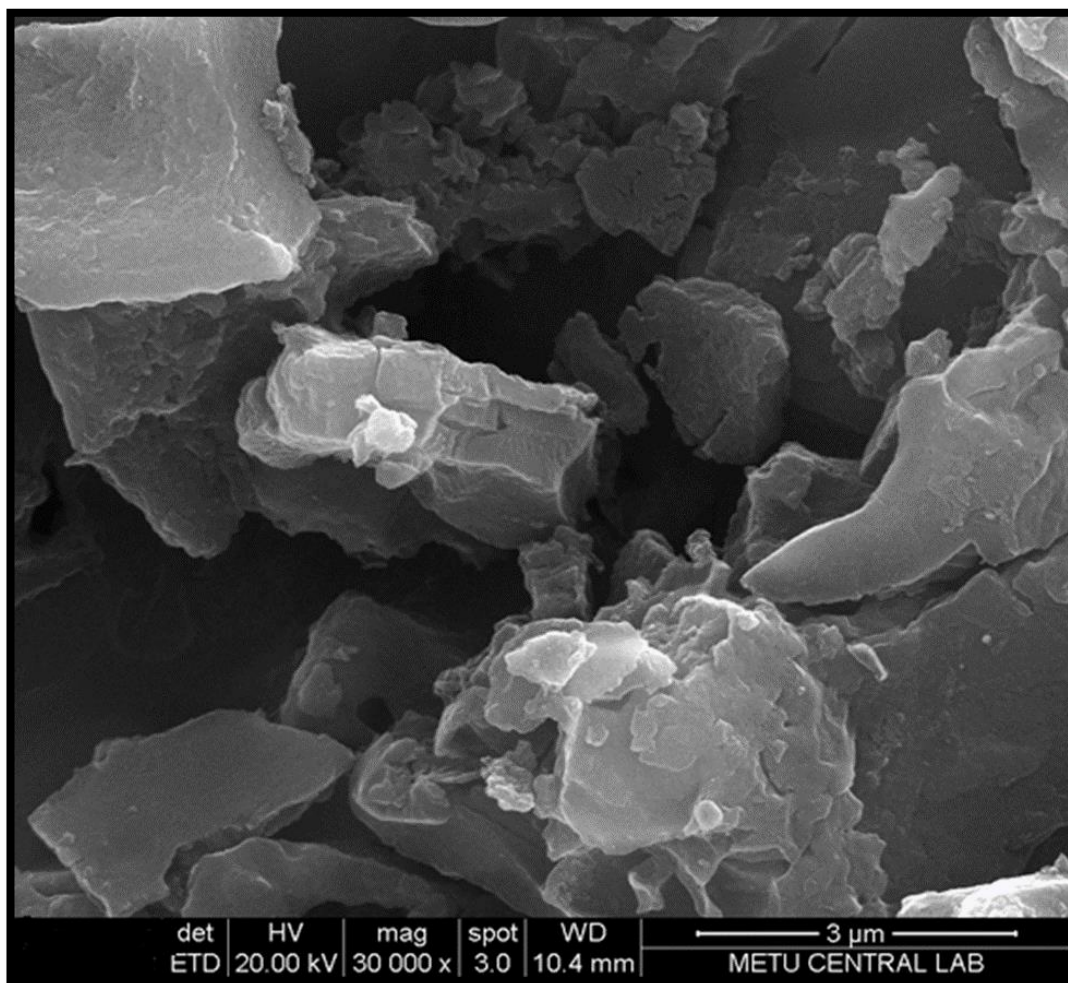


*Figure 3.6.* SEM image of PEDOT.

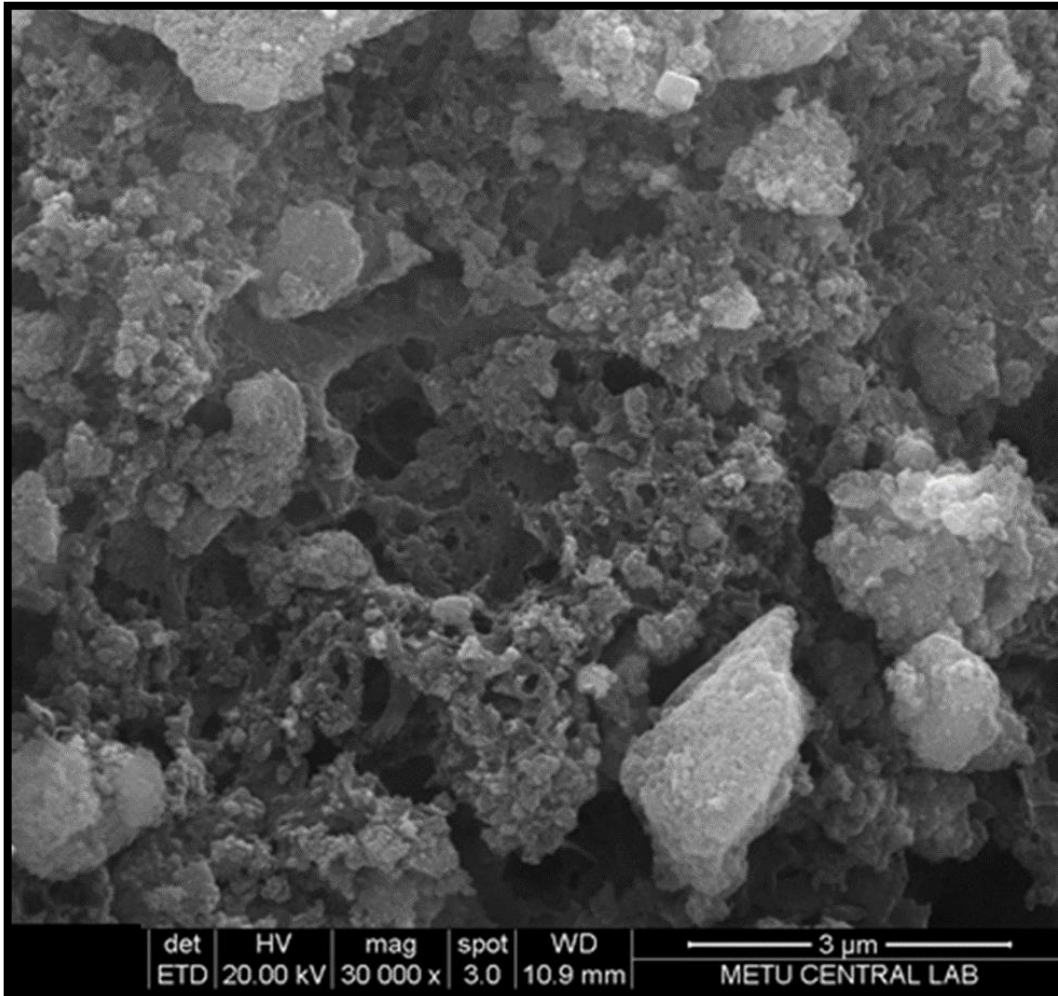


*Figure 3.7.* SEM image of MNP-PEDOT.

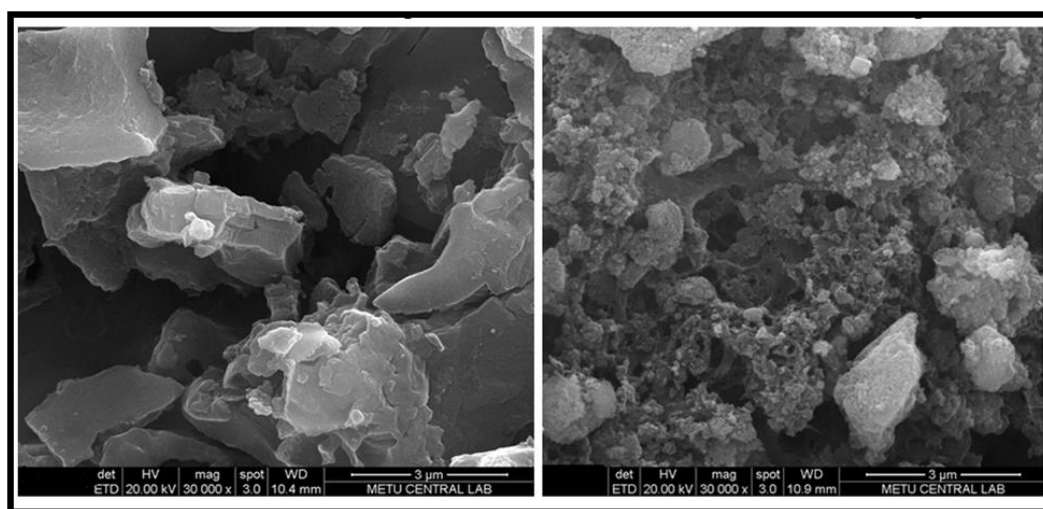


*Figure 3.8.* Comparison of SEM images of PEDOT polymer and MNP-PEDOT.

When the SEM images of PEDOT and MNP-PEDOT are compared (Figure 3.8), due to the addition of magnetic nanoparticles into the structure, MNP-PEDOT exhibits different structural morphology than PEDOT polymer. According to images, incorporation of small nanoparticles to polymer matrix results an increase in the porosity of structure, and surface area. This observation was also checked by the Brunauer–Emmett–Teller (BET) analysis. For this, the nitrogen adsorption/desorption experiments were carried out at 77 K using a Quantachrome Instrument. The sample was outgassed under vacuum at 573 K for 24 h before the adsorption of nitrogen. The surface area of samples was calculated from the BET plot. According to BET analysis, the surface area for PEDOT was measured as 8.3 m<sup>2</sup>/g, and for MNP-PEDOT as 34.3 m<sup>2</sup>/g. Therefore, BET analysis results exhibit the proof of an increase in surface area with the addition of magnetic nanoparticles to the polymer matrix.

### 3.1.3. Preparation and Characterization of MNP-PEDOT-TiO<sub>2</sub> Composite Material

Commercially available Degussa P25 TiO<sub>2</sub> nanoparticles were utilized throughout the study. Figure 3.9. exhibited a TEM image of TiO<sub>2</sub> nanoparticles used for the preparation of composites.

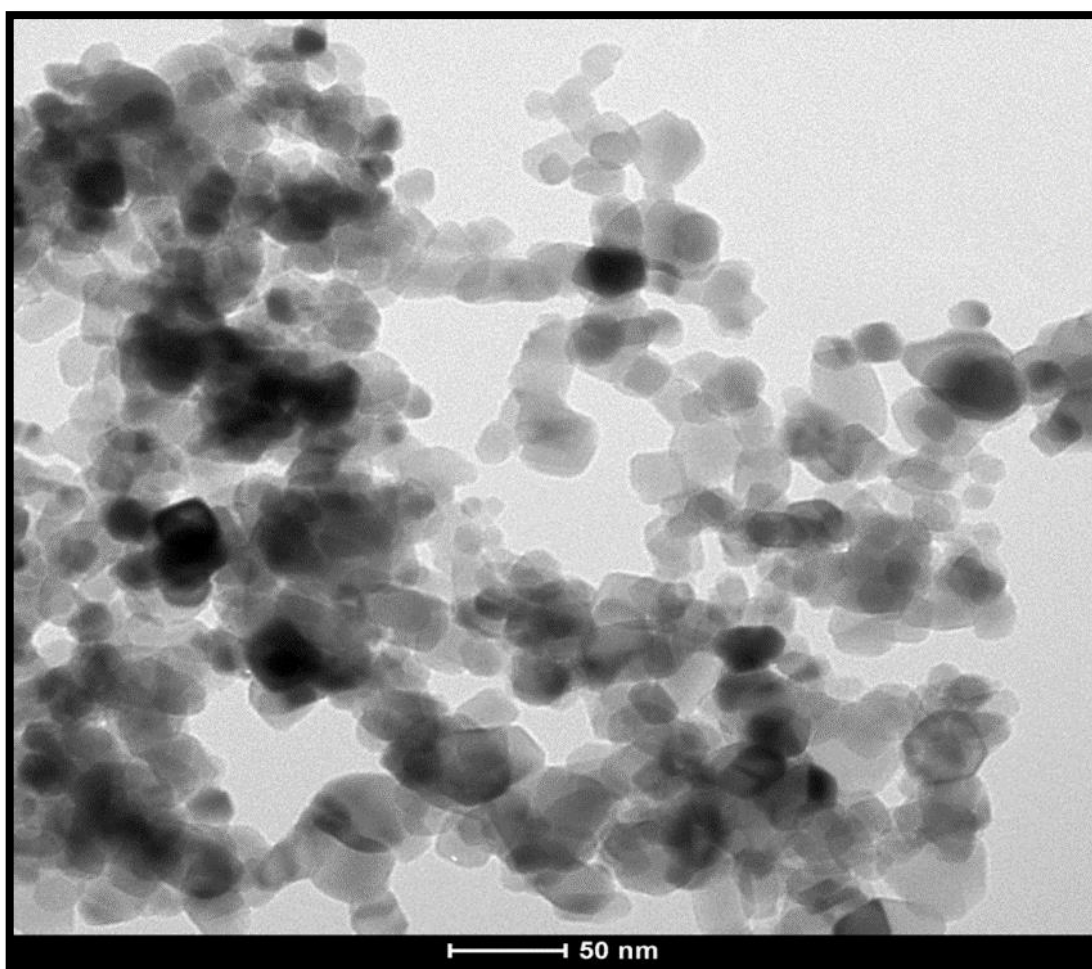


*Figure 3.9.* TEM image of TiO<sub>2</sub> nanoparticles.

According to TEM image, TiO<sub>2</sub> nanoparticles were quite homogenous and the grain size of particles was calculated in the range of 20-30 nm.

Secondly, the characterization of MNP-PEDOT-TiO<sub>2</sub> composite material was investigated. For surface morphology and chemical composition analysis, TEM and EDX pattern of prepared materials were obtained, respectively (Figure 3.10, Figure 3.11).

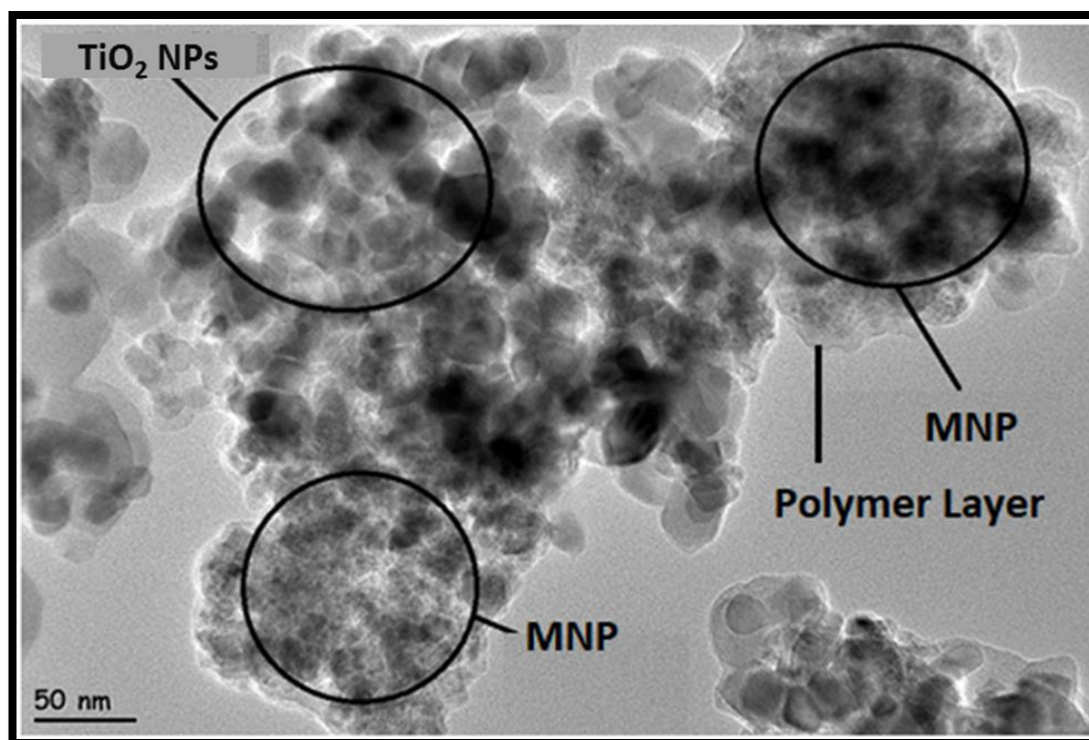


*Figure 3.10.* TEM image of MNP-PEDOT- TiO<sub>2</sub>.



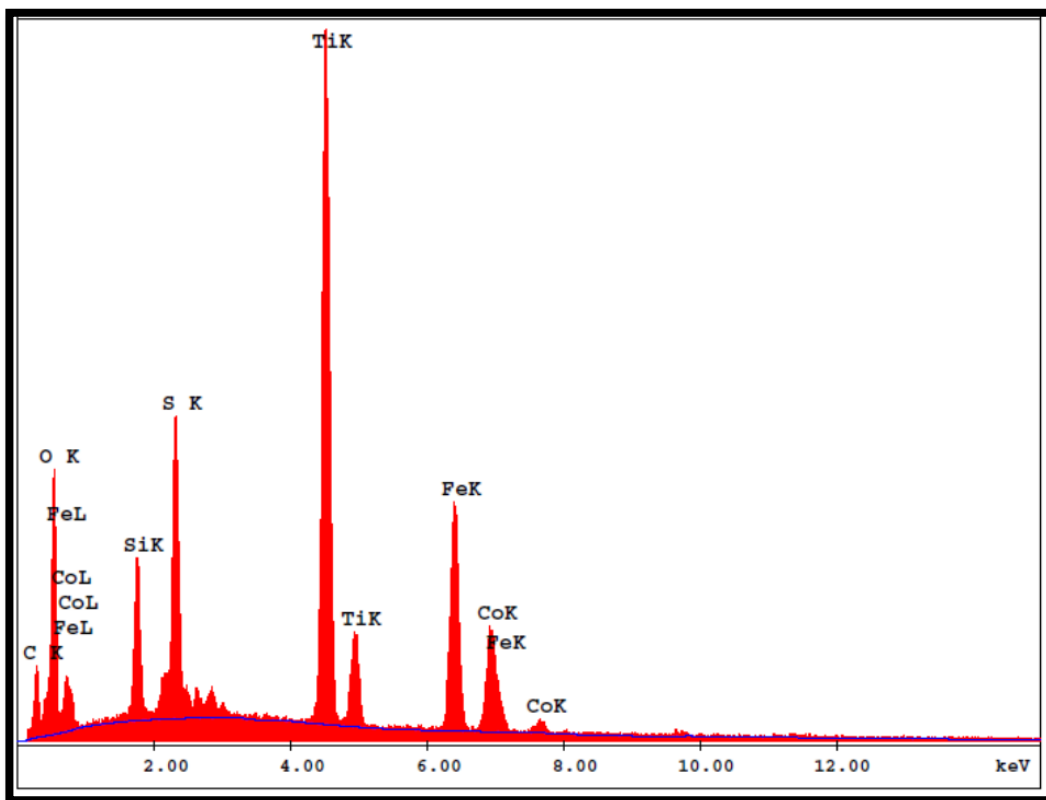


Figure 3.11. EDX pattern of MNP-PEDOT-TiO<sub>2</sub>.

According to the elemental composition of composite material, besides titanium peak, a sulfur signal corresponding to PEDOT, and also silica, cobalt, and iron peaks were observed corresponding to silica coated CoFe<sub>2</sub>O<sub>4</sub> magnetic nanoparticles. The specific surface area of the composite material was calculated from BET analysis as 42.5 m<sup>2</sup>/g. As mentioned before, according to BET results, surface area for PEDOT and MNP-PEDOT composite materials were calculated as 8.3 m<sup>2</sup>/g and 34.3 m<sup>2</sup>/g, respectively. With the addition of TiO<sub>2</sub> nanoparticles to MNP-PEDOT, surface area of composite material increased which was attributed to morphology change of prepared material.

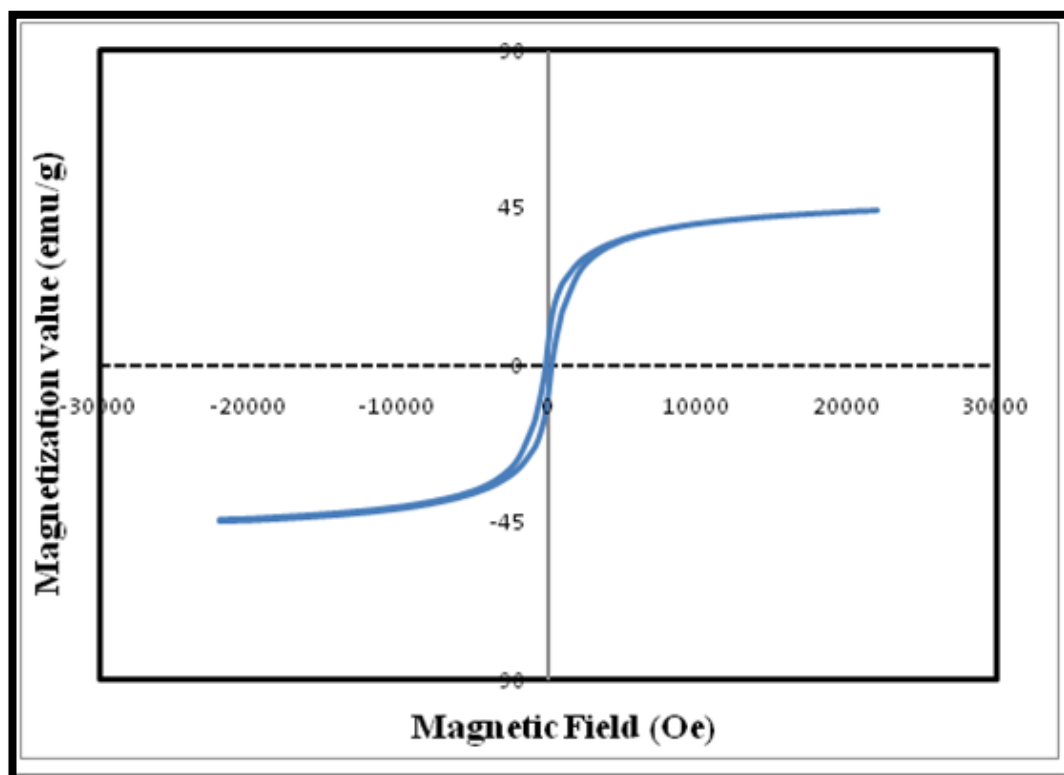


Figure 3.12. Magnetization vs. magnetic field for MNP-PEDOT-TiO<sub>2</sub>.

According to VSM curve of MNP-PEDOT-TiO<sub>2</sub>, saturation magnetization was found as 39.4 emu/g as seen in Figure 3.12. When saturation magnetization of the MNP-PEDOT-TiO<sub>2</sub> is compared with the magnetization value of CoFe<sub>2</sub>O<sub>4</sub>@SiO<sub>2</sub> magnetic nanoparticles (48.7 emu/g), the embedding of magnetic nanoparticles to the polymer matrix results in the small decline in the values. However, still, the prepared MNP-PEDOT-TiO<sub>2</sub> materials can be completely collected from the solution medium within 30 seconds. This shows that the material still has magnetic property so that it can be separated from the solution medium by using external magnet (Figure 3.13).



*Figure 3.13.* Magnetic behavior of MNP-PEDOT-TiO<sub>2</sub> composite material under externally applied magnetic field (1.6 T).

#### **3.1.4. Characterization of Silver and Gold Nanoparticle Added TiO<sub>2</sub> Nanoparticles**

As mentioned in the experimental part, addition of noble metal nanoparticles onto the surface of TiO<sub>2</sub> was achieved via a liquid impregnation technique. According to ICP-OES results, 1.15 % (w/w) silver added to TiO<sub>2</sub> nanoparticles substrate. Figure 3.14 and Figure 3.15 exhibited TEM image and EDX pattern of silver added TiO<sub>2</sub> nanoparticles. The average particle size of Ag nanoparticles on the surface was calculated as  $8 \pm 2$  nm.



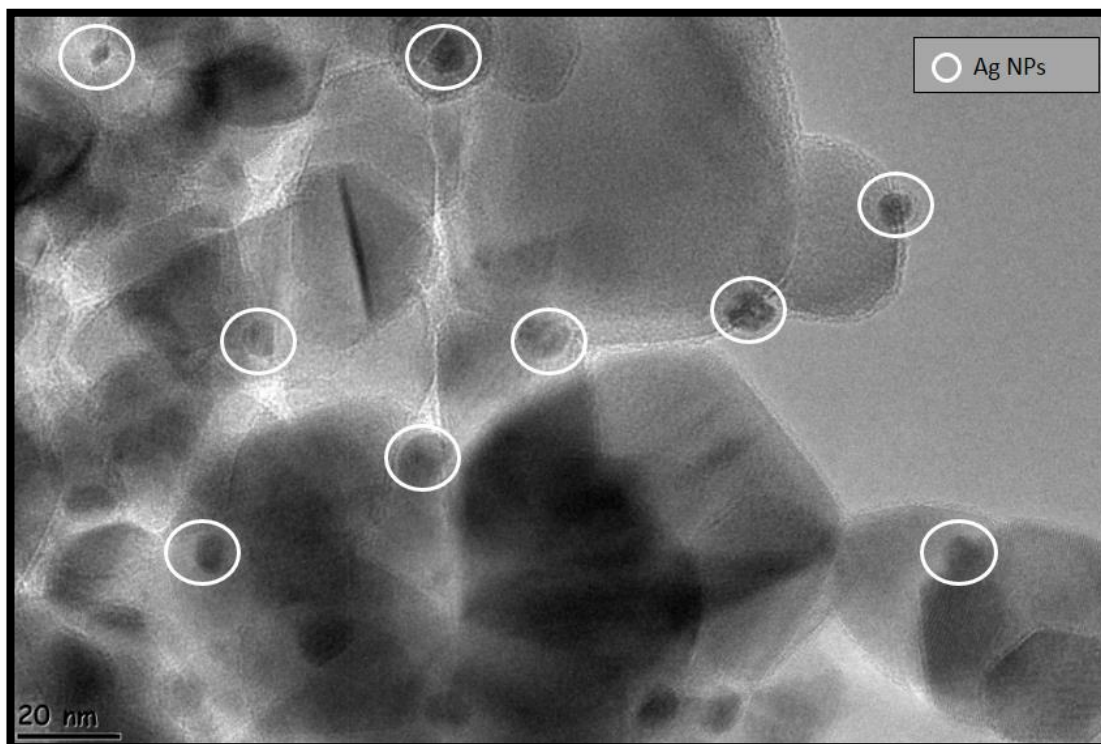


Figure 3.14. TEM image of Ag added  $\text{TiO}_2$  nanoparticles.

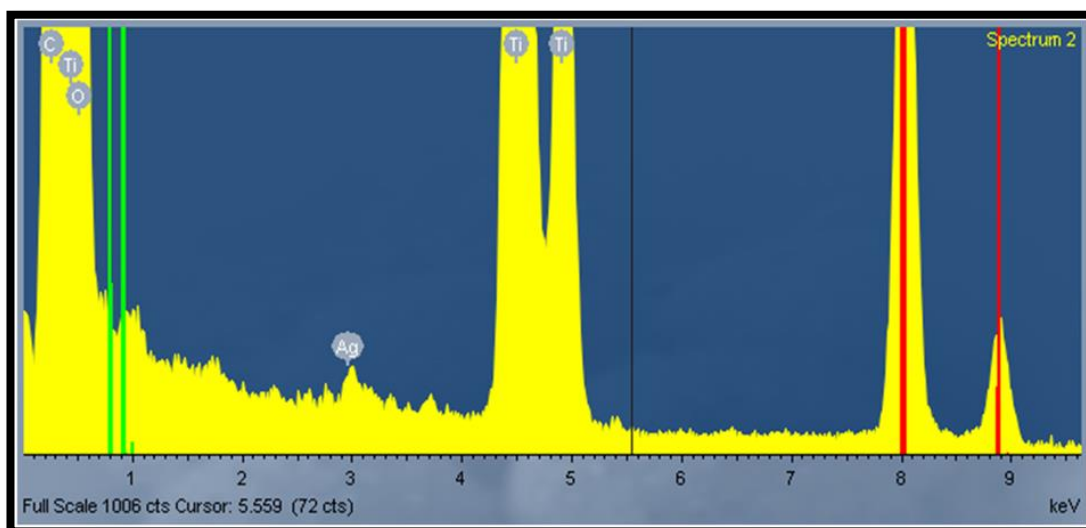
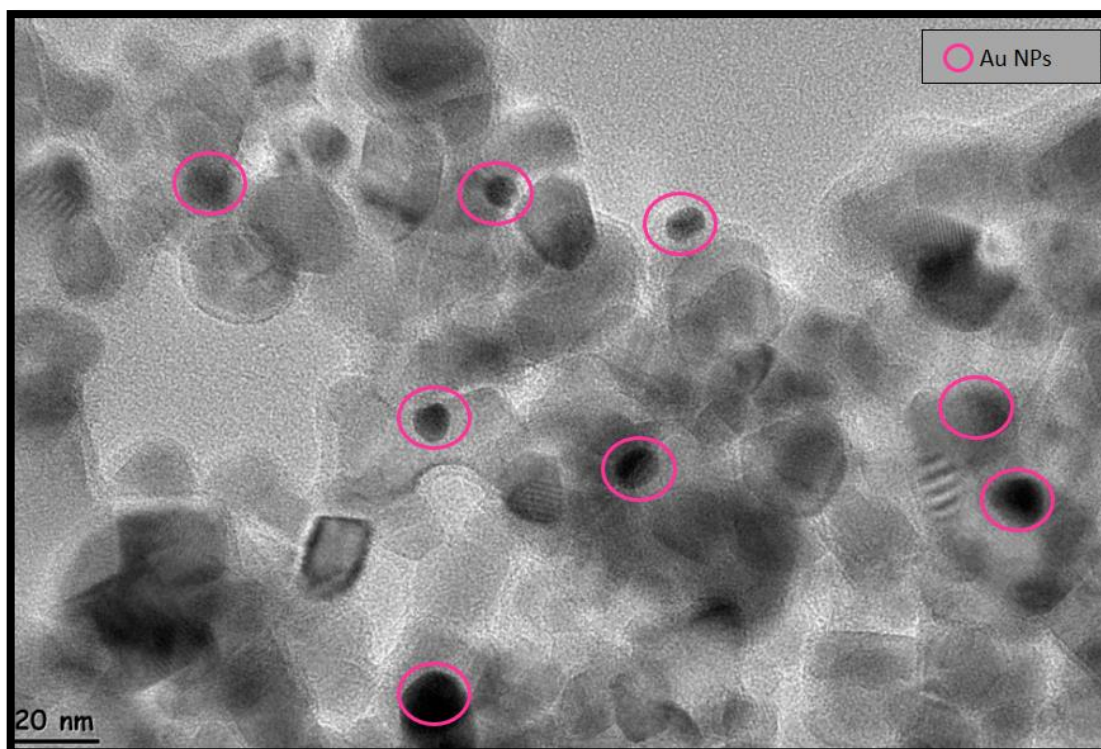


Figure 3.15. EDX Analysis of Ag added  $\text{TiO}_2$ .

The silver signal in EDX pattern proves the attachment of silver nanoparticles to the surface of TiO<sub>2</sub>.

Secondly, the attachment of gold nanoparticles to the surface was achieved. ICP-OES results exhibited that % 0.52 (w/w) addition of Au to the surface was achieved.



*Figure 3.16.* TEM image of Au added TiO<sub>2</sub> nanoparticles.

The surface morphology and elemental composition of prepared Au nanoparticles added TiO<sub>2</sub> nanoparticles can be seen in Figure 3.16 and Figure 3.17, respectively. Size of gold nanoparticles on the surface of TiO<sub>2</sub> was calculated as  $10 \pm 2$  nm. As seen in EDX measurement (Figure 3.17), the presence of a gold signal in the pattern exhibits the addition of gold nanoparticles onto the surface successfully.

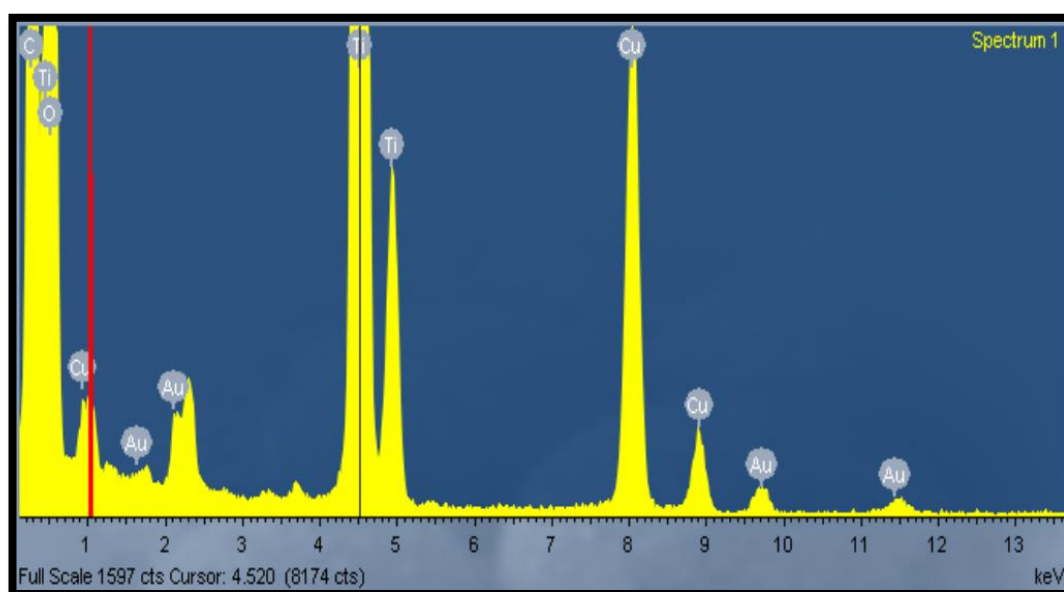


Figure 3.17. EDX pattern of Au added TiO<sub>2</sub> nanoparticles.

### 3.1.5. Characterizations of Silver-Gold Bimetallic Nanoparticle Added TiO<sub>2</sub> Nanoparticles

In order to increase photocatalytic activity TiO<sub>2</sub> nanoparticles were also modified with bimetallic AgAu nanoparticles. All metal ions, initially, were loaded as 1% by mass. According to ICP-OES measurements, the amount of silver and gold added onto TiO<sub>2</sub> nanoparticles was calculated as % 0.68 (w/w) and % 0.45 (w/w), respectively. Figure 3.18 and Figure 3.19 show a TEM image and EDX results of AgAuNPs deposited TiO<sub>2</sub> nanoparticles.

The particle size of bimetallic nanoparticles on the surface was calculated as  $4.0 \pm 2$  nm. TEM image of material exhibit homogeneous particle distribution on the surface. Interestingly, the size of the bimetallic nanoparticles produced on the surface of TiO<sub>2</sub> nanoparticles is smaller compared to the silver and gold nanoparticles added separately. It is known that the structure and morphology of bimetallic nanoparticles strongly depend on the synthetic procedure and miscibility of two metals. Bimetallic

nanoparticles exhibit distinct unique properties than that of corresponding pure monometallic counterparts and their physical mixings. Therefore, they show better photocatalytic performance compared to monometallic ones. Generally, bimetallic nanoparticles have smaller crystallite size which can be attributed to a decrease in both enthalpy and Gibbs free energy of bimetallic nanoparticles during synthesis.

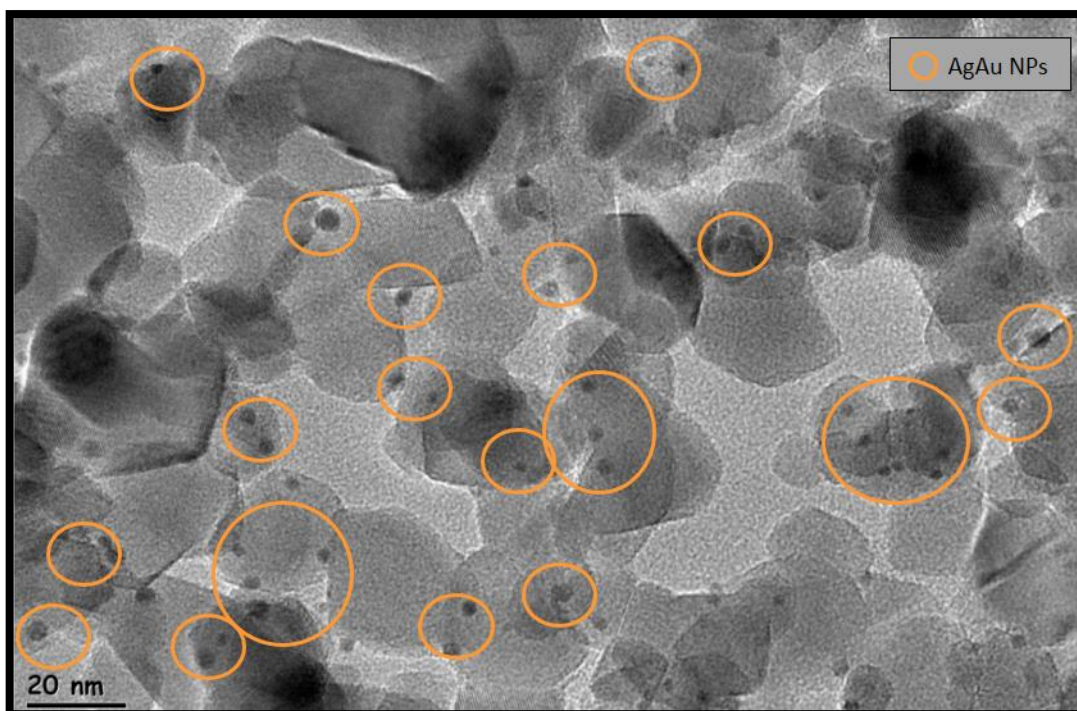


*Figure 3.18.* TEM image of AgAu NPs added TiO<sub>2</sub> nanoparticles.

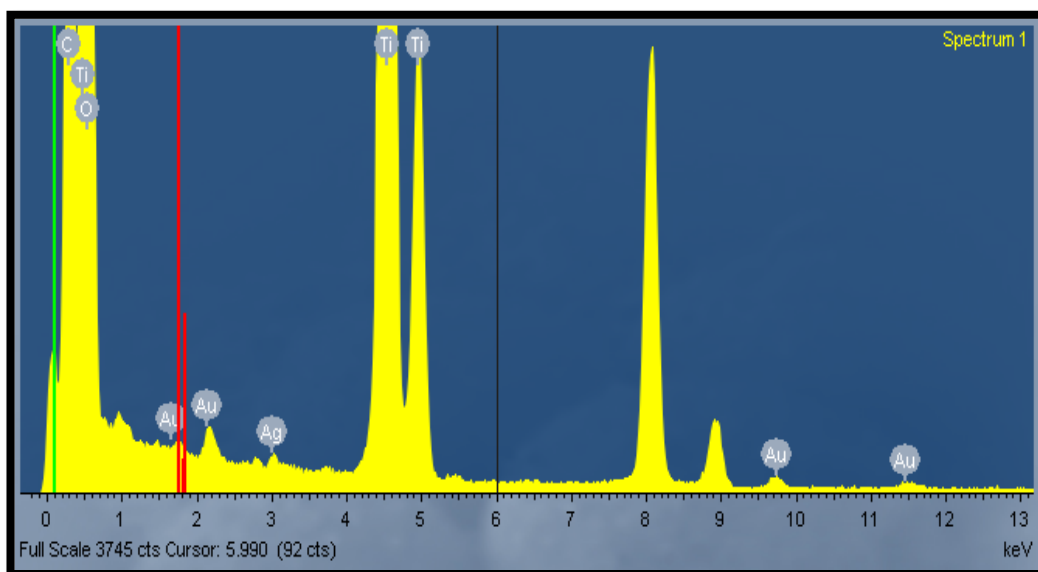


Figure 3.19. EDX pattern of AgAu bimetallic nanoparticles added TiO<sub>2</sub> nanoparticles.

The presence of AgAu bimetallic nanoparticles in the structure was examined by EDX analysis.

### 3.1.6. Characterizations of Silver Nanoparticle Added MNP-PEDOT-TiO<sub>2</sub> Composite Material

As the proposed method for attaching noble metal nanoparticles onto the TiO<sub>2</sub> surface is successful, the same method (liquid impregnation) was also used for MNP-PEDOT-TiO<sub>2</sub>. Initially addition of silver ions onto the composite material was performed. According to ICP-OES results, MNP-PEDOT-TiO<sub>2</sub> composite material contains 0.86 % (w/w) of silver.

TEM image given in Figure 3.20 exhibits homogeneous particle size distribution of silver nanoparticles on the surface. Ag nanoparticles were circled with white color for better sight.



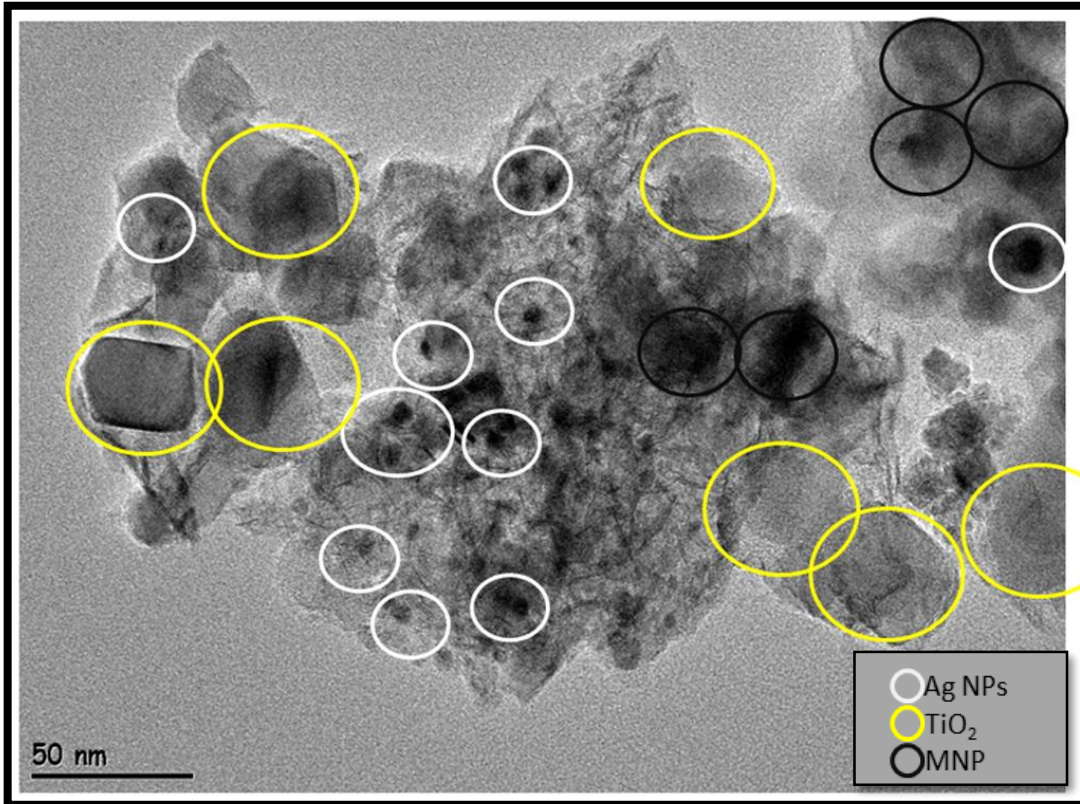


Figure 3.20. TEM image of MNP-PEDOT-TiO<sub>2</sub>-AgNPs composite material.

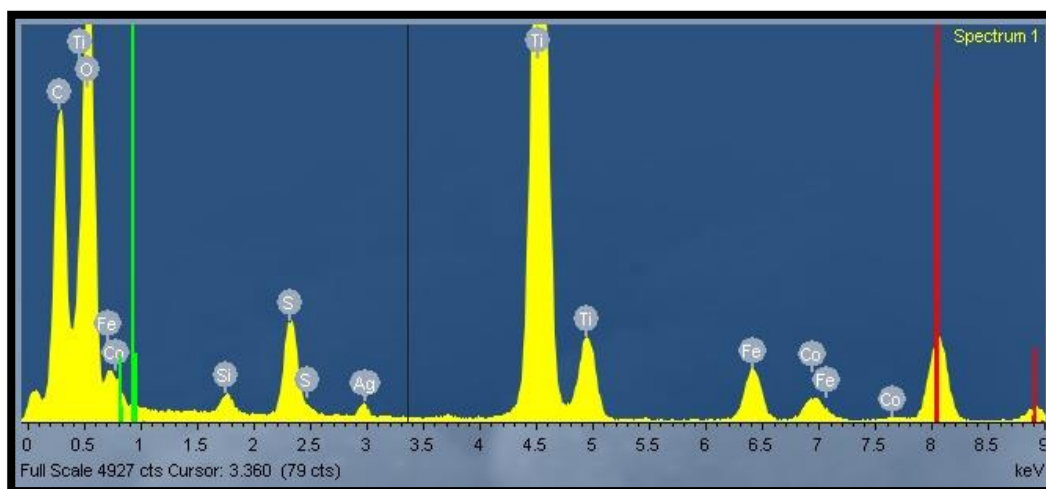


Figure 3.21. EDX pattern of Ag nanoparticle added MNP-PEDOT-TiO<sub>2</sub> composite material.

According to energy dispersive X-ray (EDX) spectroscopy, the presence of Ag signal suggests the successful incorporation of silver to the composite material. On the other hand, the sulfur peak corresponding to PEDOT, and other peaks (silicon, cobalt, and iron) are corresponding to CoFe<sub>2</sub>O<sub>4</sub>@SiO<sub>2</sub> magnetic nanoparticles (Figure 3.21).

### 3.1.7. Characterizations of Gold Added MNP-PEDOT-TiO<sub>2</sub> Composite Material

Addition of gold nanoparticles to the support of MNP-PEDOT-TiO<sub>2</sub> was proven with TEM and EDX measurements given in Figure 3.22 and Figure 3.23, respectively. Small gold nanoparticles on the surface were circled with pink color.

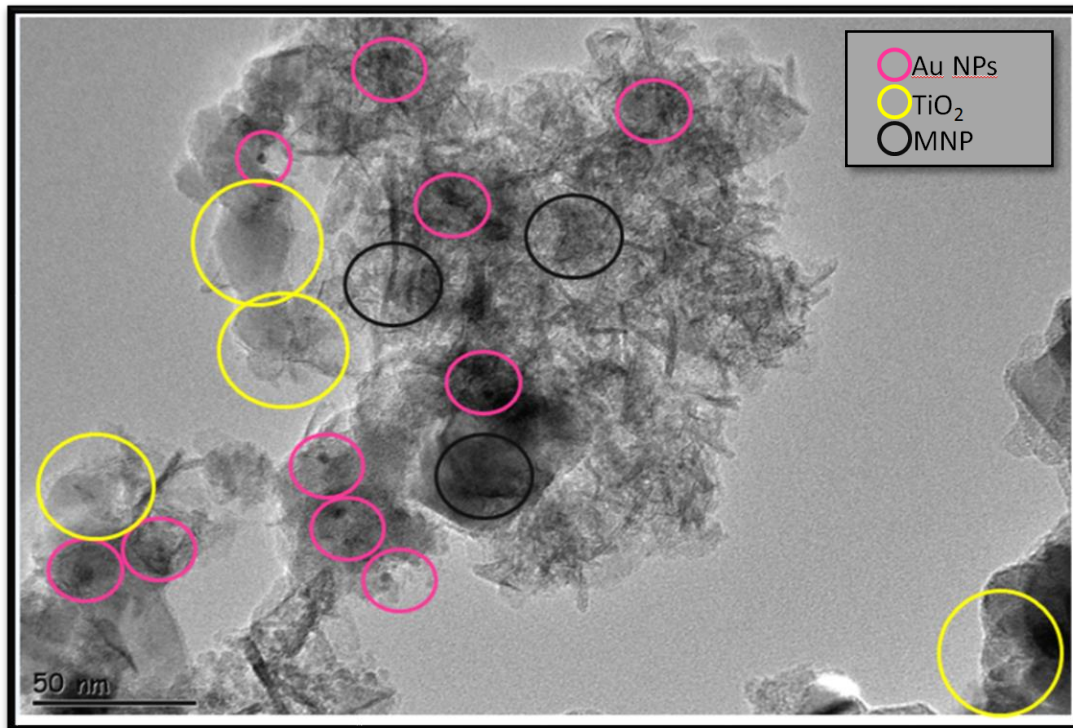


Figure 3.22. TEM image of MNP-PEDOT-TiO<sub>2</sub>-AuNPs composite material.

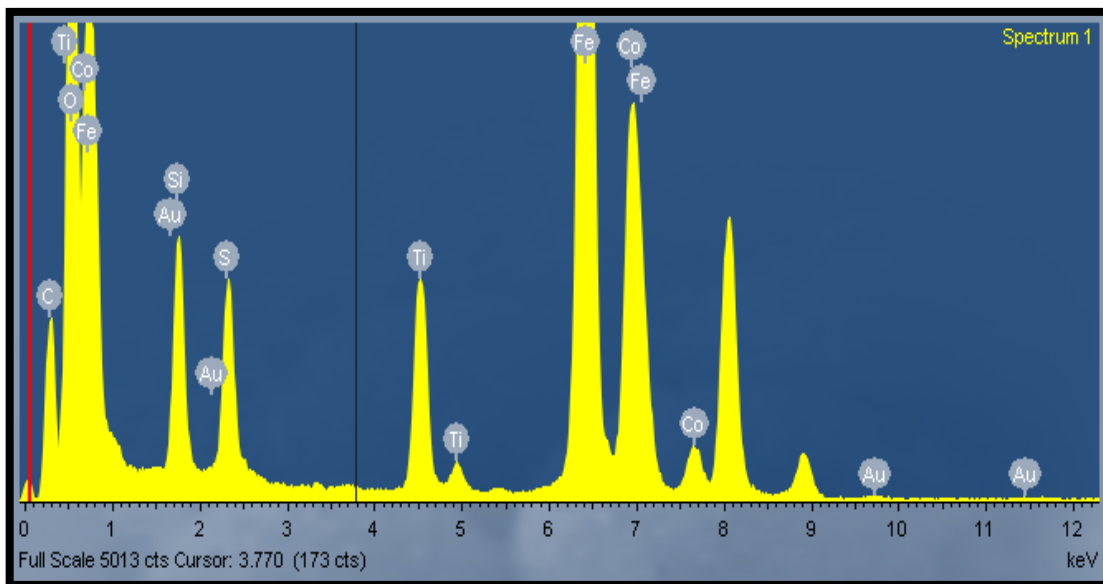


Figure 3.23. EDX pattern of Au nanoparticle added MNP-PEDOT-TiO<sub>2</sub> composite material.



EDX pattern shows the presence of AuNPs on MNP-PEDOT-TiO<sub>2</sub> composite material. The exact amount of gold added onto the composite material was calculated as 0.32% (w/w) by using ICP-OES.

### 3.1.8. Characterizations of Silver-Gold Bimetallic Nanoparticle Added MNP-PEDOT-TiO<sub>2</sub> Composite Material

Finally, silver-gold bimetallic nanoparticles added composite material, MNP-PEDOT-TiO<sub>2</sub>-AgAuNPs, was prepared and morphological properties were investigated by using TEM. TEM image of the composite material is given in Figure 3.24.

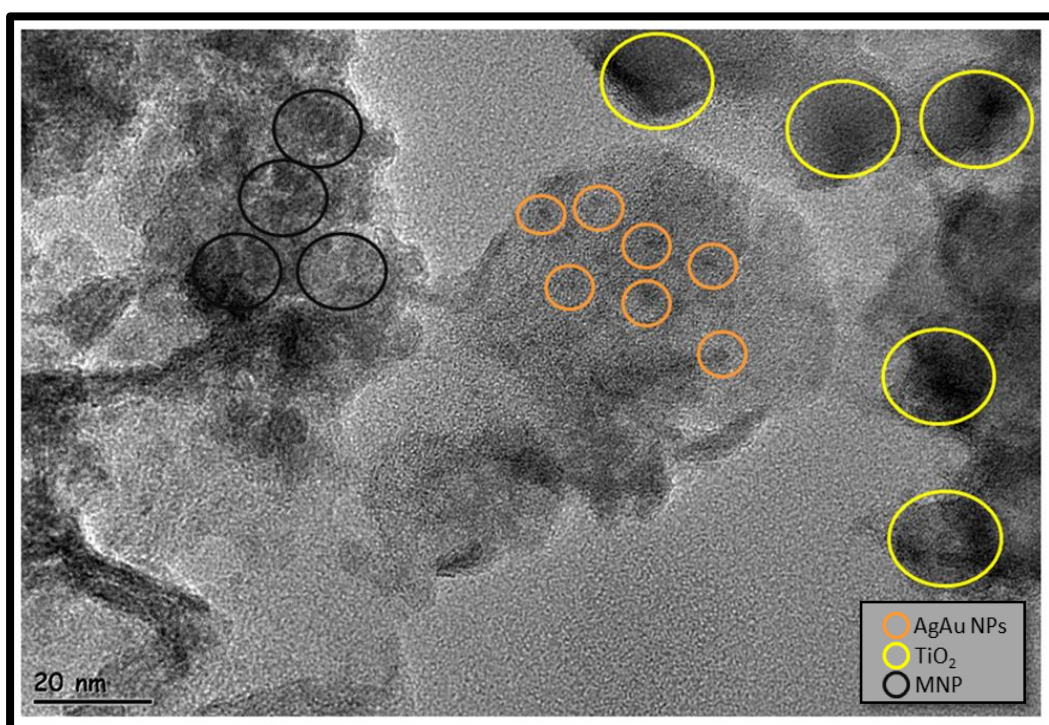


Figure 3.24. TEM image of MNP-PEDOT-TiO<sub>2</sub>-AgAuNPs.

From the Figure 3.24, each of the components that make up the composite material can be seen. The presence of silver and gold in the composite material was also proven with EDX measurement given in Figure 3.25.

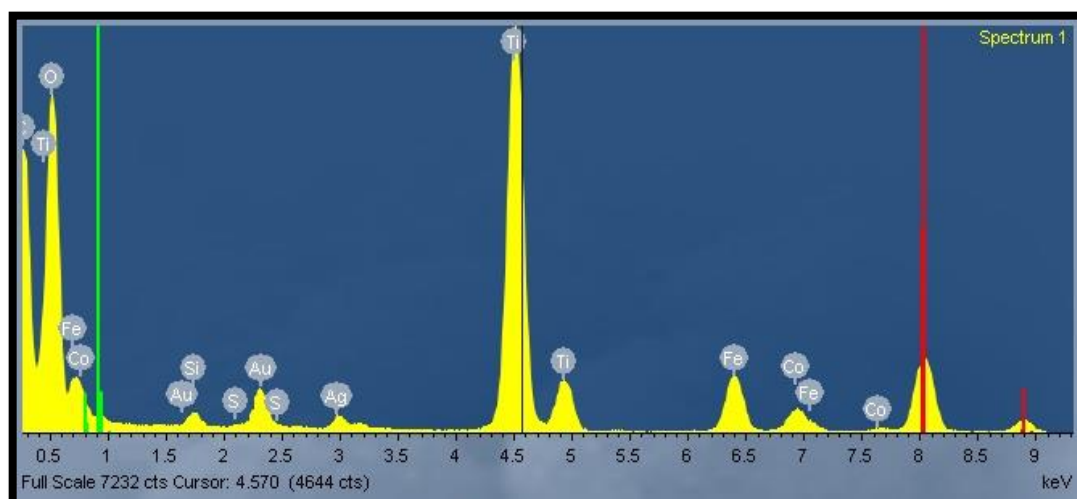


Figure 3.25. EDX pattern of AgAu nanoparticle added MNP-PEDOT-TiO<sub>2</sub> composite material.

Ag and Au signals appearing in the EDX pattern are the indications of the addition of AgAuNPs onto the MNP-PEDOT-TiO<sub>2</sub> composite material. The exact amounts of silver and gold added to the composite material were found as 0.79 % (w/w) and 0.28 % (w/w), respectively by using ICP-OES.

## 3.2. Photocatalytic Activity Results of Prepared Composite Materials

### 3.2.1. Adsorption Profiles of the Prepared Nanostructures

It is very important to reveal the adsorption behavior of photocatalytic materials to prove the photocatalytic degradation of the target molecule under light irradiation. Thus, before starting to light irradiation, the MB solution and photocatalyst were mixed and stirred in dark to find the adsorption behavior. For this, the adsorption

behavior of TiO<sub>2</sub> nanoparticle was investigated initially in order to compare with composite materials prepared during the study. The result is given in Figure 3.26.

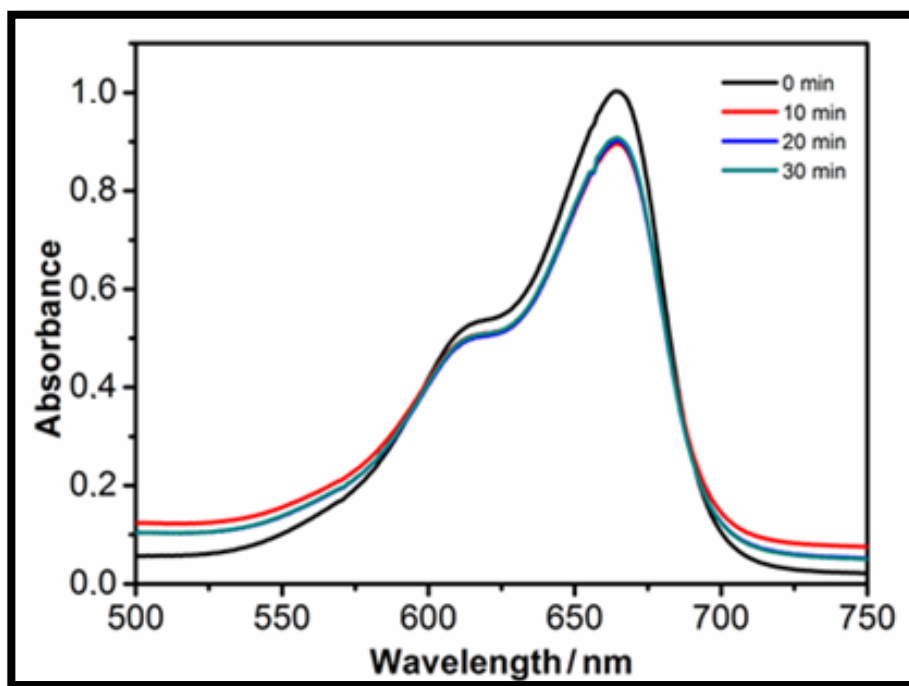


Figure 3.26. UV-Vis spectra of the MB solution taken initially and after mixed with 10 mg of TiO<sub>2</sub> nanoparticles under dark environment for different durations.

Figure 3.26 shows a series of absorption maxima of the MB solution treated with 10 mg of TiO<sub>2</sub> nanoparticle as a photocatalyst under dark for different durations. According to Figure 3.26, the highest adsorption value was obtained after 10 min mixing under dark condition. The stirring process was continued for 30 minutes. The absorption maxima of MB located at about 660 nm decreases by about 11 % at the end of 30 min. period. Percent adsorption values are given in Table 3.1.

Table 3.1. *Percent adsorption values of TiO<sub>2</sub> nanoparticle under dark condition for different durations.*

<b>Time (min)</b>	<b>Adsorption %</b>
10	11.3
20	10.9
30	10.8

According to the obtained results, the total adsorption time for TiO<sub>2</sub> nanoparticles based catalysts was chosen as 10 min (Table 3.1). So before the light illumination, each TiO<sub>2</sub> nanoparticles based catalyst (TiO<sub>2</sub>, TiO<sub>2</sub>-AgNPs, TiO<sub>2</sub>-AuNPs, TiO<sub>2</sub>-AgAuNPs) was mixed with MB solution for 10 min. After that, the adsorption behavior of MNP-PEDOT-TiO<sub>2</sub> composite material was investigated. The results are given in Figure 3.27 and Table 3.2.

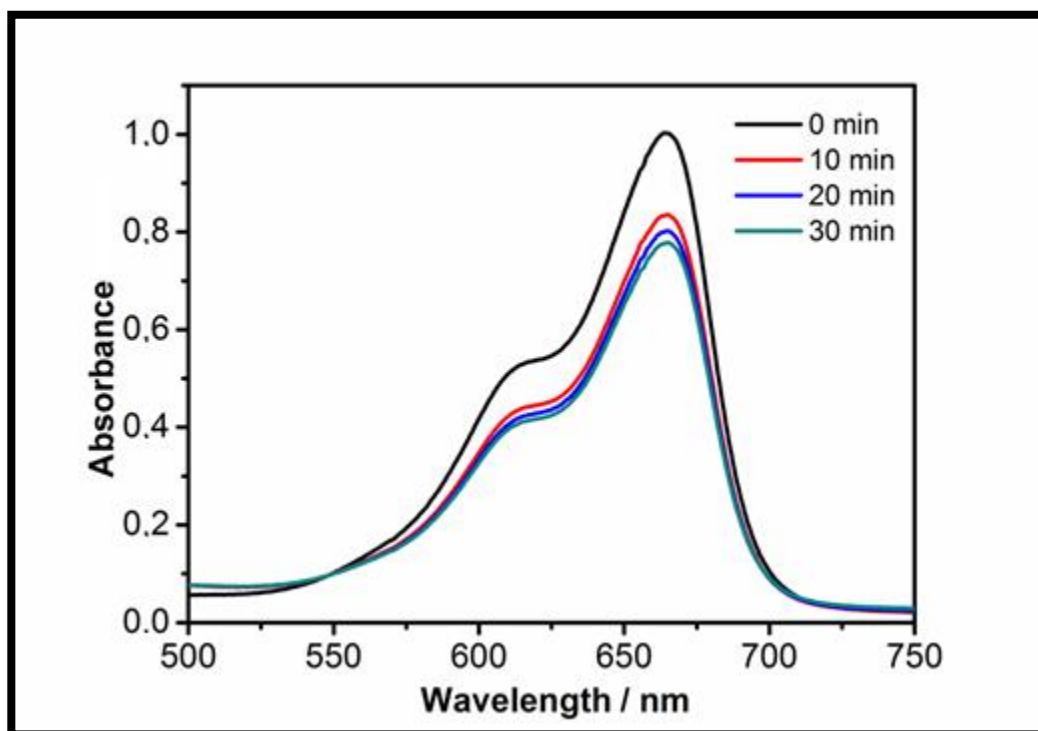


Figure 3.27. UV-Vis spectra of the MB solution taken initially and after mixed with 10 mg of MNP-PEDOT-TiO<sub>2</sub> composite material under dark environment for different durations.

Table 3.2. Percent adsorption values of MNP-PEDOT-TiO<sub>2</sub> composite material under dark condition for different durations.

Time (min)	Adsorption %
10	16.3
20	17.6
30	17.1

From Figure 3.27 and Table 3.2, the highest adsorption was detected at the end of the 20 min mixing time under dark condition. The absorption maxima of MB located at about 660 nm decreases by about 18 % at the end of 20 min dark treatment. So, the optimum mixing time before light exposure was founded as 20 min and applied for MNP-PEDOT-TiO<sub>2</sub> composite material based catalysts (MNP-PEDOT-TiO<sub>2</sub>, MNP-PEDOT-TiO<sub>2</sub>-AgNPs, MNP-PEDOT-TiO<sub>2</sub>-AuNPs, MNP-PEDOT-TiO<sub>2</sub>-AgAuNPs) before light illumination. After revealing the adsorption behaviors, the catalytic activity of the prepared materials in the degradation of MB dye under UV and solar light was investigated.

### **3.2.2. Photocatalytic Activity of the Prepared Structures Under UV Light Illumination**

In this part of the study, the photocatalytic activity of prepared materials was investigated in the degradation of MB under UV light. 10 mg catalyst was used to provide photocatalytic degradation of 10 mL,  $2.2 \times 10^{-5}$  M MB in each try. The percent methylene blue degradation capacity of catalysts was determined by measuring a 2 mL solution from the reaction medium every 10 minutes and measured by using UV-Vis spectrometer. During the measurements, the absorption peak located at 660 nm was followed. Then the solution used in the measurement was added to the reaction medium and the same method was followed until the end of the photocatalytic experiment. The percent degradation was calculated by using the equation given in the experimental part.

To obtain proper information about the degradation of MB driven with the photocatalytic process, initially, the experiment was performed in the absence of catalyst and no decolorization was observed. After that, the photocatalytic activities of TiO<sub>2</sub> nanoparticles (Degussa P25) and PEDOT polymer were investigated as reference photocatalysts for comparison with the structures prepared during the study. Photocatalytic degradation and percent removal of methylene blue under UV light

illumination in the presence of 10 mg TiO<sub>2</sub> nanoparticles (Degussa P25) is given in Figure 3.28 and Table 3.3 respectively.

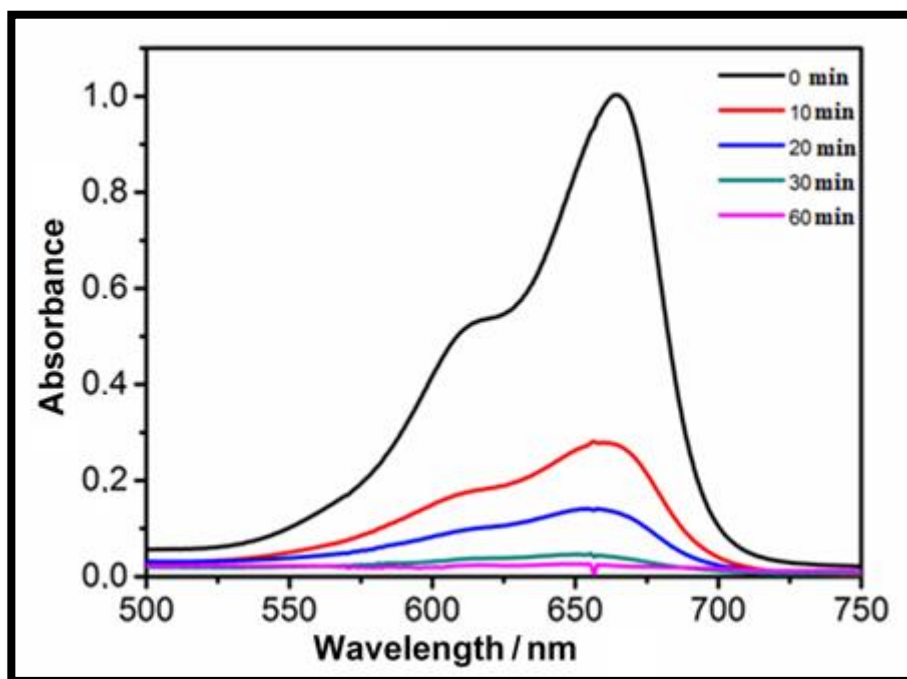


Figure 3.28. UV-Vis spectra of the MB solution shows the photocatalytic degradation of MB under UV light in the presence of 10 mg TiO<sub>2</sub> nanoparticles (Degussa P25) for different durations.

Table 3.3. Percent dye degradation efficiency of TiO<sub>2</sub> nanoparticles under UV light for different durations.

Time (min)	Removal %
10	66.0
20	81.8
30	93.2
60	99.5

According to the results, the complete degradation of MB under UV light was achieved at the end of the 60 min. period by using given photocatalytic system.

After that, the activities of the prepared materials were measured by applying the same method under the same conditions. In all UV-Vis measurements, the absorption maxima located at 660 nm was followed and the same type of spectra was recorded. In order to make comparison easier, all results related to photocatalytic degradation of MB UV light are given in Table 3.4.

Table 3.4. Calculated percent dye degradation results of all catalysts prepared in this study under UV light for different durations.

Catalysts (10 mg)	% Degr. 10 min	% Degr. 20 min	% Degr. 30 min	% Degr. 40 min	% Degr. 50 min	% Degr. 60 min
MNP (SiO <sub>2</sub> -CoFe <sub>2</sub> O <sub>4</sub> )	3.00	5.00	-	-	-	-
TiO <sub>2</sub>	66.0	81.8	93.2	99.2	99.4	99.5
TiO <sub>2</sub> /Ag <sup>0</sup>	87.2	99.5	99.7	99.7	99.7	99.7
TiO <sub>2</sub> /Au <sup>0</sup>	78.3	89.5	95.1	98.1	98.3	98.3
TiO <sub>2</sub> /Au <sup>0</sup> Ag <sup>0</sup>	80.5	90.1	94.4	97.3	99.6	99.6
PEDOT	39.4	50.4	68.1	79.2	88.9	95.0
MNP-PEDOT	57.1	80.7	89.2	91.6	94.5	95.2
MNP-PEDOT-TiO <sub>2</sub>	82.9	91.1	97.4	99.4	99.4	99.4
MNP-PEDOT-TiO <sub>2</sub> /Ag <sup>0</sup>	89.6	96.3	99.5	99.5	99.5	99.6
MNP-PEDOT-TiO <sub>2</sub> /Au <sup>0</sup>	92.7	95.4	99.5	99.4	99.4	99.4
MNP-PEDOT-TiO <sub>2</sub> /Au <sup>0</sup> Ag <sup>0</sup>	88.4	92.3	98.4	99.5	99.5	99.5

- A blank correction was applied and  $\pm$  standard deviation founded around 1%.



As can be seen from the results, complete removal of MB was obtained after 60 min with  $\text{TiO}_2$  nanoparticle under UV light illumination. Total degradation time shortened with the addition of metal nanoparticles to  $\text{TiO}_2$  nanoparticle. The total degradation was achieved in 20 min with the addition of AgNPs. Total degradation was achieved at the end of the 40 and 50 min UV light illumination by using the structures obtained by doping  $\text{TiO}_2$  nanoparticles with AuNPs and AgAuNPs, respectively. According to the results, it can be concluded that doping of  $\text{TiO}_2$  nanoparticles with noble metal nanoparticles (AgNPs, AuNPs, and AgAuNPs) increases the catalytic activity of the resulting nanostructure. The comparison of the  $\text{TiO}_2$  nanoparticles based catalyst is given in Figure 3.29.

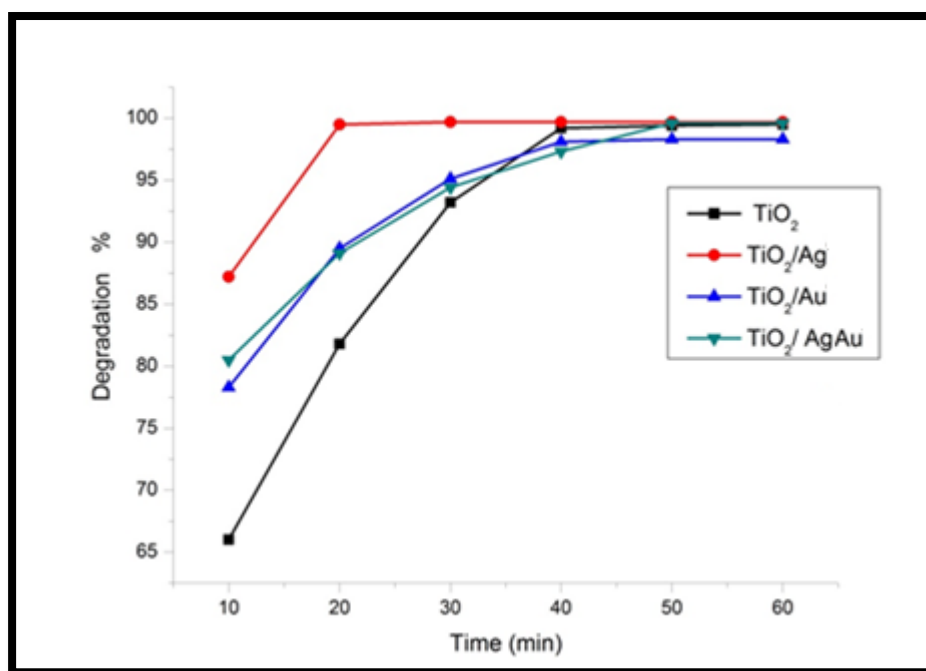


Figure 3.29. Comparison of the percent degradation of MB under UV light by using a)  $\text{TiO}_2$ , b)  $\text{TiO}_2$ -AgNPs, c)  $\text{TiO}_2$ -AuNPs and d)  $\text{TiO}_2$ -AgAuNPs catalysts.

The total degradation time of MB under UV light illumination decreases from 60 min to 20 min with the addition of 1.15% (w/w) silver nanoparticles to the TiO<sub>2</sub> nanoparticles. In the case of 0.52 % (w/w) gold nanoparticles addition, the total degradation time of MB decreases from 60 min to 40 min. Finally, doping TiO<sub>2</sub> nanoparticles with bimetallic AgAu nanoparticles, (0.68 % (w/w) Ag and 0.45 (w/w) % Au), shortened the total degradation time of MB under UV light from 60 min to 50 min. The highest photocatalytic activity and the initial rate for MB removal under UV light were obtained with the usage of TiO<sub>2</sub>-AgNPs. The shorter absorption maxima ( $\lambda=420$  nm) when compared with gold nanoparticles ( $\lambda=520$  nm) and the higher amount of silver nanoparticles (1.15%) in the structure can be the reasons for the highest activity of TiO<sub>2</sub>-AgNPs nanoparticles.

In the case of PEDOT, 95% removal of MB was achieved at the end of the 60 min UV light. The similar result obtained with the usage of MNP-PEDOT as the photocatalyst. But, MNP-PEDOT contains only 5 mg PEDOT. Although the amount of PEDOT was decreased to its half, the similar total removal of MB was obtained with a higher initial rate. This can be attributed to the increase of the total surface area with the addition of MNP to the PEDOT.

For MNP-PEDOT-TiO<sub>2</sub> composite material used as a photocatalyst, the characteristic absorption band of MB at about 660 nm decreases gradually over time and finally almost disappears within 40 min which is the indication of total degradation. Comparison of the % MB degradation obtained by using MNP-PEDOT-TiO<sub>2</sub> with TiO<sub>2</sub> nanoparticles, PEDOT and MNP-PEDOT composite material is given in Figure 3.30.

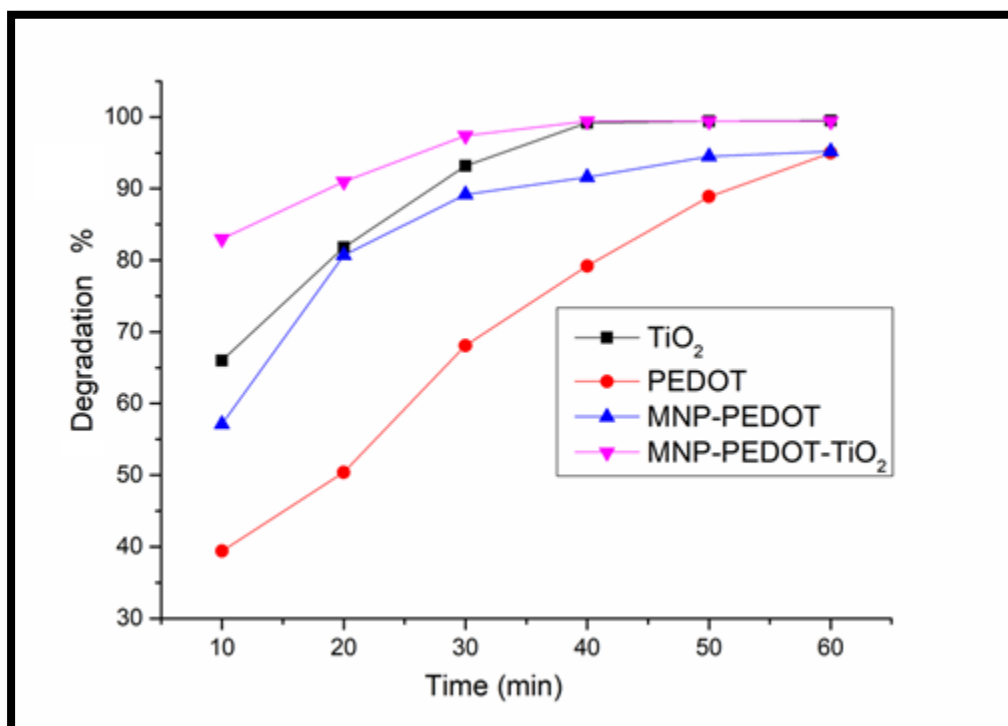


Figure 3.30. Comparison of the percent degradation of MB under UV light by using a) TiO<sub>2</sub>, b) PEDOT, c) MNP-PEDOT and d) MNP-PEDOT-TiO<sub>2</sub>.

As can be seen from the Table 3.5 and Figure 3.30, the degradation efficiency reaches up to 83% in 10 min and nearly complete removal of MB was obtained after 40 min under the same conditions by using MNP-PEDOT-TiO<sub>2</sub> as a catalyst. The comparison of the initial rates of the structures mentioned above is given in Table 3.5.

Table 3.5. The comparison of the initial rates of the MNP-PEDOT-TiO<sub>2</sub> with TiO<sub>2</sub>, PEDOT and MNP-PEDOT catalyst.

Catalysts (10 mg)	Degr. % after 10 min
TiO <sub>2</sub>	66.0
PEDOT	39.4
MNP-PEDOT (contains 5 mg PEDOT)	57.1
MNP-PEDOT-TiO <sub>2</sub> (contains 3 mg PEDOT and 2 mg TiO <sub>2</sub> )	82.9

According to the results given in Table 5, the initial degradation rate of MB obtained with TiO<sub>2</sub> nanoparticles increase from 66 % to 83% with the addition of PEDOT and MNP. Additionally, 10 mg MNP-PEDOT-TiO<sub>2</sub> composite material contains only 2 mg TiO<sub>2</sub> nanoparticles and 3 mg PEDOT. Although MNP-PEDOT-TiO<sub>2</sub> composite material contains a smaller amount of TiO<sub>2</sub>, it shows better catalytic activity than 10 mg pure TiO<sub>2</sub> nanoparticles and PEDOT polymer. In order to support this conclusion, an additional experiment was performed. In this experiment, 2 mg TiO<sub>2</sub> nanoparticles were used as the photocatalyst and the result obtained was used for comparison with MNP-PEDOT-TiO<sub>2</sub> composite material (Table 3.6.).

Table 3.6. *The comparison of the percent degradation of MB under UV light by using 2 mg TiO<sub>2</sub> nanoparticles and MNP-PEDOT-TiO<sub>2</sub> which contains 2 mg TiO<sub>2</sub> nanoparticles.*

<b>Time (min)</b>	<b>Removal % with TiO<sub>2</sub> (2 mg)</b>	<b>Removal % with MNP-PEDOT-TiO<sub>2</sub> containing 2 mg TiO<sub>2</sub></b>
10	21.6	82.9
20	22.3	91.1
30	22.5	97.4
40	23.1	99.4
50	23.8	99.4
60	24.6	99.4
90	24.7	-
120	24.9	-
180	25.1	-

As can be seen from Table 3.6, only 25% removal of MB was achieved after 180 min with the use of 2 mg TiO<sub>2</sub> nanoparticles catalyst. In the case of MNP-PEDOT-TiO<sub>2</sub> composite material which contains 2 mg TiO<sub>2</sub> nanoparticles, the total degradation of MB was obtained at the end of 40 min.

This suggests that the presence of PEDOT polymer and the synergetic interaction with TiO<sub>2</sub> plays a very important role in the photocatalytic activity of the prepared composite material. A conclusion may be given that doping TiO<sub>2</sub> nanoparticle with PEDOT polymer can remarkably increase the photocatalytic activity by increasing the

charge separation, formation of electron ( $e^-$ ) and hole ( $h^+$ ) pairs, due to its proper  $E_g$  values (1.65 eV) which allows the  $e^-$  and  $h^+$  transfer between HOMO-LUMO (-5.40 eV, -3.75 eV) levels of PEDOT and VB-CB (-7.4 eV, -4.2 eV) levels of  $TiO_2$  nanoparticles. Besides the high photocatalytic activity, MNP-PEDOT- $TiO_2$  composite material has an advantage of magnetic separation. The presence of PEDOT not only increases the photocatalytic activity but also allows the addition of magnetic nanoparticles which gives the magnetic property to the final structure. Due to this property, the catalyst can be separated from the reaction medium for reuse without the need for separation processes that require a long time and also the pollution caused by the catalyst will be prevented.

Finally, effect of the addition of noble metal nanoparticles onto the MNP-PEDOT- $TiO_2$  composite material throughout the photocatalytic activity test was figured out by comparing the results obtained for degradation of MB under UV light with the usage of MNP-PEDOT- $TiO_2$ , MNP-PEDOT- $TiO_2$ -AgNPs, MNP-PEDOT- $TiO_2$ -AuNPs and MNP-PEDOT- $TiO_2$ -AgAuNPs, respectively. Comparison of the results is given in Figure 3.31.

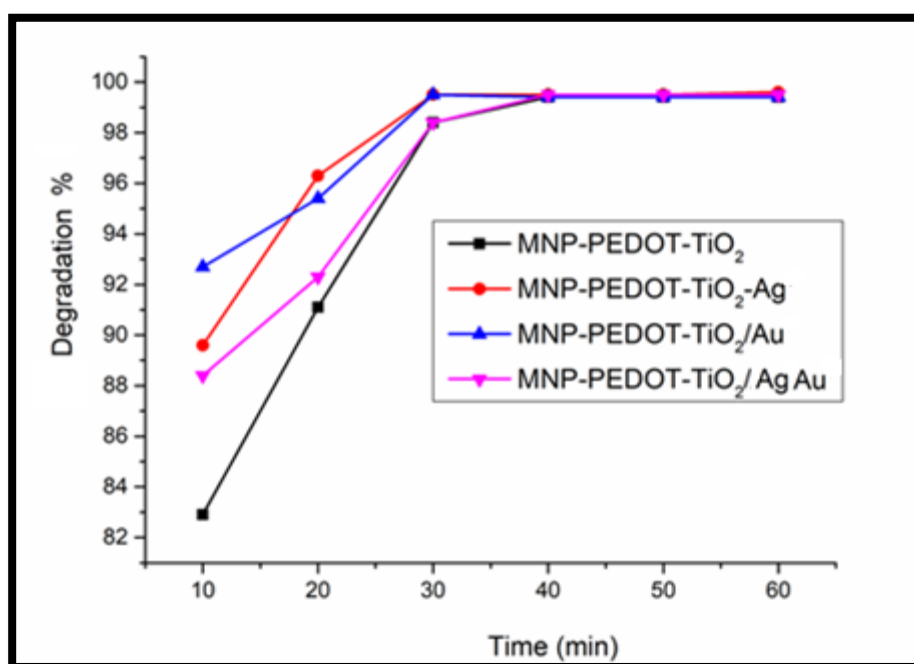


Figure 3.31. Comparison of the percent degradation of MB under UV light by using a) MNP-PEDOT-TiO<sub>2</sub>, b) MNP-PEDOT-TiO<sub>2</sub>-AgNPs, c) MNP-PEDOT-TiO<sub>2</sub>-AuNPs and d) MNP-PEDOT-TiO<sub>2</sub>/AgAuNPs.

The highest initial decomposition rate of MB (93% at 10 min.) was obtained with the usage of MNP-PEDOT-TiO<sub>2</sub>-AuNPs composite material as a catalyst which contains only 0.52 % Au. Total degradation of MB was achieved only after 30 min UV light by using MNP-PEDOT-TiO<sub>2</sub>-AuNPs, MNP-PEDOT-TiO<sub>2</sub>-AgNPs, and MNP-PEDOT-TiO<sub>2</sub>-AgAuNPs composite material as a catalyst. According to the results, it can be concluded that the addition of noble metal nanoparticles onto the MNP-PEDOT-TiO<sub>2</sub> increases the photocatalytic activity due to their surface plasmon resonance property by transferring electrons to the conduction bands of TiO<sub>2</sub> nanoparticles and LUMO level of PEDOT generated from plasmon excitation and also by increasing the separation efficiency of e-h pairs.

### 3.2.3. Photocatalytic Activity of the Prepared Structures Under Solar Light Illumination

In this part of the study, the photocatalytic activity of the proposed materials under solar light was investigated in the degradation of MB dye. The same reaction conditions and experimental parameters were used as in the previous section. During the UV-Vis measurements, the absorption peak located at 660 nm was followed at every 10 min and percent degradation was calculated from the absorption maxima by using the equation given in the experimental part. Because of the large number of catalysts, only the spectra which show the time-dependent degradation of MB obtained with titanium nanoparticles as catalyst under solar light as an example is given in Figure 3.32. All calculated percent degradation values are given in Table 3.7.

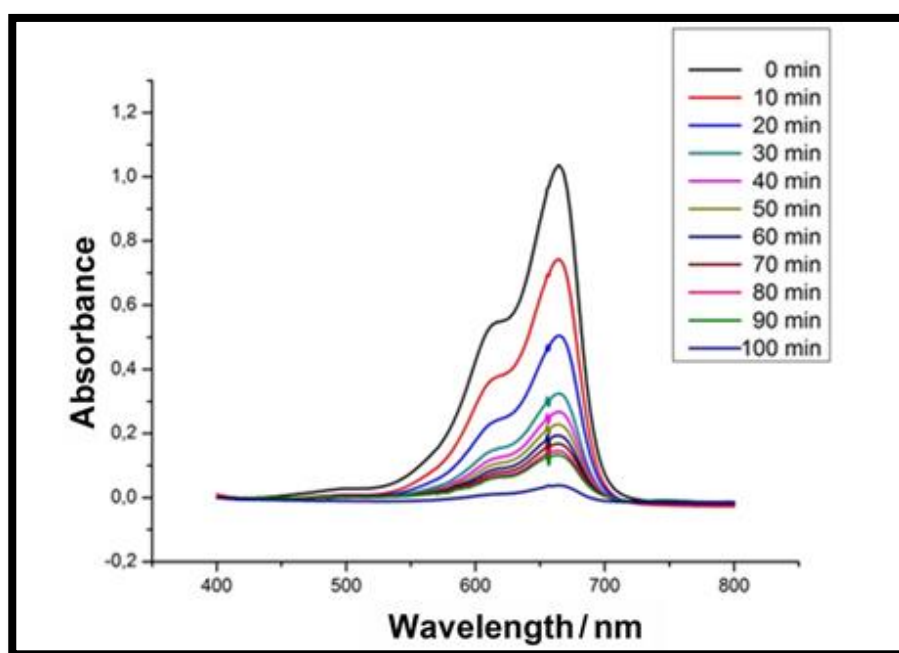


Figure 3.32. UV-Vis spectra of the MB solution shows the photocatalytic degradation of MB under solar light illumination in the presence of 10 mg TiO<sub>2</sub> nanoparticles (Degussa P25) for different durations.



Table 3.7. Calculated percent dye degradation results of all catalysts prepared in this study from UV-Vis spectra obtained under solar light for different durations.

Catalysts	Degr. % 10 min	Degr. % 20 min	Degr. % 30 min	Degr. % 40 min	Degr. % 50 min	Degr. % 60 min	Degr. % 120 min
TiO <sub>2</sub>	39.1	43.2	55.0	68.3	75.6	86.4	96.2
TiO <sub>2</sub> /Ag <sup>0</sup>	30.5	43.1	57.9	75.2	81.8	89.2	95.6
TiO <sub>2</sub> /Au <sup>0</sup>	56.8	72.2	81.9	91.1	96.0	99.5	-
TiO <sub>2</sub> /Ag <sup>0</sup> Au <sup>0</sup>	59.5	74.4	83.8	94.4	98.9	99.0	-
PEDOT	30.6	52.1	69.2	74.6	78.4	81.6	95.2
MNP-PEDOT	36.2	70.7	84.1	86.2	87.9	89.3	94.6
MNP-PEDOT-TiO <sub>2</sub>	43.1	80.3	90.9	95.5	96.3	96.8	-
MNP-PEDOT-TiO <sub>2</sub> /Ag <sup>0</sup>	80.5	99.2	99.3	99.3	99.3	-	-
MNP-PEDOT-TiO <sub>2</sub> /Au <sup>0</sup>	83.1	99.3	99.6	99.6	-	-	-
MNP-PEDOT-TiO <sub>2</sub> /Ag <sup>0</sup> Au <sup>0</sup>	85.4	99.5	99.5	99.5	99.5	-	-

- A blank correction was applied and the  $\pm$  standard deviation was founded around 1%.

According to the results, at the end of the 120 min period, complete degradation of MB was not achieved with TiO<sub>2</sub> nanoparticles under solar light illumination. The same type of behavior was recorded for AgNPs doped TiO<sub>2</sub> nanoparticles. In the case of TiO<sub>2</sub> nanoparticles doped with AuNPs and AgAuNPs complete degradation of MB was achieved after 60 min of solar light exposure. The comparison of the degradation of MB obtained by using TiO<sub>2</sub> nanoparticles with doped ones is given in Figure 3.33.

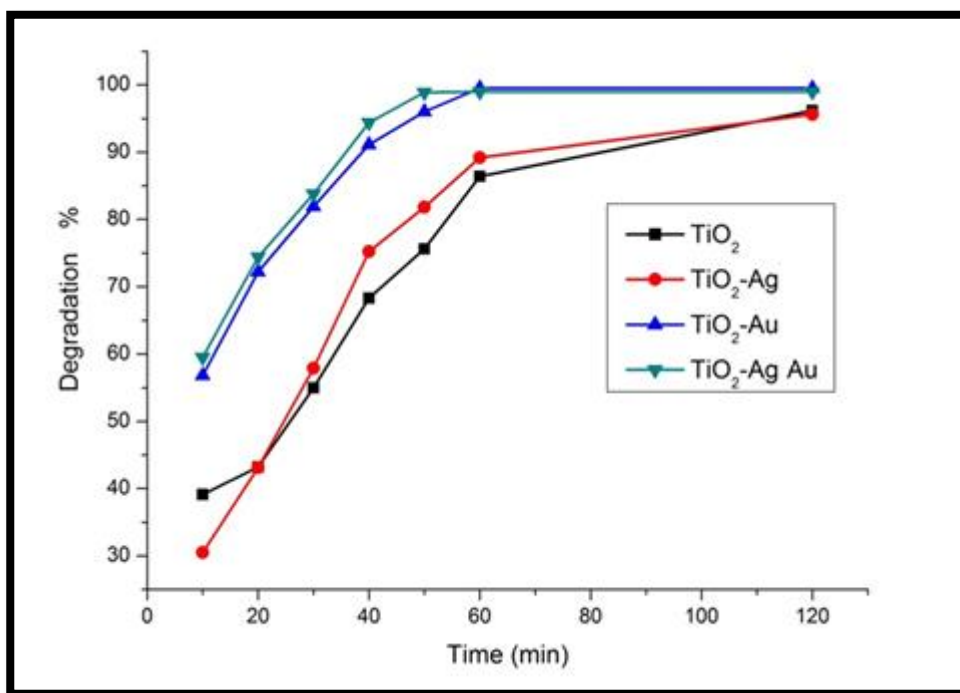


Figure 3.33. Comparison of the percent degradation of MB under solar light by using a) TiO<sub>2</sub>, b) TiO<sub>2</sub>-AgNPs, c) TiO<sub>2</sub>-AuNPs and d) TiO<sub>2</sub> AgAuNPs.

As can be seen from the Figure 3.33, the initial decomposition rate of the MB obtained with TiO<sub>2</sub>-AuNPs (0.52 % (w/w) Au) and TiO<sub>2</sub>-AgAuNPs (0.68 % (w/w) Ag and 0.45 (w/w) % Au ) was calculated nearly the same. The addition of AuNPs and AgAuNPs increased the catalytic activity and the total degradation time shortened from 120 min to 60 min. The highest activity was obtained with TiO<sub>2</sub>-AgAuNPs nanostructures under solar light. The higher activity can be related to smaller sized AgAuNPs (4 nm) formed on TiO<sub>2</sub> nanoparticles when comparing with AgNP and AuNPs. Finally, the addition of AgNP to TiO<sub>2</sub> nanoparticles has not changed the activity under solar light.

The catalytic activity of PEDOT was slower under solar light when compared with the activity recorded under UV light. Only 95% degradation of MB was observed at the end of the 120 min under solar light illumination. Although, the addition of MNP

was increased the initial rate of decomposition from 30% to 36%, the time needed for total degradation was not changed. At the end of the 120 min 96% removal of MB was obtained with the usage of MNP-PEDOT as a catalyst. The addition of TiO<sub>2</sub> nanoparticles into the MNP-PEDOT structure completely changed the catalytic behavior of the final structure, MNP-PEDOT-TiO<sub>2</sub>. Comparison of the result is given in Figure 3.34.

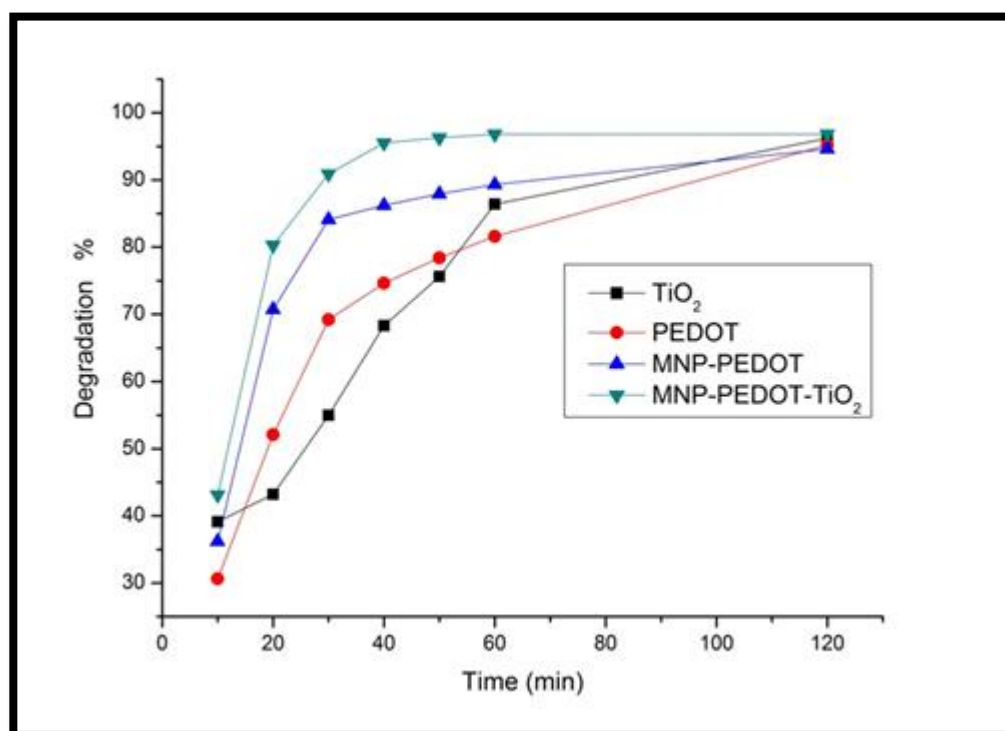


Figure 3.34. Comparison of the percent degradation of MB under solar light by using a) TiO<sub>2</sub>, b) PEDOT, c) MNP-PEDOT and d) MNP-PEDOT-TiO<sub>2</sub> catalyst.

The maximum percent degradation of MB under solar light was noted as 97% in 60 min. The decrease in the activity of TiO<sub>2</sub> and PEDOT with solar light exposure is related to a decrease in charge separation efficiency due to the usage of the source (solar light) carrying less energy. After doping TiO<sub>2</sub> nanoparticles with PEDOT, although performing degradation of MB under solar light (contains mostly visible

radiation) total degradation was achieved in 60 min. As previously mentioned in discussion part 3.2.2, 2 mg TiO<sub>2</sub> nanoparticles and 3 mg PEDOT are found in MNP-PEDOT-TiO<sub>2</sub> composite material and by using 2 mg TiO<sub>2</sub> nanoparticles, only 25 % degradation of MB was achieved in 180 min (Table 3.6). This result also supports the increase in enhancement obtained with a proposed structure. The increase in activity can be attributed to an increase in charge separation process due to doping of TiO<sub>2</sub> nanoparticles with PEDOT besides the increase in surface area of the resulting MNP-PEDOT-TiO<sub>2</sub> composite material.

In order to further increase the catalytic activity under visible light irradiation, MNP-PEDOT-TiO<sub>2</sub> composite material was doped with noble metal nanoparticles. According to the results given in Table 3.6, the addition of noble metal nanoparticles improves the catalytic activity and total degradation of MB under solar light was achieved only in 20 min. In this part, MNP-PEDOT-TiO<sub>2</sub> composite material doped with Ag, Au and AgAu nanoparticles. The comparison of the catalytic activities of MNP-PEDOT-TiO<sub>2</sub> composite material with doped ones is given in Figure 3.35.

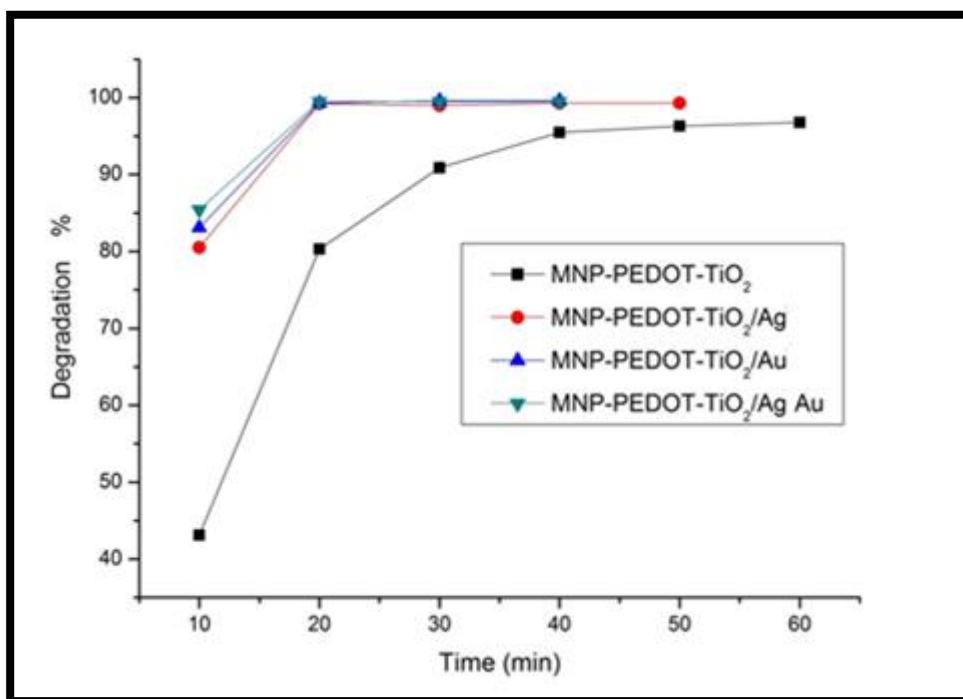


Figure 3.35. Comparison of the percent degradation of MB under solar light by using a) MNP-PEDOT-TiO<sub>2</sub>, b) MNP-PEDOT-TiO<sub>2</sub>-Ag, c) MNP-PEDOT-TiO<sub>2</sub>-Au and d) MNP-PEDOT-TiO<sub>2</sub>-AgAu catalyst.

The highest catalytic activity for MB degradation under solar light was obtained with the doping of TiO<sub>2</sub> nanoparticles with PEDOT and noble metal nanoparticles in the presence of MNP. MB dye solution was totally degraded after 20 min solar light exposure by using MNP-PEDOT-TiO<sub>2</sub>-AuNPs, MNP-PEDOT-TiO<sub>2</sub>-AgNPs and MNP-PEDOT-TiO<sub>2</sub>-AgAuNPs composite materials. Although performing the reaction under solar light (contains only 6% UV light), the catalytic activities of the composite materials much higher than the activities measured under UV light illumination. This increase can be attributed to additional electrons transferred to the conduction band of the semiconductor generated from plasmon excitation process besides the synergetic effects resulting increase in charge separation efficiency obtained with the addition of PEDOT and noble metal nanoparticles to the TiO<sub>2</sub> nanoparticles.

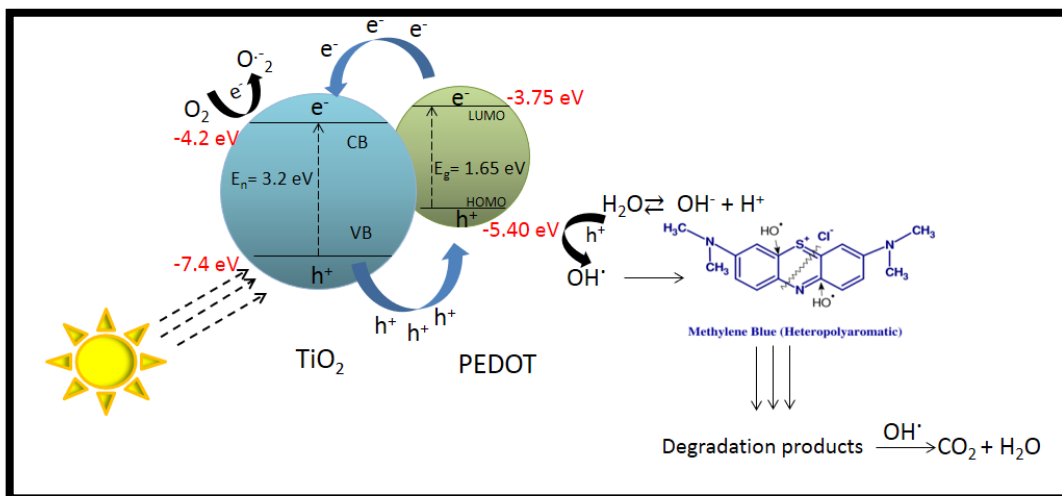
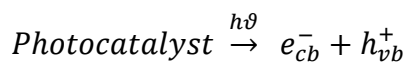
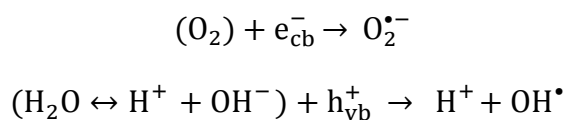


Figure 3.36. Proposed mechanism of photodegradation of MB dye by the prepared photocatalysts under light irradiation..

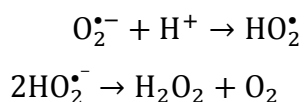
Mainly, the mechanism involves the absorption of photons by photocatalyst with larger energy than that of band gap of photocatalyst.



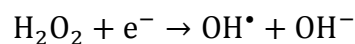
Later on, the reduction of oxygen to superoxide radicals, and neutralization of hydroxyl ions that produces  $\text{OH}\cdot$  radicals are taking place.



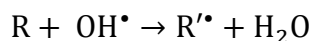
The third step is the neutralization of superoxide radicals by protons following formation of hydrogen peroxide.



The next step is the decomposition of hydrogen peroxide.



And, final steps are the oxidation of reactants by attacks of hydroxyl radicals and by reaction with holes directly.



As the HOMO-LUMO (-5.40 eV, -3.75 eV) levels of PEDOT are well-matched with VB-CB (-7.4 eV, -4.2 eV) levels of TiO<sub>2</sub> nanoparticles, the formed photogenerated e-h pairs can transfer between these levels that results in enhanced charge separation. The better charge separation provides improved photocatalytic activity therefore, the rate of degradation of MB by formed superoxide and hydroxyl radicals to final degradation products (CO<sub>2</sub> and H<sub>2</sub>O) increases. The decrease in time for degradation of dye exhibits the proper synergistic interaction between dopant polymer and TiO<sub>2</sub> as shown in Figure 3.36.

The results obtained were also compared with literature and comparison is given in Table 3.8.

Table 3.8. *The comparison of the results with literature*

Type of Photocatalyst (Concentration)	Concentr. of MB (mg/L)	Year	Removal % (UV)	Removal % (Vis)	Irradiation Time (min)	Ref.
TiO <sub>2</sub> -PVDF/PMMA Blend Membranes (4 cm x 4 cm membranes in 500 mL)	(3.2)	2019	99.0	-	150	[128]
g-C <sub>3</sub> N <sub>4</sub> -RGO-TiO <sub>2</sub> nanoheterojunctions (50 mg catalyst/200 mL MB)	(30)	2017	-	92.0	180	[129]
Mo doped TiO <sub>2</sub> /C-PVA thin films (4 cm/8 mL MB)	(3.2)	2019	90.6	-	1440	[130]
PPy-TiO <sub>2</sub> nanocomposite (20 mg/50 mL MB)	(1)	2017	-	93.0	90	[131]
PoPD/TiO <sub>2</sub> (30 mg/30 mL MB)	(40)	2017	-	Nearly 60.0	180	[132]
Aerochitin-TiO <sub>2</sub> composite (10 mg/10 mL)	(10)	2018	98.0	-	200	[133]
TrCMP-TiO <sub>2</sub> micropous comp. (25 mg/35 mL)	(8)	2018	-	Complete Degr.	60	[134]
BiPO <sub>4</sub> /PANI (200 mg/200 mL)	(20)	2018	95.8	87.3	480 (sunlight) 2 (UV)	[135]
CdS/PTh, CdS/PPy, CdS/PANI (25 mg/50 mL)	(10)	2018	-	71.0, 77.0, 61.0 respectively	300	[136]
ZnO /PMMA powders (100 mg/2 mL)	(10)	2017	60.0	-	240	[137]
MNP-PEDOT-TiO <sub>2</sub> -AgAu (10 mg/10 mL)	(10)	2019	Complete Deg.	Complete Deg.	30 (UV) 20 (SS)	This Study



As shown in Table 3.8, the MNP-PEDOT-TiO<sub>2</sub>-AgAuNPs has the highest photocatalytic activity among the polymer and TiO<sub>2</sub> based catalysts reported in the literature for the same reaction.

#### **3.2.4. Reuse Studies**

To evaluate the photocatalytic stability, reusability of MNP-PEDOT-TiO<sub>2</sub>-AgNPs, MNP-PEDOT-TiO<sub>2</sub>-AuNPs and MNP-PEDOT-TiO<sub>2</sub>-AgAuNPs composites was tested in successive experiments. After the completion of photocatalytic degradation of MB performed under solar light, the catalyst was isolated using a permanent magnet (Figure 3.13) and then dispersed in 10 mL solution containing MB. After that second run of degradation process was started immediately and continued for another 20 min. The photocatalytic degradation process was repeated 5 times under solar light. Since the isolation of catalyst by time-consuming processes like centrifugation and filtration results in catalyst loss after each subsequent runs, magnetically isolable composite materials are highly advantageous. The results are given in Figure 3.37, Figure 3.38 and Figure 3.39, respectively.

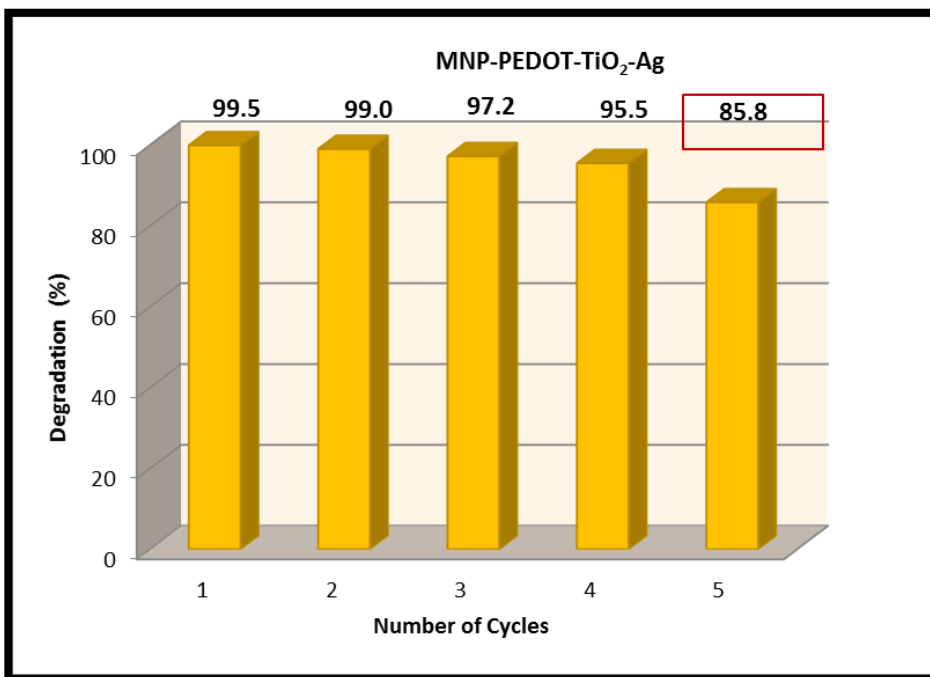


Figure 3.37. Reuse performance of MNP-PEDOT-TiO<sub>2</sub>-AgNPs composite material.

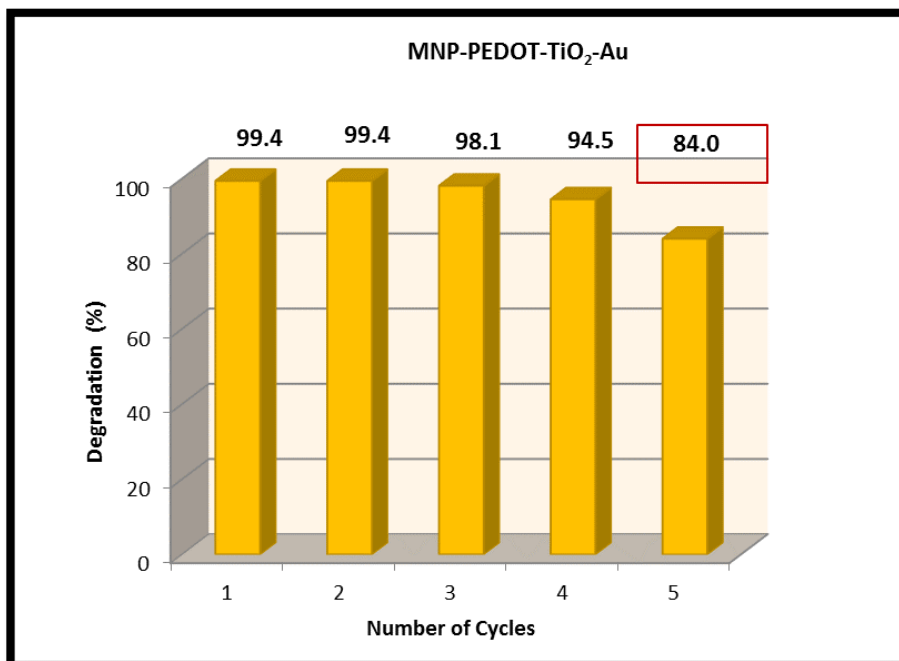


Figure 3.38. Reuse performance of MNP-PEDOT-TiO<sub>2</sub>-AuNPs composite material.

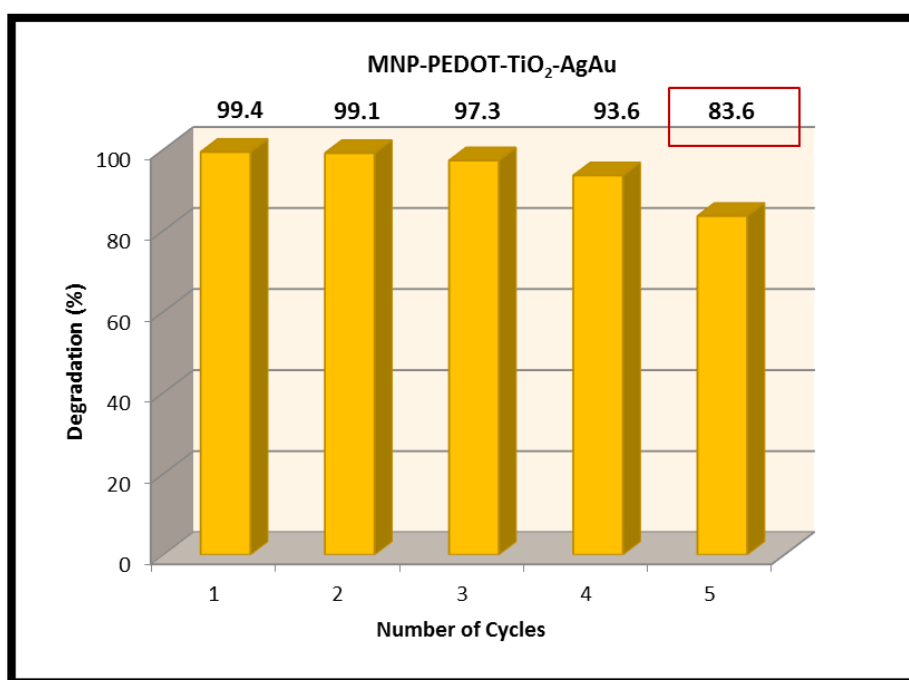


Figure 3.39. Reuse performance of MNP-PEDOT-TiO<sub>2</sub>-AgAuNPs composite material.

As can be seen from the results, after five successive experiments percent degradations decrease from 99.5 % to 84% for all catalysts. The resulting solutions after 5 runs were analyzed by ICP-OES and no leaching of Au and Ag into the solution was detected. Therefore, the slight decrease in the catalytic activity of MNP-PEDOT-TiO<sub>2</sub>-AgNPs, MNP-PEDOT-TiO<sub>2</sub>-AuNPs and MNP-PEDOT-TiO<sub>2</sub>-AgAuNPs composites after the 5th run in photocatalytic degradation of MB under solar light can be attributed to partial oxidation of noble metal nanoparticles found on the structure and deposition of degradation products onto the composites and/or small amount of loss of catalyst during separation. In order to provide complete degradation, a number of washing step can be increased to get rid of the degradation products adsorbed onto the surface of composites. Also, additional reduction step with sodium borohydride can be applied to regenerated catalyst after 3<sup>rd</sup> run or exposure time can be increased.

### **3.3. Measurements of the Degradation Products of Methylene Blue by Using LC-MS**

The photocatalytic degradation process can be followed in two different ways. In the first one, decolorization of dye followed by using UV-Vis spectrometer. But it is difficult to understand whether the removal is caused by photocatalytic degradation or attachment to the surface of the material (adsorption). In order to decide whether the process is degradation or not, the reaction solution must be analyzed with gas (GC) or liquid chromatography (LC) coupled with mass (MS) detector. TiO<sub>2</sub> nanoparticles are considered as the reference total oxidation catalyst in photocatalytic reactions. Thus the data obtained from the usage of TiO<sub>2</sub> nanoparticle for the decomposition of methylene blue was used to prove the photocatalytic decomposition of methylene blue with the usage of prepared composite material under solar light illumination.

In the previous section, dye removal was determined using UV-Vis spectroscopy by following the decolorization. In this part, removal of the MB dye was due to photocatalytic degradation was revealed by LC-MS data. In this direction, initially, the mass spectrum of MB solution was obtained prior to treatment with the catalyst under light irradiation. The corresponding MS data of the methylene blue is given in Figure 3.40.

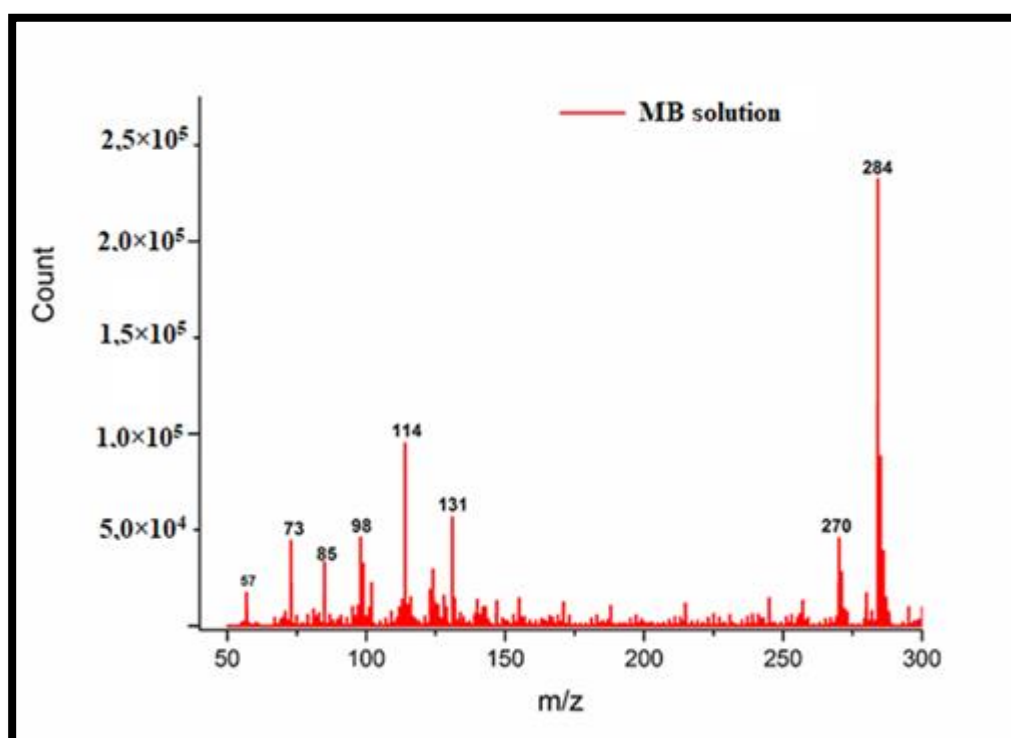


Figure 3.40. LC-MS spectrum of MB before the photocatalytic reaction under solar light.

The line located at  $m/z=284$  is related to parent ion of methylene blue  $[MB + H]^+$ . The other intense line observed at  $m/z= 270$  is related to Azure B known as well-known homologs of MB [ref Hiba 65]. New lines at  $m/z= 131, 114, 98, 85$  and  $73$  are related to fragmentation of MB and/or organic contamination.

Secondly, photocatalytic degradation of MB solution was performed in the presence of  $TiO_2$  nanoparticles as the catalyst under solar light for 120 min. After isolation of catalyst, the solution part was analyzed with LC-MS and the result is given in Figure 3.41.

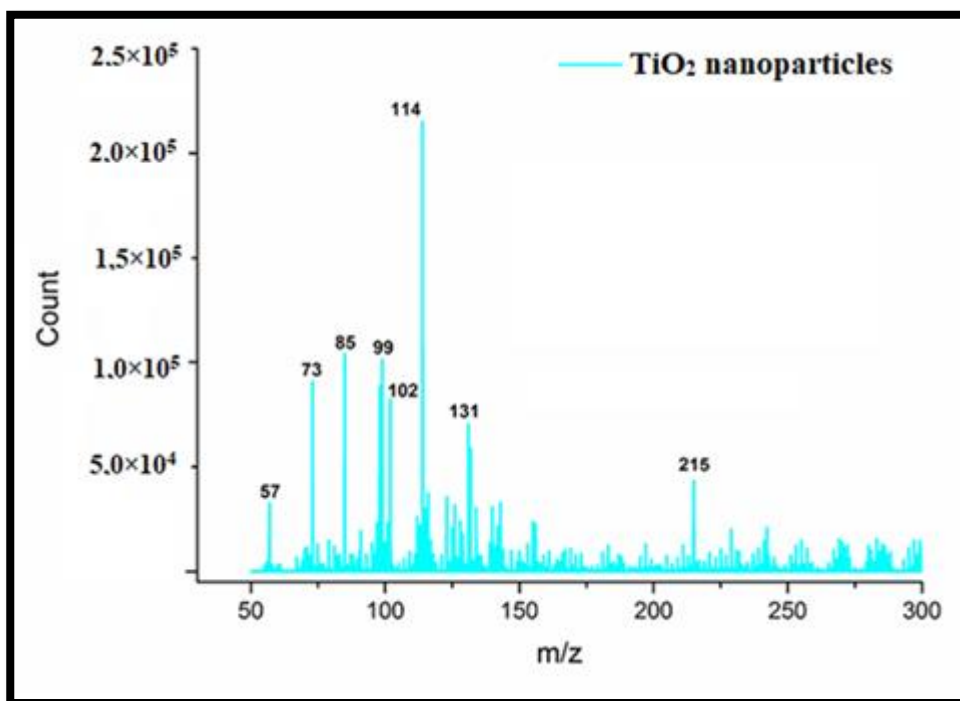


Figure 3.41. LC-MS spectrum of the photocatalytic degradation products of methylene blue by using TiO<sub>2</sub> nanoparticles as catalyst under solar light.

Main signals located at  $m/z= 284$  and  $m/z= 270$  were disappeared after the photocatalytic treatment which is the indication of degradation of MB molecules.

Finally, the MB solution treated with MNP-PEDOT-TiO<sub>2</sub>-AgAuNPs composite material under solar light for 20 min measured with LC-MS. After that, the result is compared with the mass spectra obtained with TiO<sub>2</sub> nanoparticles. The comparison of the LC-MS spectra is given in Figure 3.42.

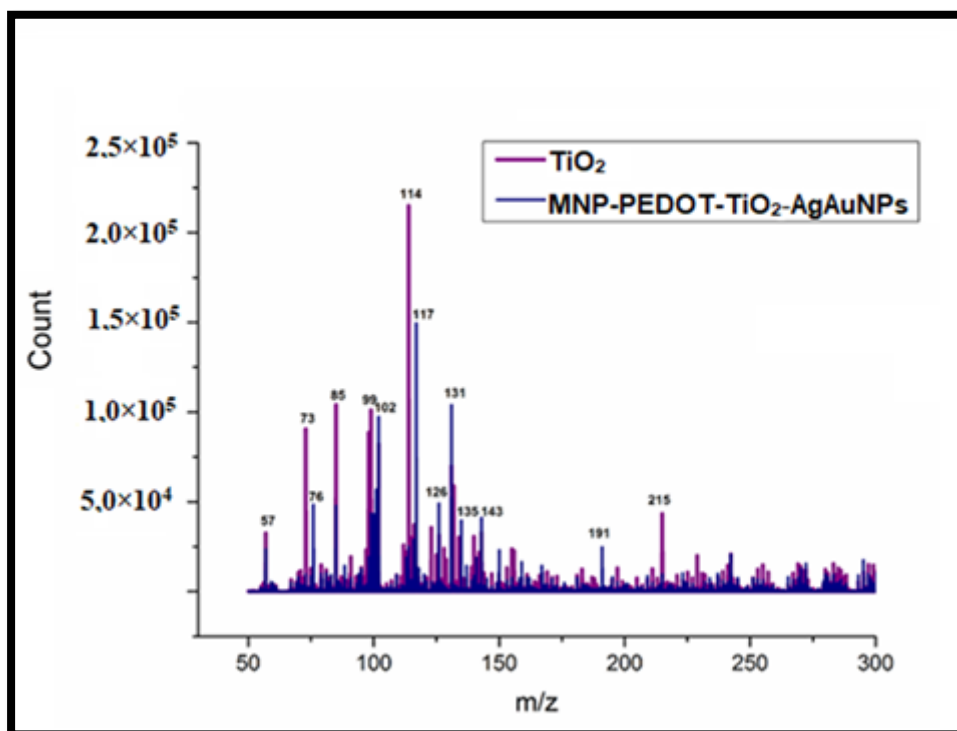


Figure 3.42. Comparison of the LC-MS data of the MB solution treated with TiO<sub>2</sub> nanoparticles and MNP-PEDOT-TiO<sub>2</sub>-AgAuNPs under solar light.

According to Figure 3.42, main lines located at  $m/z=284$  and  $270$  related to parent ion of methylene blue disappeared after treatment with MNP-PEDOT-TiO<sub>2</sub>-AgAuNPs composite material under solar light irradiation. These changes can be considered as the proof of photocatalytic degradation of methylene blue with the usage of prepared composite materials. As can be seen from the MS spectra, there is a decrease in the total amount of methylene blue (Figure 3.42) which can be attributed the decomposition of it into CO<sub>2</sub> and other inorganic ions like nitrate and sulfate besides degradation products and fragments. When the total illumination time of solar light considered (120 min for TiO<sub>2</sub> nanoparticles and 20 min for MNP-PEDOT-TiO<sub>2</sub>-AgAuNPs composite), it is possible to say that the prepared composite material is a much more effective catalyst than TiO<sub>2</sub> nanoparticles. The results of LC-MS

measurements are consistent with the results obtained with UV-Vis spectrometry in decolorization studies.

### **3.4. Photocatalytic Hydrogen Production Studies**

In this part of the thesis, the photocatalytic activity of the prepared composite catalysts was tested in the production of hydrogen gas from the ethanol-water mixture. For this, 50 mL of 10% ethanol solution and 20 mg of catalyst were introduced into the photoreactor as described in the experimental section in all trials. The hydrogen production efficiency of all catalyst prepared under UV light was checked using the quartz reactor system given in the Experimental part (Figure 2.8). The amount of gas obtained during the reaction was monitored by a decrease in liquid level founded in a tube. Then the experiments were repeated and the gas obtained in each experiment was collected in the gas sampling bag (Tedlar bag). After that, the content of the gas collected was revealed by using GC-TCD system in order to find the exact amount of hydrogen gas produced in each try.

Initially, a control experiment was performed by putting 50 mL ethanol-water mixture contains 10% of ethanol into the reactor and UV exposure was started without putting catalyst. Then gas evolution was followed in time. The reaction was continued for 60 min and then ended at the point where the gas formation not observed. The result obtained for the control experiment is given in Figure 3.43.



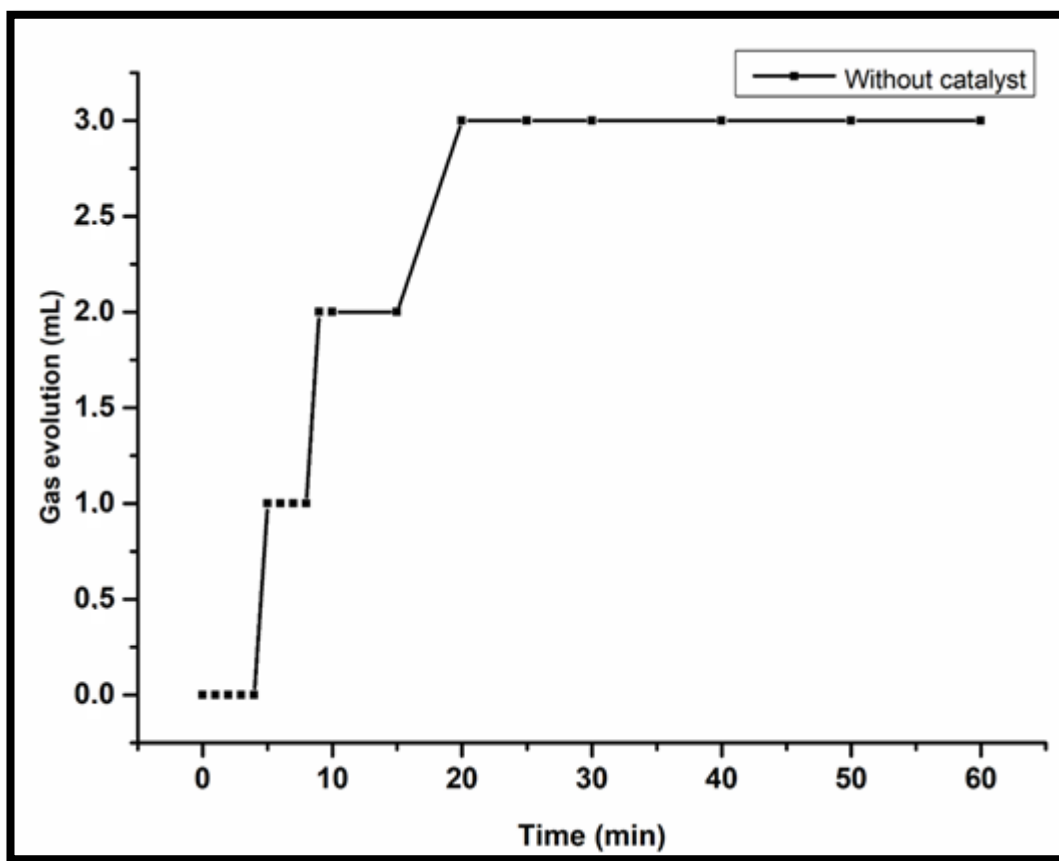


Figure 3.43. Control experiment for photocatalytic hydrogen evolution, a time-dependent variation of the volume of the gas mixture obtained from 50 mL water-ethanol mixture under 150 W UV light exposure in the absence of a catalyst.

As can be seen from Figure 3.43, no appreciable gas formation was observed in the catalyst-free medium. Only 3 mL gas generation was measured at the end of 60 minutes of UV light exposure.

The analysis of the generated gas at the end of the control experiment was carried out by using GC coupled with a TCD detector and no hydrogen detected. Only oxygen and nitrogen gases were observed. The obtained chromatogram is given in Figure 3.44.

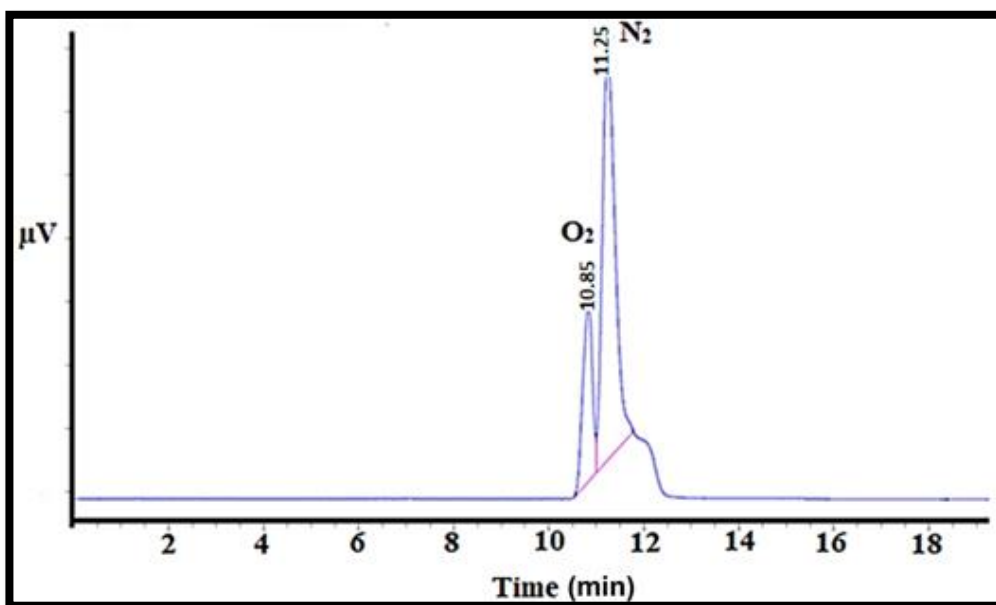


Figure 3.44. GC chromatogram which shows the composition of gas obtained from 50 mL water-ethanol mixture under 150 W UV light exposure at the end of the control experiment.

According to the chromatogram obtained, only peaks related to oxygen (10.85 min) and nitrogen (11.25 min) were observed.

After the control experiment, the hydrogen generation capacity of prepared catalysts was measured respectively with UV light exposure. In the first trials, gas evolution profiles of all catalysts were revealed. After that same experiments were performed and the formed gas collected into the Tedler bag and analyzed by using GC-TCD. Initially, the hydrogen generation capacity of  $\text{TiO}_2$  nanoparticles from the ethanol-water mixture as photocatalyst was determined. The obtained result is given in Figure 3.45.

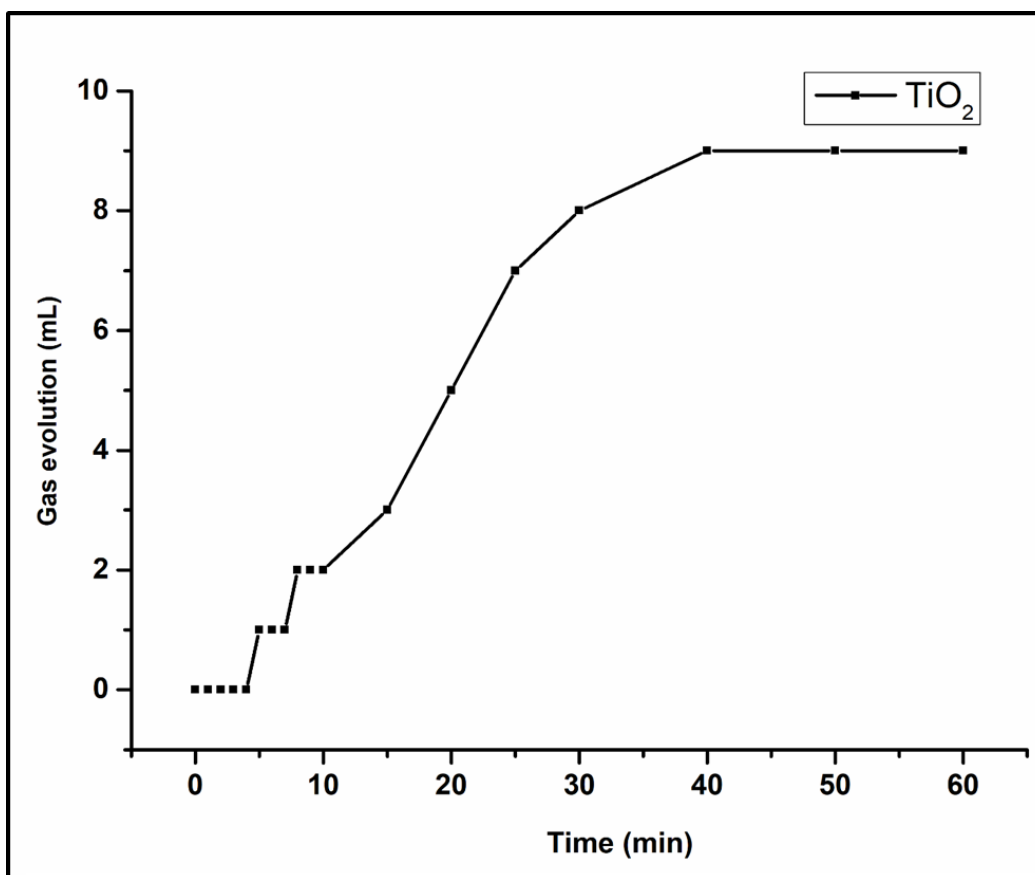


Figure 3.45. Time-dependent variation of the volume of the gas mixture obtained from photocatalytic hydrogen evolution from 50 mL water-ethanol mixture under 150 W UV light exposure by using 20 mg TiO<sub>2</sub> nanoparticles as a catalyst.

9 mL gas evolution was determined at the end of the 40 min UV light exposure by using TiO<sub>2</sub> nanoparticles as the photocatalyst. The reaction was continued for up to 60 minutes. No change in gas volume was observed after 40 minutes. Therefore, the maximum gas evolution was recorded as 9 mL.

Secondly, the photocatalytic activity of MNP-PEDOT in hydrogen generation from the ethanol-water mixture was investigated. For this, the same experimental setup and conditions were used. The result is given in Figure 3.46.

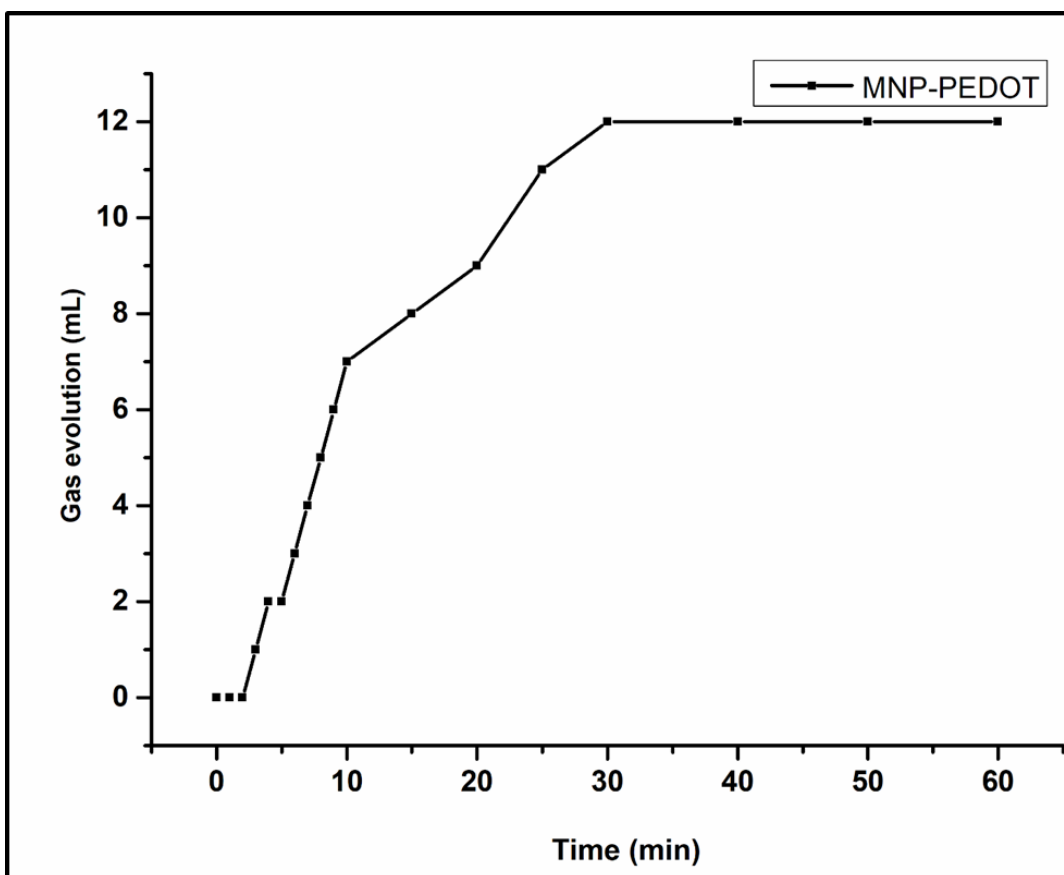


Figure 3.46. Time-dependent variation of the volume of the gas mixture obtained from photocatalytic hydrogen evolution from 50 mL water-ethanol mixture under 150 W UV light exposure by using 20 mg MNP-PEDOT as a catalyst.

According to the result given above, 12 mL gas was evolved after 30 min. At the end of the 60 min exposure, no change was observed in the volume of the gas obtained by using MNP-PEDOT as a catalyst.

Hydrogen generation capacity of the prepared composite materials was investigated respectively after determination of the photocatalytic activity of TiO<sub>2</sub> nanoparticles and MNP-PEDOT in the photocatalytic hydrogen generation from the water-ethanol mixture under UV light exposure.

In this part, initially the photocatalytic activity thus hydrogen generation capability of MNP-PEDOT-TiO<sub>2</sub> composite material was investigated. The result is given in Figure 3.47.

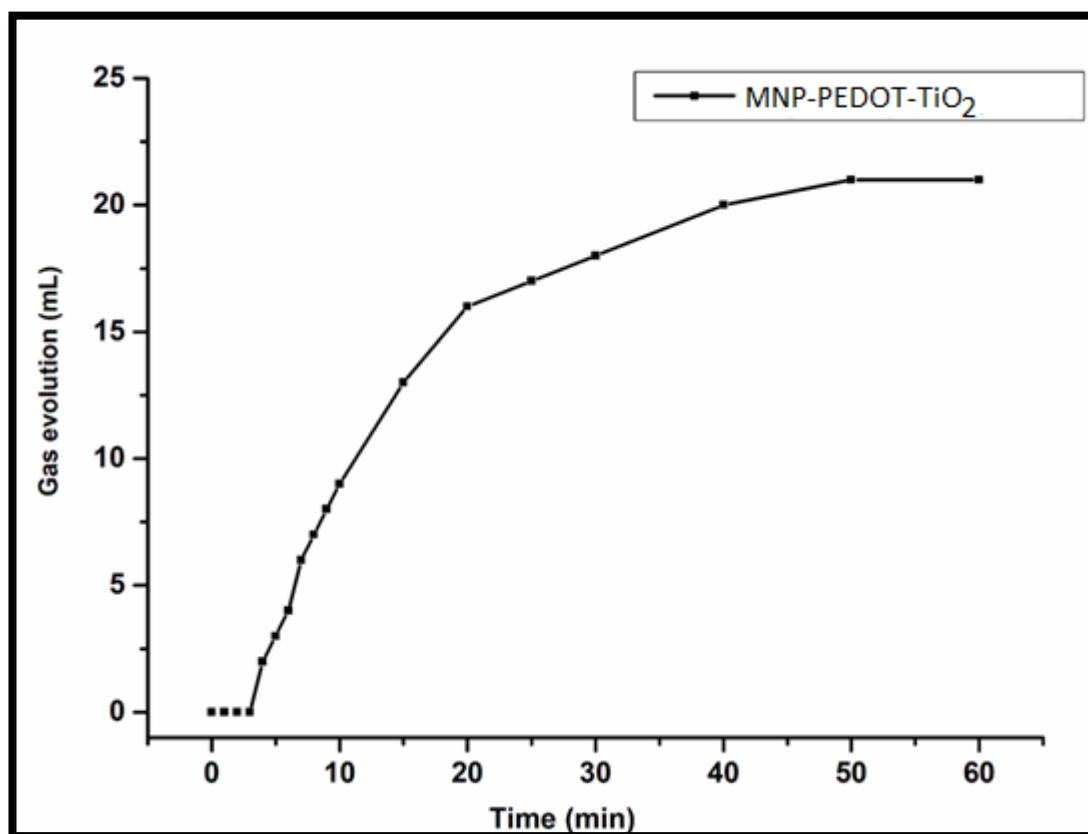


Figure 3.47. Time-dependent variation of the volume of the gas mixture obtained from photocatalytic hydrogen evolution from 50 mL water-ethanol mixture under 150 W UV light exposure by using 20 mg MNP-PEDOT-TiO<sub>2</sub> as a catalyst.

According to Figure 3.47, 22 mL gas generation was obtained at the end of the 50 min UV light exposure. The reaction was ended at 60 min and no increase was detected at the gas level. Although the amount of TiO<sub>2</sub> nanoparticles decreases from 20 mg to 4 mg and PEDOT from 20 mg to 6 mg (20 mg MNP-PEDOT-TiO<sub>2</sub> composite contains nearly 4 mg TiO<sub>2</sub> nanoparticles and 6 mg PEDOT), the volume of gas generated was

increased to 21 mL (9 mL for TiO<sub>2</sub> nanoparticles and 12 mL for PEDOT). From the result obtained, it can be concluded that doping of TiO<sub>2</sub> nanoparticles with PEDOT increased the activity and resulting MNP-PEDOT-TiO<sub>2</sub> composite material showed enhanced activity in photocatalytic hydrogen generation studies under UV light exposure.

After that hydrogen generation performance of the MNP-PEDOT-TiO<sub>2</sub> composite material doped with AgNPs, AuNPs and AgAuNPs were investigated and obtained results were given below respectively. Studies were started by measuring the activity of the MNP-PEDOT-TiO<sub>2</sub>/AgNPs composite material as a catalyst in the photocatalytic hydrogen generation from the water-ethanol mixture. The obtained result is given in Figure 3.48.

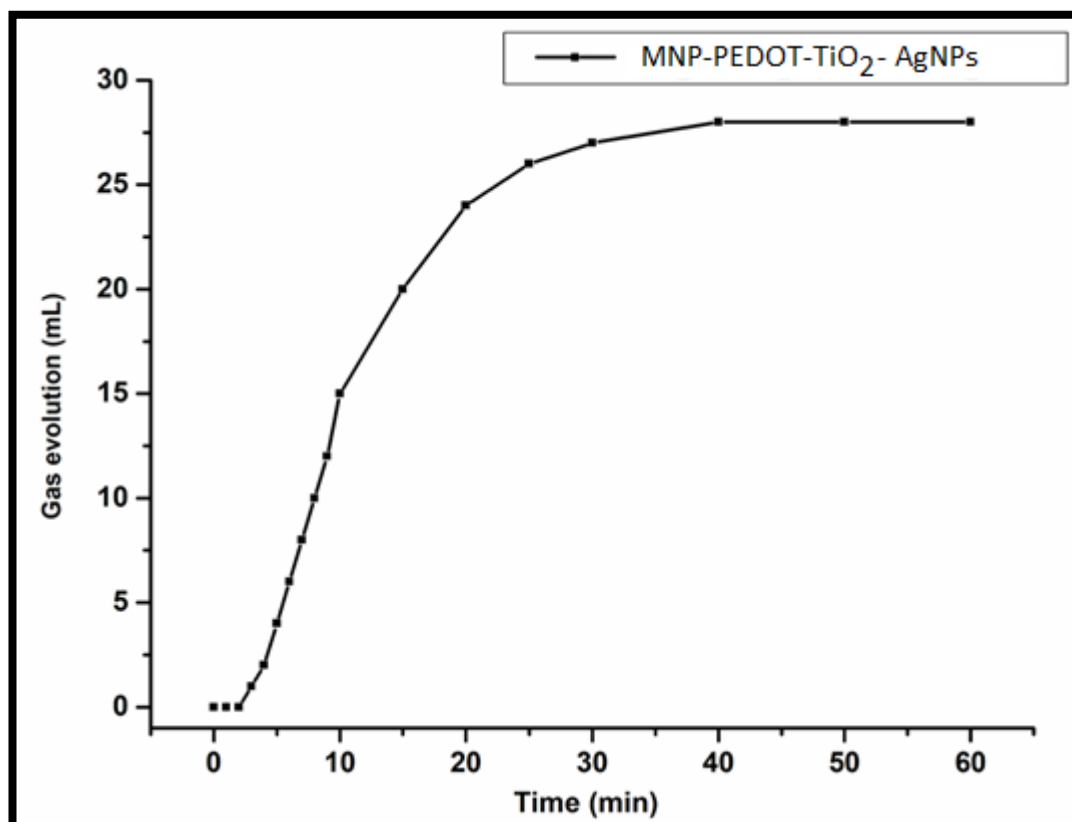
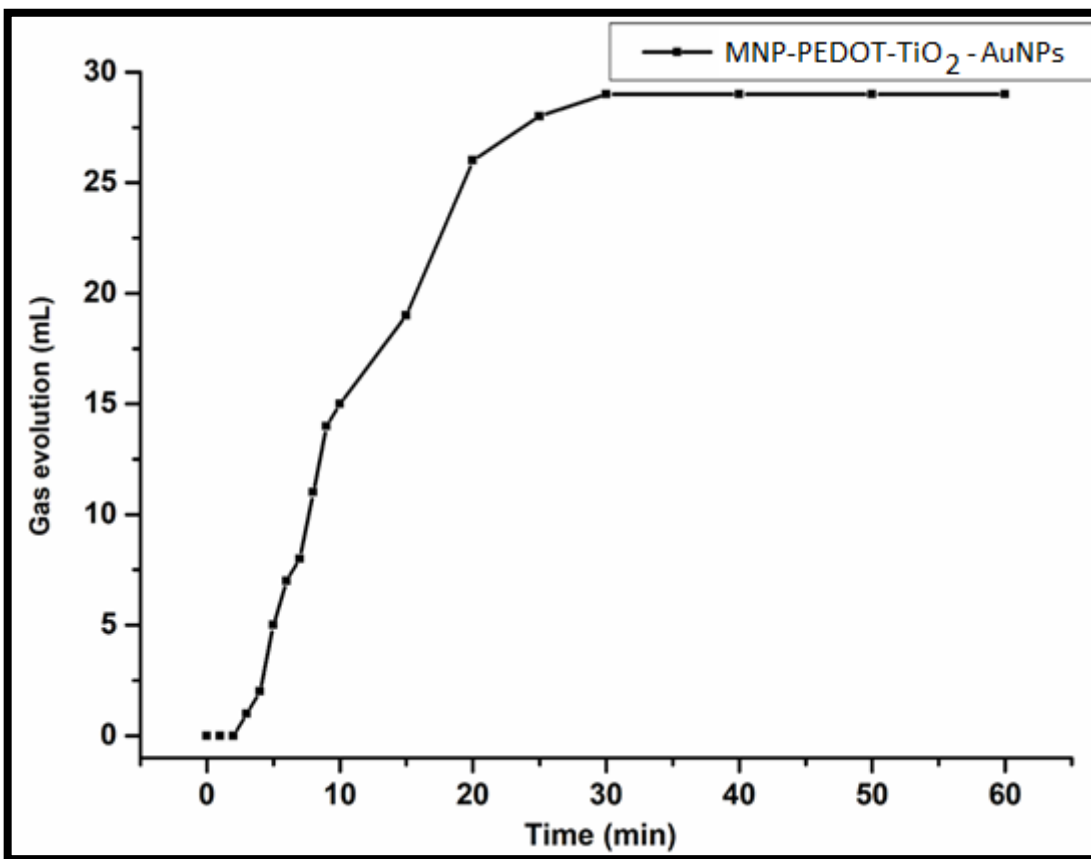


Figure 3.48. Time-dependent variation of the volume of the gas mixture obtained from photocatalytic hydrogen evolution from 50 mL water-ethanol mixture under 150 W UV light exposure by using 20 mg MNP-PEDOT-TiO<sub>2</sub>-AgNPs as a catalyst which contains 0.86 % (w/w), Ag.

According to the result obtained, the gas evolution was increased to 28 mL under 40 min of UV light exposure. The increase in the volume of the generated gas at the end of the photocatalytic process can be considered as the evidence of the effect of the metal nanoparticles doping of the MNP-PEDOT-TiO<sub>2</sub> composite material.

After that MNP-PEDOT-TiO<sub>2</sub> composite material was doped with Au and AgAu (bimetallic) nanoparticles and then used as a photocatalyst in the production of hydrogen gas. The results are given in Figure 3.49 and Figure 3.50, respectively.



*Figure 3.49.* Time-dependent variation of the volume of the gas mixture obtained from photocatalytic hydrogen evolution from 50 mL water-ethanol mixture under 150 W UV light exposure by using 20 mg MNP-PEDOT-TiO<sub>2</sub>-AuNPs as a catalyst which contains 0.32 % (w/w), Au.



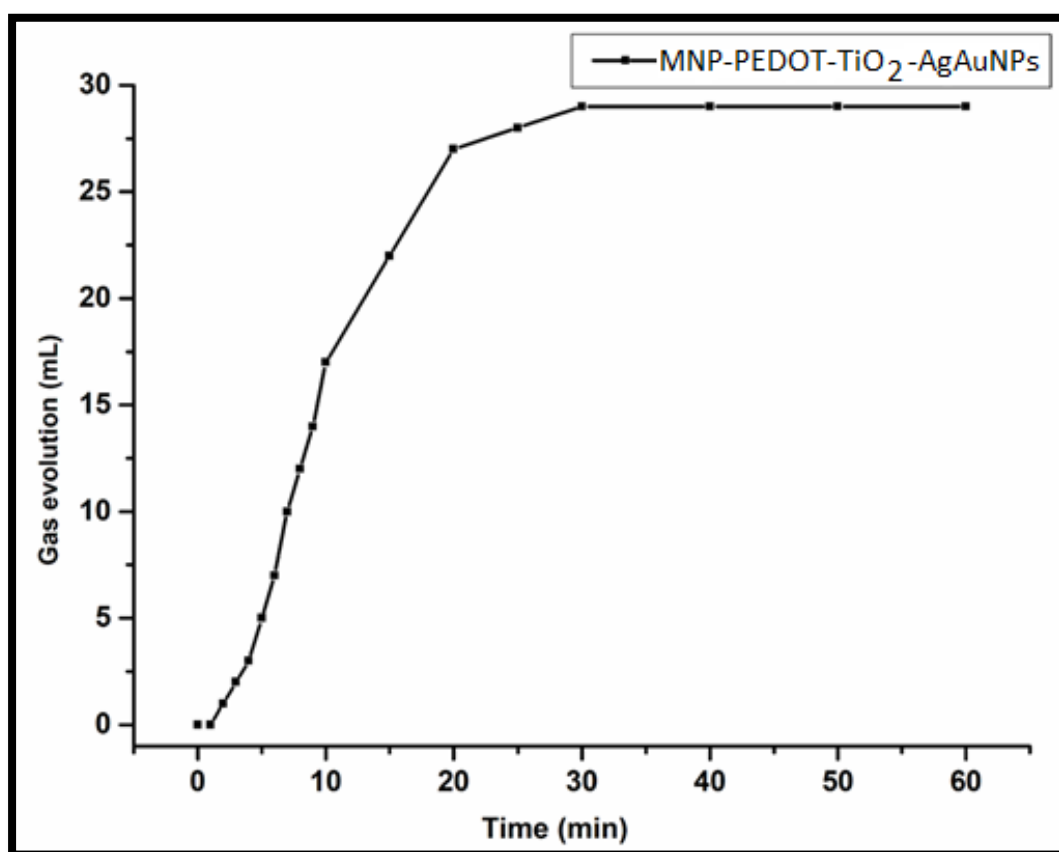


Figure 3.50. Time-dependent variation of the volume of the gas mixture obtained from photocatalytic hydrogen evolution from 50 mL water-ethanol mixture under 150 W UV light exposure by using 20 mg MNP-PEDOT-TiO<sub>2</sub>-AgAuNPs as a catalyst which contains 0.79 % (w/w) Ag and 0.28 % (w/w) Au.

According to the result 29 mL and 28 mL gas evolved by using MNP-PEDOT-TiO<sub>2</sub>-AuNPs and MNP-PEDOT-TiO<sub>2</sub>-AgAuNPs as a catalyst, respectively. The increase in the activity also observed with the addition of Au and AgAu nanoparticles to the MNP-PEDOT-TiO<sub>2</sub> composite material. In order to make the comparison, all results obtained are given in Figure 3.51.

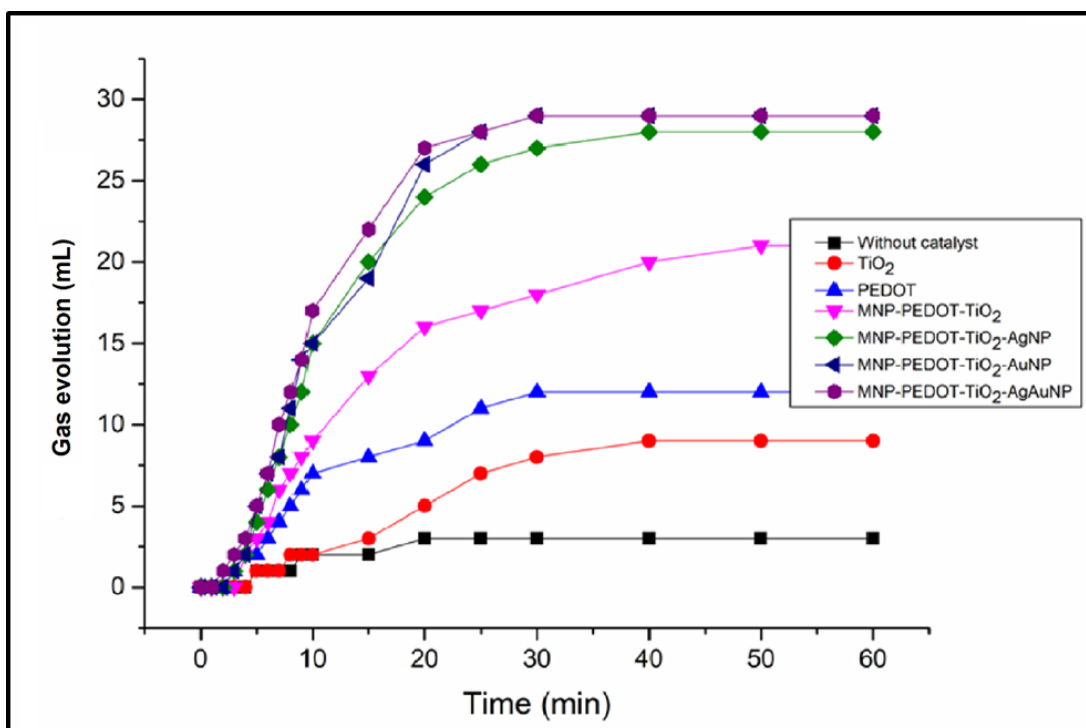
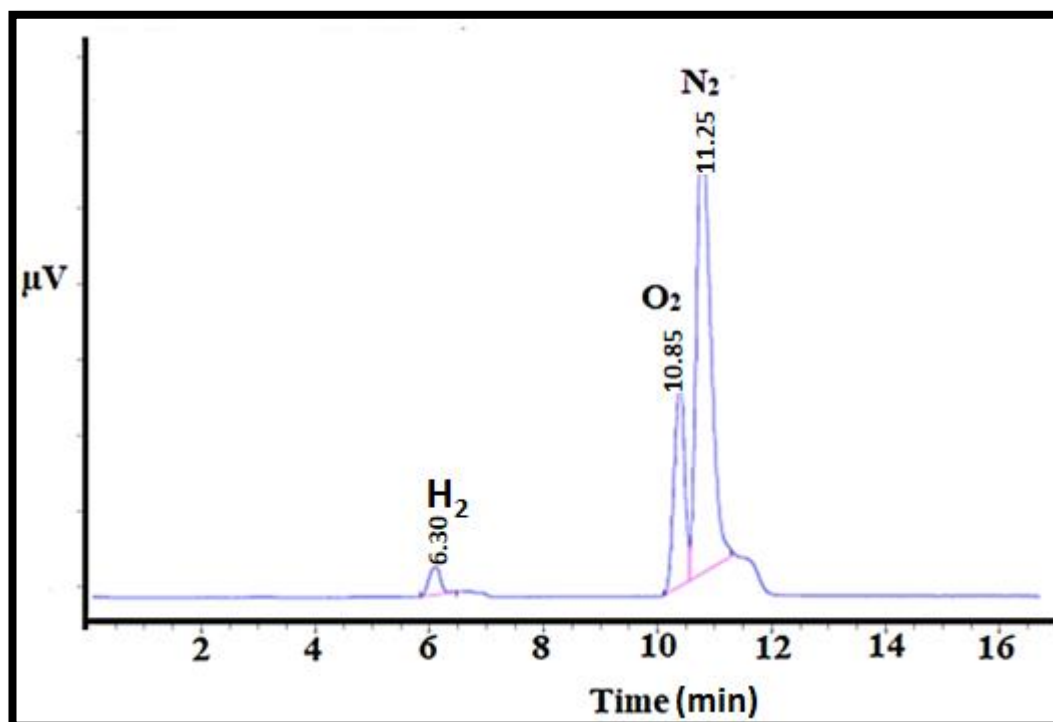


Figure 3.51. Comparison of the gas formation capability of catalysts prepared during this study.

The highest gas generation activity was obtained with the usage of MNP-PEDOT-TiO<sub>2</sub>-AuNPs and MNP-PEDOT-TiO<sub>2</sub>-AgAuNPs as the photocatalyst. It was observed that the results obtained for gas generation studies were consistent with the results obtained for the decomposition of MB under both UV and solar light illumination.

Accordingly, the doping of TiO<sub>2</sub> nanoparticles with polymer and metallic nanoparticles in the presence of magnetic nanoparticles increased the photocatalytic activity. After that, the amount of hydrogen gas found in the gas generated at the end of the photocatalytic reaction was revealed with GC-TCD measurements. The example of the chromatogram obtained for each experiment is given in Figure 3.52.



*Figure 3.52.* GC chromatogram showing the composition of gas obtained from 50 mL water-ethanol mixture by using MNP-PEDOT-TiO<sub>2</sub> composite material as photocatalyst under 150 W UV light exposure.

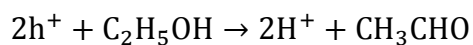
In addition to N<sub>2</sub> and O<sub>2</sub>, H<sub>2</sub> peak was observed at 6.3 min from the chromatogram. The amount of hydrogen was calculated from the peak area and results are given in Table 3.9.

Table 3.9. Comparison of the hydrogen amounts obtained by using photocatalyst produced during the study.

Sample	The volume of the obtained gas mixture	% Hydrogen amount by GC-TCD	The volume of Hydrogen (mL)	Temperature measured at the end of the reaction (K)	Hydrogen amount (mol)
<b>Control Experiment (without catalyst)</b>	3	0	0	305	0
<b>TiO<sub>2</sub></b>	9	1.6	0.14	304	$5.61 \times 10^{-6}$
<b>MNP-PEDOT</b>	12	1.5	0.18	307	$7.20 \times 10^{-6}$
<b>MNP-PEDOT-TiO<sub>2</sub></b>	21	3.2	0.67	308	$2.65 \times 10^{-5}$
<b>MNP-PEDOT-TiO<sub>2</sub>-AgNPs</b>	28	3.5	0.98	308	$3.88 \times 10^{-5}$
<b>MNP-PEDOT-TiO<sub>2</sub>-AuNPs</b>	29	3.5	1.02	307	$4.05 \times 10^{-5}$
<b>MNP-PEDOT-TiO<sub>2</sub>-AgAuNPs</b>	29	3.6	1.04	308	$4.13 \times 10^{-5}$

According to the results given in Table 3.9, the highest amount of hydrogen gas was obtained by using MNP-PEDOT-TiO<sub>2</sub>-AuNPs and MNP-PEDOT-TiO<sub>2</sub>-AgAuNPs composite materials as the photocatalyst under UV light illumination.

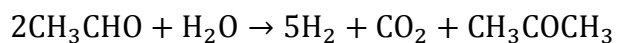
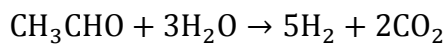
As reported before, after the e-h pairs formation by light irradiation in the photocatalyst, ethanol is oxidized to acetaldehyde via holes.



Secondly, electrons are trapped on the surface, where they reduce and recombine protons to produce H<sub>2</sub> gas as follows:



Furthermore, in the presence of water, acetaldehyde can additionally form hydrogen gas according to following reactions.





## CHAPTER 4

### CONCLUSION

Semiconductor metal oxide based photocatalytic materials have gained great importance for degradation of pollutants in wastewater. Among the semiconductor based photocatalysts, TiO<sub>2</sub> has attracted attention in the wastewater and air purification due to its low-cost, efficiency, and non-toxicity. Unfortunately, low catalytic activity under visible light and separation of small sized photocatalyst materials from large volumes of wastewater considered as the main drawbacks.

In this thesis, in order to increase the photocatalytic activity, and provide separation of catalyst without the need for complex processes (filtration, centrifugation, etc.) for reuse study and to eliminate secondary pollution caused by catalyst, composite materials which contains PEDOT, TiO<sub>2</sub> nanoparticles, noble metal and magnetic nanoparticles were prepared and their catalytic activities were investigated in the photocatalytic degradation of MB and hydrogen generation from water-ethanol mixture under UV and solar light.

Detailed characterization of the prepared materials was carried out by using advanced analytical methods. The catalytic activities of the obtained catalysts were tested in the photocatalytic degradation of MB under UV and solar light. The highest activity was obtained with the use of MNP-PEDOT-TiO<sub>2</sub>-AuNPs and MNP-PEDOT-TiO<sub>2</sub>-AgAuNPs composite structures. Under solar light, only 20 minute is enough to achieve complete degradation of methylene blue by using these composite materials. Besides, the determination of degradation products was carried out by using LC-MS to prove photocatalytic degradation. In addition, the hydrogen generation capacity of the photocatalysts from ethanol-water mixture was also investigated. The amount of

hydrogen generated was calculated with GC-TCD measurements. The highest hydrogen generation was obtained with MNP-PEDOT-TiO<sub>2</sub>-AgAuNPs composite material.

According to the results obtained, it has been shown that the efficiency of TiO<sub>2</sub> nanoparticles can be increased with the addition of conductive polymers and metal nanoparticles and, therefore it is possible to ensure their effectiveness in the visible light region. The prepared photocatalysts are proper candidates to remove toxic dyes finding in textile wastewaters and to generate hydrogen from volatile organic compounds. The obtained results are also shown that the idea of doping titanium dioxide nanoparticles together with PEDOT and metal nanoparticles is the right strategy for increasing the activity under UV light and providing high activity under visible light.



## REFERENCES

- [1] Shahzad, U. The need for renewable energy sources. *ITEE Journal*, 16-18. (2015).
- [2] Akhter Hossain, K. Present and future of global energy sources. *J. Fundam. Renewable Energy Appl.* **5**, 1-7 (2015).
- [3] Alpern, B., & Lemos de Sousa, M. J. Documented international enquiry on solid sedimentary fossil fuels; coal: definitions, classifications, reserves-resources, and energy potential. *Int. J. Coal Geol.* **50**, 3-41 (2002).
- [4] Hill, J., Nelson, E., Tilman, D., Polasky, S., & Tiffany, D. Environmental, economic, and energetic costs and benefits of biodiesel and ethanol biofuels. *P. Natl. Acad. Sci.* **103**, 11206-11210 (2006).
- [5] Bengtsson, S., Andersson, K., & Fridell, E. A comparative life cycle assessment of marine fuels: liquefied natural gas and three other fossil fuels. *P. I. Mech. Eng. M-J Eng.* **225**, 97-110 (2011).
- [6] Khoo, H., & Tan B. H. R. Environmental impact evaluation of conventional fossil fuel production (oil and natural gas) and enhanced resource recovery with potential CO<sub>2</sub> sequestration. *Energy & Fuels* **20**, 1914-1924 (2006).
- [7] Panwar, N. L., Kaushik, S. C., & Kothari, S. Role of renewable energy sources in environmental protection: A review. *Renew. Sust. Energ. Rev.* **15**, 1513-1524 (2011).
- [8] Adewuyi, A. O., & Awodumi, O. B. Renewable and non-renewable energy-growth-emissions linkages: Review of emerging trends with policy implications. *Renew. Sust. Energ Rev.* **69**, 275-291 (2017).
- [9] Nadimi, R., & Tokimatsu, K. Analyzing of renewable and non-renewable energy consumption via bayesian inference. *Enrgy. Proced.* **142**, 2773-2778 (2017).

- [10] Dincer, I., & Acar, C. A review on clean energy solutions for better sustainability. *Int. J. Energ. Res.* **39**, 585-606 (2015).
- [11] Owusu, P., & Asumadu-Sarkodie, S. A review of renewable energy sources, sustainability issues and climate change mitigation, *Cogent Eng.* **3**, 1-14 (2016).
- [12] Dincer, I. Technical, environmental and exergetic aspects of hydrogen energy systems. *Int J Hydrogen Energy* **27**, 265-285 (2002).
- [13] Ma, Y., Wang, X., Jia, Y., Chen, X., Han, H., & Li, C. Titanium dioxide-based nanomaterials for photocatalytic fuel generations. *Chem. Rev.* **114**, 9987-10043 (2014).
- [14] Idriss, H., Scott, M., Llorca, J., Chan, S. C., Chiu, W., Sheng, P. Y., Yee, A., Blackford, M. A., Pas, S. J., Hill, A. J., Alamgir, F. M., Rettew, R., Petersburg, C., Senanayake, S. D. & Barteau, M. A. A phenomenological study of the metal-oxide interface: the role of catalysis in hydrogen production from renewable resources. *ChemSusChem* **1**, 905-910 (2008).
- [15] Czernik, S., Evans, R., & French, R. Hydrogen from biomass-production by steam reforming of biomass pyrolysis oil. *Catal. Today* **129**, 265-268 (2007).
- [16] Santos, D. M. F., Sequeira, C. A. C., & Figueiredo, J. L. Hydrogen production by alkaline water electrolysis. *Quím. Nova* **36**, 1176-1193 (2013).
- [17] Panwar, N. L., Kaushik, S. C., & Kothari, S. Role of renewable energy sources in environmental protection: A review. *Renew. and Sust. Energ. Rev.* **15**, 1513-1524 (2011).
- [18] Edwards, P. P., Kuznetsov, V. L., & David, W. I. F. Hydrogen energy. *Phil. Trans. R. Soc. A: Math., Phys. and Eng. Sci.* **365**, 1043-1056 (2007).
- [19] Fujishima, A., & Honda, K. Electrochemical photolysis of water at a semiconductor electrode. *Nature* **238**, 37-38 (1972).

- [20] Mao, S. S., & Chen, X. Selected nanotechnologies for renewable energy applications. *Int. J. of Energ Res.* **31**, 619-636 (2007).
- [21] Singh, R., & Dutta, S. A review on H<sub>2</sub> production through photocatalytic reactions using TiO<sub>2</sub>/TiO<sub>2</sub>-assisted catalysts. *Fuel* **220**, 607-620 (2018).
- [22] Ismail, A. A., & Bahnemann, D. W. Photochemical splitting of water for hydrogen production by photocatalysis: A review. *Sol. Energy Mater. Sol. Cells* **128**, 85-101 (2014).
- [23] Kuvarega, A. T., Krause, R. W. M., & Mamba, B. B. Evaluation of the simulated solar light photocatalytic activity of N, Ir co-doped TiO<sub>2</sub> for organic dye removal from water. *Appl. Surf. Sci.* **329**, 127-136 (2015).
- [24] Tufekci, N., Sivri, N., & Toroz, I. Pollutants of textile industry wastewater and assessment of its discharge limits by water quality standards, *Turk. J. Fish. Aquat. Sci.* **7**, 97-103 (2007).
- [25] Hao O., Kim H., & Chiang P.-C. Decolorization of wastewater. *Crit. Rev. Environ. Sci. Technol.* **30**, 449-505 (2000).
- [26] Robinson, T., McMullan, G., Marchant, R., & Nigam, P. Remediation of dyes in textile effluent: a critical review on current treatment technologies with a proposed alternative. *Bioresour. Technol.*, **77**, 247-255 (2001).
- [27] Joshi, M., Bansal, R., & Purwar, R. Colour removal from textile effluents. *Indian J. Fibre Text Res.* **29**, 239-259 (2004).
- [28] H. Glaze, W., Kang, J.-W., & H. Chapin, D. The chemistry of water treatment processes involving ozone, hydrogen peroxide and ultraviolet radiation. *Ozone-sci Eng.* **9**, 335-352 (1987).
- [29] Herrmann, J.-M. Heterogeneous photocatalysis: fundamentals and applications to the removal of various types of aqueous pollutants. *Catal. Today* **53**, 115-129 (1999).

- [30] Gogate, P. R., & Pandit, A. B. A review of imperative technologies for wastewater treatment I: oxidation technologies at ambient conditions. *Adv. Environ. Res.* **8**, 501-551 (2004).
- [31] Walling, C. Intermediates in the reactions of fenton type reagents. *Acc. Chem. Res.* **31**, 155-157 (1998).
- [32] Lindsey, M. E., & Tarr, M. A. Quantitation of hydroxyl radical during fenton oxidation following a single addition of iron and peroxide. *Chemosphere* **41**, 409-417 (2000).
- [33] Bautista, P., Mohedano, A. F., Casas, J. A., Zazo, J. A., & Rodriguez, J. J. An overview of the application of fenton oxidation to industrial wastewaters treatment. *J. Chem. Technol. & Biotechnol.*, **83**, 1323-1338 (2008).
- [34] Trabelsi, F., Aït-Lyazidi, H., Ratsimba, B., Wilhelm, A. M., Delmas, H., Fabre, P. L., & Berlan, J. Oxidation of phenol in wastewater by sonoelectrochemistry. *Chem. Eng. Sci.* **51**, 1857-1865 (1996).
- [35] Ma, Y. S. Short review: Current trends and future challenges in the application of sono-fenton oxidation for wastewater treatment. *Sustain. Environ. Res.* **22**, 271-278 (2012).
- [36] Sirés, I., & Brillas, E. Remediation of water pollution caused by pharmaceutical residues based on electrochemical separation and degradation technologies: A review. *Environ. Int.* **40**, 212-229 (2012).
- [37] Hernandez, R., Zappi, M., Colucci, J., & Jones, R. Comparing the performance of various advanced oxidation processes for treatment of acetone contaminated water. *J. Hazard Mater.* **92**, 33-50 (2002).
- [38] Collivignarelli, M. C., Pedrazzani, R., Sorlini, S., Abbà, A., & Bertanza, G. (2017). H<sub>2</sub>O<sub>2</sub> based oxidation processes for the treatment of real high strength aqueous wastes. *Sustainability* **9**, 1-14 (2017).

- [39] Suzuki, H., Araki, S., & Yamamoto, H. Evaluation of advanced oxidation processes (AOP) using O<sub>3</sub>, UV, and TiO<sub>2</sub> for the degradation of phenol in water. *J. Water Process Eng.*, **7**, 54-60 (2015).
- [40] Saghafinia, M. S., Emadian, S. M., & Vossoughi, M. Performances evaluation of photo-fenton process and sonolysis for the treatment of penicillin G formulation effluent. *Procedia Environ. Sci.* **8**, 202-208 (2011).
- [41] Rahim Pouran, S., Abdul Aziz, A. R., & Wan Daud, W. M. A. Review on the main advances in photo-Fenton oxidation system for recalcitrant wastewaters. *J. Ind. Eng. Chem.* **21**, 53-69 (2015).
- [42] Foteinis, S., Monteagudo, J. M., Durán, A., & Chatzisyneon, E. Environmental sustainability of the solar photo-fenton process for wastewater treatment and pharmaceuticals mineralization at semi-industrial scale. *Sci. Total Environ.* **612**, 605-612 (2018).
- [43] Fujishima, A., & Honda, K. Electrochemical photolysis of water at a semiconductor electrode. *Nature* **238**, 37-38 (1972).
- [44] Shon, H. K., Phuntsho, S., Okour, Y. H., Cho, D. L., Kim, K. S., Li, H. J., Na, S., Kim, B.-J & Kim, J.-H. Visible light responsive titanium dioxide (TiO<sub>2</sub>). *J. Korean Ind. Eng. Chem.* **19**, 1-16 (2008).
- [45] Oturan, M. A., & Aaron, J.-J. Advanced oxidation processes in water/wastewater treatment: principles and applications. A Review. *Crit. Rev. Env. Sci Tec.* **44**, 2577-2641 (2014).
- [46] Hashimoto, K., Irie, H., & Fujishima, A. TiO<sub>2</sub> Photocatalysis: a historical overview and future prospects. *Jpn. J. Appl. Phys.* **44**, 8269-8285 (2005).
- [47] Giannakis, S., Rtimi, S., & Pulgarin, C. Light-Assisted advanced oxidation processes for the elimination of chemical and microbiological pollution of wastewaters in developed and developing countries. *Molecules* **22**, 1-20 (2017).

- [48] Pelaez, M., Nolan, N. T., Pillai, S. C., Seery, M. K., Falaras, P., Kontos, A. G., Dunlop, P. S. M., Hamilton, J. W. J., Byrne, J. A., O'Shea, K., Entezari, M. H., Dionysiou, D. D. A review on the visible light active titanium dioxide photocatalysts for environmental applications. *Appl. Catal. B: Environ.* **125**, 331-349 (2012).
- [49] Mills, A., & Le Hunte, S. An overview of semiconductor photocatalysis. *J. of Photoch. Photobio. A: Chem.* **108**, 1-35 (1997).
- [50] Lin, F., Zhang, Y., Wang, L., Zhang, Y., Wang, D., Yang, M., Yang, J., Zhang, B., Jiang, Z., & Li, C. Highly efficient photocatalytic oxidation of sulfur-containing organic compounds and dyes on TiO<sub>2</sub> with dual cocatalysts Pt and RuO<sub>2</sub>. *Appl. Catal. B: Environ.* **127**, 363-370 (2012).
- [51] Yang, X., & Wang, D. Photocatalysis: from fundamental principles to materials and applications. *ACS Appl. Energy Mater.* **1**, 6657-6693 (2018).
- [52] Schultz, D. M., & Yoon, T. P. Solar synthesis: prospects in visible light photocatalysis. *Science* **343**, 1239176-1-8 (2014).
- [53] Yan, H., Wang, X., Yao, M., & Yao, X. Band structure design of semiconductors for enhanced photocatalytic activity: The case of TiO<sub>2</sub>. *Prog. Nat. Sci. Mater.* **23**, 402-407 (2013).
- [54] Huang, C., Li, X.-B., Tung, C.-H., & Wu, L.-Z. Photocatalysis with quantum dots and visible light for effective organic synthesis. *Chem. Eur. J.* **24**, 11530-11534 (2018).
- [55] Luo, B., Liu, G., & Wang, L. Recent advances in 2D materials for photocatalysis. *Nanoscale* **8**, 6904-6920 (2016).
- [56] Wang, P., Huang, B., Dai, Y., & Whangbo, M.-H. Plasmonic photocatalysts: Harvesting visible light with noble metal nanoparticles *Phys. Chem. Chem. Phys.* **14**, 9813-9825 (2012).

- [57] Lia, J. & Wu, N. Semiconductor-based photocatalysts and photoelectrochemical cells for solar fuel generation: a review. *Catal. Sci. Technol.* **5**, 1360-1384 (2015).
- [58] Djurišić, A. B., Leung, Y. H., & Ng, A. M. C. Strategies for improving the efficiency of semiconductor metal oxide photocatalysis. *Mater. Horiz.* **1**, 400-410 (2014).
- [59] Chatterjee, D., & Dasgupta, S. Visible light induced photocatalytic degradation of organic pollutants. *J. Photoch. Photobio. C: Photoch. Rev.* **6**, 186-205 (2005).
- [60] Gunti, S., Kumar, A., & Ram, M. K. Nanostructured photocatalysis in the visible spectrum for the decontamination of air and water. *Int. Mater. Rev.* **63**, 257-282 (2018).
- [61] Mantzila, A. G., & Prodromidis, M. I. Development and study of anodic Ti/TiO<sub>2</sub> electrodes and their potential use as impedimetric immunosensors. *Electrochim. Acta* **51**, 3537-3542 (2006).
- [62] Wang, S., Lian, J. S., Zheng, W. T., & Jiang, Q. Photocatalytic property of Fe doped anatase and rutile TiO<sub>2</sub> nanocrystal particles prepared by sol-gel technique. *Appl. Surf. Sci.* **263**, 260-265 (2012).
- [63] Xie, M., Jing, L., Zhou, J., Lin, J., & Fu, H. Synthesis of nanocrystalline anatase TiO<sub>2</sub> by one-pot two-phase separated hydrolysis-solvothermal processes and its high activity for photocatalytic degradation of rhodamine B. *J. Hazard Mater.* **176**, 139-145 (2010).
- [64] Ilyas, H., Masih, I., & van der Hoek, J. Disinfection methods for swimming pool water: byproduct formation and control. *Water* **10**, 797, 1-29 (2018).
- [65] Mills, A., & Le Hunte, S. An overview of semiconductor photocatalysis. *J. Photochem. Photobiol. A: Chem.* **108**, 1-35 (1997).
- [66] Park, H., Yang, D.-J., Yoo, J.-S., Mun, K.-S., Kim, W.-R., Kim, H.-G., & Choi, W.-Y. Surface passivation of highly ordered TiO<sub>2</sub> nanotube arrays and application to

dye-sensitized solar cells using the concept of isoelectric point. *J. Ceram. Soc. Jpn* **117**, 596-599 (2009).

[67] Zhu, Y., Shi, J., Zhang, Z., Zhang, C., & Zhang, X. Development of a gas sensor utilizing chemiluminescence on nanosized titanium dioxide. *Anal. Chem.* **74**, 120-124 (2002).

[68] Ni, M., Leung, M. K. H., Leung, D. Y. C., & Sumathy, K. A review and recent developments in photocatalytic water-splitting using TiO<sub>2</sub> for hydrogen production. *Renew. Sust. Energ Rev.* **11**, 401-425 (2007).

[69] Anpo, M., Yamashita, H., Ichihashi, Y., & Ehara, S. Photocatalytic reduction of CO<sub>2</sub> with H<sub>2</sub>O on various titanium oxide catalysts. *J. Electroanal. Chem.* **396**, 21-26 (1995).

[70] Joanne, G., & Zhang, Z. Applications of photocatalytic disinfection. *Int. J. Photoenergy* **2010**, 1-11 (2010).

[71] Gaya, U. I., & Abdullah, A. H. Heterogeneous photocatalytic degradation of organic contaminants over titanium dioxide: A review of fundamentals, progress and problems. *J. Photoch. and Photobio C* **9**, 1-12 (2008).

[72] Wei, X., Wang, K.-X., Guo, X.-X., & Chen, J.-S. Single-site photocatalysts with a porous structure. *Proc. Roy. Soc. A: Math., Phys. and Eng. Sci.* **468**, 2099-2112 (2012).

[73] Wu, Z., Cao, S., Zhang, C., & Piao, L. Effects of bulk and surface defects on the photocatalytic performance of size-controlled TiO<sub>2</sub> nanoparticles. *Nanotechnology* **28**, 275706 (2017).

[74] Santhosh, C., Malathi, A., Daneshvar, E., Kollu, P., & Bhatnagar, A. Photocatalytic degradation of toxic aquatic pollutants by novel magnetic 3D-TiO<sub>2</sub>@HPGA nanocomposite. *Sci. Rep.* **8**, 15531 (2018).



- [75] Elhalil, A., Elmoubarki, R., Sadiq, M., Abdennouri, M., Kadmi, Y., Favier, L., Qourzal, S., Barka, N. Enhanced photocatalytic degradation of caffeine as a model pharmaceutical pollutant by Ag-ZnO-Al<sub>2</sub>O<sub>3</sub> nanocomposite. *Desalin. water treat.* **94**, 254-262 (2017).
- [76] Alkaim, A., Kandiel, T. A., Hussein, F. H., Dillert, R., & Bahnemann, D. W. Enhancing the photocatalytic activity of TiO<sub>2</sub> by pH control: A case study for the degradation of EDTA. *Catal. Sci. Technol.* **3**, 3216-3222 (2013).
- [77] Costacurta, S., Maso, G. D., Gallo, R., Guglielmi, M., Brusatin, G., & Falcaro, P. Influence of temperature on the photocatalytic activity of sol-gel TiO<sub>2</sub> films. *ACS Appl. Mater. & Interfaces* **2**, 1294-1298 (2010).
- [78] Kumar, A. A review on the factors affecting the photocatalytic degradation of hazardous materials. *Material Sci & Eng Int J.* **1**, 1-10 (2017).
- [79] Wilke, K., & Breuer, H. D. The influence of transition metal doping on the physical and photocatalytic properties of titania. *J. Photoch. Photobio. A* **121**, 49-53 (1999).
- [80] Jitputti, J., Suzuki, Y., & Yoshikawa, S. Synthesis of TiO<sub>2</sub> nanowires and their photocatalytic activity for hydrogen evolution. *Catal. Commun.* **9**, 1265-1271 (2008).
- [81] Liao, D. L., & Liao, B. Q. Shape, size and photocatalytic activity control of TiO<sub>2</sub> nanoparticles with surfactants. *J. Photoche. Photobio. A* **187**, 363-369 (2007).
- [82] Zaleska-Medynska, A. Doped-TiO<sub>2</sub>: a review *Recent Pat. on Eng.* **2**, 157-164 (2008).
- [83] Singh, R., & Dutta, S. A review on H<sub>2</sub> production through photocatalytic reactions using TiO<sub>2</sub>/ TiO<sub>2</sub>-assisted catalysts. *Fuel* **220**, 607-620 (2018).
- [84] Humayun, M., Raziq, F., Khan, A., & Luo, W. Modification strategies of TiO<sub>2</sub> for potential applications in photocatalysis: A critical review. *Green Chem Let. Rev.* **11**, 86-102 (2018).

- [85] Jing, L., Zhou, W., Tian, G., & Fu, H. Surface tuning for oxide-based nanomaterials as efficient photocatalysts. *Chem Soc Rev*, **42**, 9509-9549 (2013).
- [86] Khan, M. R., Chuan, T. W., Yousuf, A., Chowdhury, M N. K., & Cheng, C. K. Schottky barrier and surface plasmonic resonance phenomena towards the photocatalytic reaction: Study of their mechanisms to enhance the photocatalytic activity. *Catal. Sci. Technol.* **5**, 2522-2531 (2015).
- [87] Chen, J., Qiu, F., Xu, W., Cao, S., & Zhu, H. Recent progress in enhancing photocatalytic efficiency of TiO<sub>2</sub>-based materials. *Appl. Catal. A: Gen.* **495**, 131-140 (2015).
- [88] Mogal, S. I., Gandhi, V. G., Mishra, M., Tripathi, S., Shripathi, T., Joshi, P. A., & Shah, D. O. Single-step synthesis of silver-doped titanium dioxide: influence of silver on structural, textural, and photocatalytic properties. *Ind. Eng. Chem. Res.* **53**, 5749-5758 (2014).
- [89] Ebrahimian, A. Silver doped TiO<sub>2</sub> nanoparticles: preparation, characterization and efficient degradation of 2,4-dichlorophenol under visible light. *J. Water Environ. Nanotechnol.* **1**, 135-144 (2016).
- [90] Lee, M. S., Hong, S.-S., & Mohseni, M. Synthesis of photocatalytic nanosized TiO<sub>2</sub>-Ag particles with sol-gel method using reduction agent. *J. Mol. Catal. A: Chem.* **242**, 135-140 (2005).
- [91] Wahyuni, E., & Aprilita, N. Photoreduction processes over TiO<sub>2</sub> photocatalyst. *InTech*. 1-17 (2018).
- [92] Sobana, N., Muruganadham, M., & Swaminathan, M. Nano-Ag particles doped TiO<sub>2</sub> for efficient photodegradation of direct azo dyes. *J. Mol. Catal. A: Chem.* **258**, 124-132 (2006).
- [93] Ge, W., Chen, Y., Wang, L., & Zhang, R. Photocatalytic Degradation of  $\beta$ -carotene with TiO<sub>2</sub> and Transition Metal Ions Doped TiO<sub>2</sub> under Visible Light Irradiation. *Univers. J. Chem.* **3**, 104-111 (2015).

- [94] Sobana, N., Muruganadham, M., & Swaminathan, M. Nano-Ag particles doped TiO<sub>2</sub> for efficient photodegradation of direct azo dyes. *J. Mol. Catal. A: Chem.* **258**, 124-132 (2006).
- [95] Seery, M. K., George, R., Floris, P., & Pillai, S. C. Silver doped titanium dioxide nanomaterials for enhanced visible light photocatalysis. *J. Photoch. and Photobio. A: Chem.* **189**, 258-263 (2007).
- [96] Chao, H. E., Yun, Y. U., Xingfang, H. U., & Larbot, A. Effect of silver doping on the phase transformation and grain growth of sol-gel titania powder. *J. Eur. Ceram. Soc.* **23**, 1457-1464 (2003).
- [97] Zhang, Y., Fu, F., Li, Y., Zhang, D., & Chen, Y. One-Step synthesis of Ag@TiO<sub>2</sub> nanoparticles for enhanced photocatalytic performance. *Nanomaterials* **8**, 1-15 (2018).
- [98] Santos, L. M., Machado, W. A., França, M. D., Borges, K. A., Paniago, R. M., Patrocínio, A. O. T., & Machado, A. E. H. Structural characterization of Ag-doped TiO<sub>2</sub> with enhanced photocatalytic activity. *RSC Advances* **5**, 103752-103759 (2015).
- [99] Zielinska-Jurek, A., Walicka, M., Tadaiewska, A., Łacka, I., Gazda, M., & Zaleska-Medynska, A. Preparation of Ag/Cu-doped titanium (IV) oxide nanoparticles in w/o microemulsion. *Physicochem. Probl. Miner. Process.* **45**, 113-126 (2010).
- [100] Nainani, R., Thakur, P., & Chaskar, M. Synthesis of silver doped TiO<sub>2</sub> nanoparticles for the improved photocatalytic degradation of methyl orange *J Mater. Sci. Eng. B* **2**, 52-58 (2012).
- [101] Dinh, C.-T., Yen, H., Kleitz, F., & Do, T.-O. Three-dimensional ordered assembly of thin-shell Au/TiO<sub>2</sub> hollow nanospheres for enhanced visible-light-driven photocatalysis. *Angew. Chem. Int. Ed.* **53**, 6618-6623 (2014).
- [102] Subramanian, V., Wolf, E. E., & Kamat, P. V. Catalysis with TiO<sub>2</sub>/gold nanocomposites. Effect of metal particle size on the fermi level equilibration. *J. Am. Chem. Soc.* **126**, 4943-4950 (2004).

- [103] Silva, C. G., Juárez, R., Marino, T., Molinari, R., & García, H. Influence of excitation wavelength (UV or visible light) on the photocatalytic activity of titania containing gold nanoparticles for the generation of hydrogen or oxygen from water. *J. Am. Chem. Soc.* **133**, 595-602 (2011).
- [104] Tanaka, A., Teramura, K., Hosokawa, S., Kominami, H., & Tanaka, T. Visible light-induced water splitting in an aqueous suspension of a plasmonic Au/TiO<sub>2</sub> photocatalyst with metal co-catalysts. *Chem. Sci.* **8**, 2574-2580 (2017).
- [105] Green, I. X., Tang, W., Neurock, M., & Yates, J. T. Spectroscopic observation of dual catalytic sites during oxidation of CO on a Au/TiO<sub>2</sub> catalyst. *Science* **333**, 736-739 (2011).
- [106] Tanaka, A., Ogino, A., Iwaki, M., Hashimoto, K., Ohnuma, A., Amano, F., Ohtani, B., Kominami, H. Gold–titanium(IV) oxide plasmonic photocatalysts prepared by a colloid-photodeposition method: correlation between physical properties and photocatalytic activities. *Langmuir*, **28**, 13105-13111 (2012).
- [107] Nasrabadi, H. T., Abbasi, E., Davaran, S., Kouhi, M., & Akbarzadeh, A. Bimetallic nanoparticles: Preparation, properties, and biomedical applications. *Artif. Cells Nanomed. Biotechnol.* **44**, 376-380 (2016).
- [108] Zielinska-Jurek, A. Progress, challenge, and perspective of bimetallic TiO<sub>2</sub>-based Photocatalysts. *J. Nanomater.* **2014**, 1-17 (2014).
- [109] Oros-Ruiz, S., Zanella, R., Collins, S. E., Hernández-Gordillo, A., & Gómez, R. Photocatalytic hydrogen production by Au–MxOy (MAg, Cu, Ni) catalysts supported on TiO<sub>2</sub>. *Catal. Commun.* **47**, 1-6 (2014).
- [110] Geonmonond, R. S., Silva, A., & Camargo, P. H. C. Controlled synthesis of noble metal nanomaterials: motivation, principles, and opportunities in nanocatalysis. *An Acad. Bras. Cienc.* **90**, 719-744 (2018).

- [111] Kim, D., Resasco, J., Yu, Y., Asiri, A. M., & Yang, P. Synergistic geometric and electronic effects for electrochemical reduction of carbon dioxide using gold–copper bimetallic nanoparticles. *Nature Commun.* **5**, 4948 (2014).
- [112] Lee, S. L., & Chang, C.-J. Recent developments about conductive polymer based composite photocatalysts. *Polymers* **11**, 206 (2019).
- [113] Floresyona, D., Goubard, F., Aubert, P.-H., Lampre, I., Mathurin, J., Dazzi, A., Ghosh, S., Beaunier, P., Brisset, F., Remita, S., Ramos, L. & Remita, H. Highly active poly(3-hexylthiophene) nanostructures for photocatalysis under solar light. *Appl. Catal B: Environment.* **209**, 23-32 (2017).
- [114] Zhang, G., Lan, Z.-A., & Wang, X. Conjugated polymers: catalysts for photocatalytic Hydrogen Evolution. *Angew. Chem. Int. Ed.* **55**, 15712-15727 (2016).
- [115] Su, Y. W., Lin, W. H., Hsu, Y. J., & Wei, K. H. Conjugated polymer/nanocrystal nanocomposites for renewable energy applications in photovoltaics and photocatalysis. *Small* **10**, 4427-4442 (2014).
- [116] Ghosh, S., Kouame, N. A., Remita, S., Ramos, L., Goubard, F., Aubert, P.-H., Dazzi, A., Deniset-Besseau A. & Remita, H. Visible-light active conducting polymer nanostructures with superior photocatalytic activity. *Sci. Rep.* **5**, 18002 (2015).
- [117] Katančić, Z. Synthesis of PEDOT/ZnO photocatalyst: validation of photocatalytic activity by degradation of Azo RR45 dye under solar and UV-A irradiation. *Chem. Biochem. Eng. Q.* **31**, 385-394 (2018).
- [118] Balinta, R., Cassidy, N. J., & Cartmell, S. H. Conductive polymers: towards a smart biomaterial for tissue engineering. *Acta Biomater.* **10**, 2341-2353 (2014).
- [119] Nguyen, D. N., & Yoon, H. Recent advances in nanostructured conducting polymers: from synthesis to practical applications. *Polymers* **8**, 118 (2016).

- [120] Majidi, S., Sehrig, F. Z., Farkhani, S. M., Goloujeh, M. S., & Akbarzadeh, A. Current methods for synthesis of magnetic nanoparticles. *Artif. Cells Nanomed. Biotechnol.* **44**, 722-734 (2016).
- [121] Yusoff, A. H. M., Salimi, M. N., & Jamlos, M. A review: Synthetic strategy control of magnetite nanoparticles production. *Adv. Nano Res.* **6**, 1-19 (2018).
- [122] Xu Y. & Zhu Y. Synthesis of magnetic nanoparticles for biomedical applications *Nano Adv.* **1**, 25–38 (2016).
- [123] Jamshidiyan, M., Shirani, A. S., & Alahyarizadeh, G. Solvothermal synthesis and characterization of magnetic Fe<sub>3</sub>O<sub>4</sub> nanoparticle by different sodium salt sources *Mater. Sci.* **35**, 50-57(2017).
- [124] Yao, H., Fan, M., Wang, Y., Luo, G., & Fei, W. Magnetic titanium dioxide based nanomaterials: synthesis, characteristics, and photocatalytic application in pollutant degradation. *J. Mater. Chem. A* **3**, 17511-17524 (2015).
- [125] Dagher, S., Soliman, A., Ziout, A., Tit, N., Hilal-Alnaqbi, A., Khashan, S., Alnaimat, F. & Qudeiri, J. A. Photocatalytic removal of methylene blue using titania- and silica-coated magnetic nanoparticles. *Mater. Res. Express* **5**, 1-13 (2018).
- [126] Greene, D., Serrano-Garcia, R., Govan, J., & Gun'ko, Y. K. Synthesis characterization and photocatalytic studies of cobalt ferrite-silica-titania nanocomposites. *Nanomater.* **4**, 331-343 (2014).
- [127] Mantione, D., Del Agua, I., Sanchez-Sanchez, A., & Mecerreyes, D. Poly(3,4-ethylenedioxythiophene) (PEDOT) derivatives: innovative conductive polymers for bioelectronics. *Polymers* **9**, 1-21 (2017).
- [128] Benhabiles, O., Galiano, F., Marino, T., Mahmoudi H., Lounici H., & Figoli A. Preparation and characterization of TiO<sub>2</sub>-PVDF/PMMA blend membranes using an alternative non-toxic solvent for UF/MF and photocatalytic application. *Molecules* **24**, 1-20 (2019).

- [129] Wu, F., Li, X., Liu, W., & Zhang S. Highly enhanced photocatalytic degradation of methylene blue over the indirect all-solid-state Z-scheme g-C<sub>3</sub>N<sub>4</sub>-RGO-TiO<sub>2</sub> nanoheterojunctions. *Appl. Surf. Sci.* **405**, 60–70 (2017).
- [130] Jiang, Y., Chen, W.-F., Koshy, P., & Sorrell, C. Enhanced photocatalytic performance of nanostructured TiO<sub>2</sub> thin films through combined effects of polymer conjugation and Mo-doping, *J. Mater. Sci.* **54**, 5266–5279 (2019).
- [131] Sangareswari, M., & Sundaram, M. M. Development of efficiency improved polymer-modified TiO<sub>2</sub> for the photocatalytic degradation of an organic dye from wastewater environment, *Appl. Water Sci.* **7**, 1781–1790 (2017).
- [132] Yang, C., Dong, W., Cui G., Zhao, Y., Shi, X., Xia, X., Tang, B. & Wang, W. Highly-efficient photocatalytic degradation of methylene blue by PoPD-modified TiO<sub>2</sub> nanocomposites due to photosensitization-synergetic effect of TiO<sub>2</sub> with PoPD, *Sci. Rep.* **7**, 1-12 (2017).
- [133] Dassanayake, R. S., Rajakaruna, E., & Abidi, N. Preparation of aeroxichitin-TiO<sub>2</sub> composite for efficient photocatalytic degradation of methylene blue, *J. Appl. Polym. Sci.* **135**, 1-10 (2017).
- [134] Li, J., Wen, X., Zhang, Q., & Ren, S. Adsorption and visible-light photodegradation of organic dyes with TiO<sub>2</sub>/conjugated microporous polymer composites, *RSC Adv.* **8**, 34560-34565 (2018).
- [135] Yu, W. J. , Cheng, Y., Zou T., Liu, Y., Wu, K., & Peng, N. Preparation of BiPO<sub>4</sub>-polyaniline hybrid and its enhanced photocatalytic performance. *NANO: Brief Rep. Rev.* **13**, 1-10 (2018).
- [136] Hiragond, C. B., Khanna, P. K., & More, P. V. Probing the real-time photocatalytic activity of CdS QDs sensitized conducting polymers: Featured PTh, PPy and PANI, *Vacuum*, **155**, 159–168 (2018).

[137] Mauro, A., Cantarella, M., Nicotra, G, Pellegrino, G., Gulino, A., Brundo, M. V., Privitera, V. & Impellizzeri, G. Novel synthesis of ZnO/PMMA nanocomposites for photocatalytic applications, *Sci. Rep.* **7**, 1-12 (2017).



## CURRICULUM VITAE

### PERSONAL INFORMATION

Surname, Name : Uzun, Ceren  
Nationality : Turkish (TC)  
Date and Place of Birth : 16 October 1986, Kdz. Ereğli (Zonguldak)  
Phone : +90 312 586 87 62  
E-mail : cerenuzun1986@gmail.com

### EDUCATION

<b>Degree</b>	<b>Institution</b>	<b>Year of Graduation</b>
PhD	METU Chemistry	2019
MS	METU Chemistry	2012
BS	METU Chemistry	2010
High School	Kdz. Ereğli Anatolian High School	2004

### WORK EXPERIENCE

<b>Year</b>	<b>Place</b>	<b>Enrollment</b>
2013-Present	Atılım University	Research Assistant
2012- June	METU Central Laboratory (Ankara)	Part-Time Specialist
2008-July	Ereğli Iron and Steel Works Co. (Zonguldak Ereğli)	Intern Student

### FOREIGN LANGUAGES

Advanced English, Basic German

## **PUBLICATIONS**

1. Khadim, R., Uzun, C., Cihaner, A., Kaya, M. (2019). Silver Nanoparticles Added Polymer Film Prepared by Electrochemical Route for Surface Enhanced Raman Scattering Applications, *J. Electrochem. Soc.*, 166 (4), B243-B248.

## **INTERNATIONAL AND NATIONAL CONFERENCE PAPERS**

1. Ceren Uzun, Murat Kaya, Mürvet Volkan, Preparation of Noble Metal Nanoparticle Loaded Titanium Dioxide as Photocatalyst, NANOTR14, İzmir, 2018

2. Canan Karabay, Ceren Uzun, Murat Kaya, Preparation of Noble Metal and Polymer Added Titanium Based Magnetic Photocatalytic Nanocomposite Material and Usage in Environmental Remediation, 10th Aegean Analytical Chemistry Days, Çanakkale, Turkey, September 29 th-October 02, 2016.

3. Ceren Uzun, Murat Kaya, Mürvet Volkan, Multiplexed and Sensitive Detection of Glucose via Fluorescence and Surface Enhanced Raman Spectroscopy, 10th Aegean Analytical Chemistry Days, Çanakkale, Turkey, September 29 th-October 02, 2016.

4. Ceren Uzun, Semra Kocabıyık, Mürvet Volkan, Application of SERS Nanotag Labeled Probes for DNA Studies, IUBMB and 37<sup>th</sup> FEBS, Sevilla, September 4 th-September 09, 2012.